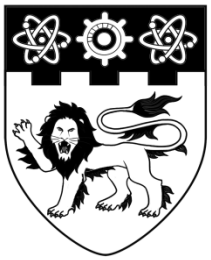

NANYANG
TECHNOLOGICAL
UNIVERSITY

Deployable Structure Associated with

Rigid Origami and Its Mechanics

LIU SI CONG

SCHOOL OF
MECHANICAL AND AEROSPACE ENGINEERING

2014

Deployable Structure Associated with
Rigid Origami and Its Mechanics

LIU SI CONG

2014

Deployable Structure Associated with Rigid Origami and Its Mechanics

LIU SI CONG

School of Mechanical and Aerospace Engineering

A Dissertation Submitted to the Nanyang Technological University in fulfilment of the requirement for the Degree of Doctor of Philosophy

2014

LIU SI CONG

Acknowledgement

First and foremost, I would like to express my sincere and warmst gratitude to my supervisor, Prof. Lu Guoxing, who supervised the experimental, numerical and theogetical work presented in the thesis, for his guidance, enouragement, and support during my PhD period. Without his patience and help, I would never make to this point. I would also like to thank my co-supervisor Prof. Chen Yan, who oversaw the kinematics studies, for the chance she gave me four years ago, which opened the door to the world of science.

Appreciation also goes to Dr. Leong Yew Wei from Institute of Materials Research and Engineering, who helped me select materials and fabricate the patterned sheet specimens, for his patience and understanding during our pleasant cooperation.

Deep appreciation and gratitude go to my senior research students and dear friends Song Chaoyang and Shen Changjian, who shared the research experiences and gave me valuable suggestions. I also want to thank the technical staffs at the Robotics Research Center and the workshops of MAE. Without your superb technical skills and assistance, my models will not be this fine. I want to give my thanks to my follow lab mates, Wang Zheng, Zhao Su, Sun Zhenglong, Wang Zhenan, Li Lei, Chi Wanchao, and other friends for sticking with me all along.

My special gratitude goes to Lu Zhengji for the kind advice and warm words during the hard times.

Last but not least, I would like to express my sincerest thanks to my parents and family, without their love, not only this work but any achievement in my life would be impossible.

Table of Contents

List of Notations

Z_i	Coordinate axis along the revolute axis of joint *i*.
X_i	Coordinate axis commonly normal to Z_{i-1} and Z_i , and $X_i = Z_{i-1} \times Z_i$.
Y_i	Coordinate axis commonly normal to X_i and Z_i , and $Y_i = Z_i \times X_i$.
θ_i	Revolute variable of joint *i*, which is the rotation angle from X_i to X_{i+1}, positive about Z_i .
d_i	Offset of joint *i*, which is the common normal distance from X_i to X_{i+1}, positive along axis Z_i .
$a_{i(i+1)}$	Length of link $i(i+1)$, which is the common normal distance from Z_i to Z_{i+1}, positive along axis X_{i+1}.
$\alpha_{i(i+1)}$	Twist of link $i(i+1)$, which is the rotation angle from Z_i to Z_{i+1}, positive about axis X_{i+1}.
$\mathbf{F}_i$	Coordinate frame: $X_i\ Y_i\ Z_i$.
$\mathbf{R}_z(\theta_i)$	Homogeneous matrices of rotation θ_i about axis Z_i .
$\mathbf{T}_z(d_i)$	Homogeneous matrices of translation d_i along axis Z_i .
$\mathbf{T}_x(a_{i(i+1)})$	Homogeneous matrices of translation $a_{i(i+1)}$ along axis X_{i+1}.

$\mathbf{R}_{\mathrm{x}}(\alpha_{i(i+1)})$	Homogeneous matrices of rotation $\alpha_{i(i+1)}$ about axis X_{i+1}.
$\mathbf{M}^{L}$	Matrix at the left side of an equation.
$\mathbf{M}^{R}$	Matrix at the right side of an equation.
$f_{i(i+2)}$	Relationship between the revolute variables of two opposite joints, θ_i and θ_{i+2}.
$f_{i(i+1)}$	Relationship between two adjacent revolute variables θ_i and θ_{i+1}.
i	Number of the revolute axis and cycles counter-clockwise, $i = 1, 2, 3, 4$.
j	Number of the spherical 4*R* linkages, *j* = I, II, III…*N*.
$\alpha^{j}_{i(i+1)}$	Twist $\alpha_{i(i+1)}$ of linkage *j*.
θ^{j}_{i}	Revolute variable θ_i of linkage *j*.
X^{j}_{i}	Axis X_i, of linkage *j*.
Z^{j}_{i}	Axis Z_i of linkage *j*.
f^{j}	Function f of linkage *j*.
f^{-j}	Inverse function of f^{j}.
L^{j}_{j+1}	Distance between the vertices of linkage *j* and *j*+1.
$\theta^{j}_{(i+1)i}$	Rotation angle from axis X^{j}_{i+1} to X^{j+1}_{i}, positively about Z^{j}_{i}.

$\mathbf{T}_{\mathbf{U}}^{(j+1)j}$	Transformation matrix from the coordinate frame X_3^{j+1} - Z_2^{j+1} to X_3^j - Z_2^j in the upper half of the prismatic structure.
$\mathbf{T}_{\mathbf{L}}^{j(j+1)}$	Transformation matrix from the coordinate frame X_4^j - Z_4^j to X_4^{j+1} - Z_4^{j+1} in the lower half of the prismatic structure.
j'	Projection of j on the plane that perpendicular to the ridgelines Z_2^j.
$\varepsilon_{m(m+1)}$	Dihedral angle represents the rotation from intersection plane m to $m + 1$, positive in the counterclockwise direction.
a , b	Lengths of the sides of a facet in the Miura-ori unit.
α	Twist angle of a facet in the Miura-ori unit.
θ	dihedral angle between a facet and the horizontal plane
D1, D2	In-plane direction 1 and 2 of the patterned sheet.
D3	Out-of-plane direction of the patterned sheet.
h	Height of the Miura-ori unit.
w	Width of the Miura-ori unit.
l	Length between two vertices in D1 direction.
l_1	Length of the side projected to D1 direction.
γ	Dihedral angle of the Miura-ori unit.
T	Thickness of the patterned sheet facets.
H	Height of the patterned sheet made of Elvaloy.

D_{D1}, D_{D2}	Average lengths of the patterned sheet in directions D1 and D2, respectively.
ρ	Density of material.
E	Young's modulus.
ν	Poisson's ratio.
V2V5	Distance between two vertices V2 and V5 in the Miura-ori unit.
F	Reaction force.
L_{D1}	The distance between the load in D1 direction and the fix end.
φ	Half of the dihedral angle γ, i.e. $\varphi = \frac{\gamma}{2}$, representing the rotation of a single facet around the ridge.
F_{D3}	Reaction force in direction D3.
dh	Changes in variable h.
M	Moment.
I	Second moment of cross-section of the ridge.
R	Radius of curvature after bending.
t	Thickness of the ridge lines.
nt	Half of the width of a hinge.
β	Angle between the direction of load and the direction perpendicular to the ridgeline.

List of Figures

List of Tables

Abstract

A special family of origami, rigid origami is when each paper facet surrounded with crease lines neither stretches nor bends during folding. In recent years, deployable structures and patterned sheets inspired by rigid origami have gained popularity among researchers in the fields of both mathematics and engineering. The focus of this thesis is on the kinematic modeling of the deployable structures, the mechanical behaviour and the mechanics of the Miura-ori patterned sheets.

The first part of this thesis is devoted to kinematic modeling of deployable surfaces. A kinematic model of mobile assemblies has been proposed based on the closed adjacent assembly of four spherical 4*R* linkages. To ensure the assemblies have a mobility of one, the kinematic compatibility conditions of the model have been obtained. The solutions to the compatibility conditions cover the existing one degree of freedom mobile assemblies, as well as twelve novel ones. In total, eighteen types of mobile assemblies have been devised. Based on the solutions, relationships between kinematic variables, hybrid assemblies, networks and rigid origami patterns for flat surfaces have been studied.

The second part of the thesis focuses on the kinematic modeling of the deployable prismatic structures. A kinematic model has been introduced based on closed opposite assembly of spherical 4*R* linkages. The kinematic compatibility conditions of these mobile assemblies have then been derived. Two groups of even-sided deployable prismatic structures have been obtained. For the 4-sided case, one structure incorporates a kite-shaped intersection, whereas the other incorporates a parallelogram. Unit variations have been discussed. Straight and curvy multi-layer prisms have been obtained by changing the dihedral angles between the intersecting planes. A general method to design even-sided multi-layer deployable prismatic structures has been proposed using the geometric conditions of the origami patterns. All the

deployable structures constructed using this method can be deployed and folded along the central axis with a single degree of freedom; this makes them usable for a wide range of engineering applications.

An investigation of deformations in patterned sheets forms the final part of this thesis. A Miura-ori patterned sheet was made from copolymer Elvaloy by compression molding and its deformation behavior was investigated experimentally and using finite element analysis. Mechanical tests have been performed on the material and patterned sheet. FE simulations using ABAQUS/Explicit have been carried out to analyse deformations on the patterned sheet. Based on the simulation results, the deformation patterns on the patterned sheet under different loading conditions were examined, as well as their energy absorption capacities. Theoretical analyses based on the deformation patterns predicted the mechanical behaviour of the patterned sheet. Therefore, the geometry and material of the patterned sheet can be designed to meet the requirements of a certain application.

Chapter 1

Introduction

1.1 Rigid origami

Origami is to fold paper into a sculpture; it is a traditional Japanese art with hundreds of years of history (Bern and Hayes 1996). The folding mechanism of origami has been attracting the attention of mathematicians and engineers for decades and is continuing to nourish new research.

The study of origami encapsulates several subjects of mathematical interest. For instance, the problems of flat-foldability and mobility have been studied by considerable mathematical studies. A number of technological advances have come from insights obtained through paper folding, such as the deployment of car airbags and stent implants from a folded position. Origami can also be used to construct various geometrical designs not possible with compass and straightedge constructions. For instance paper folding may be used for angle trisection and doubling the cube.

Recently, in focusing on the folding properties of origami inspired structures, researchers in mechanical and material engineering fields have carried out research on mechanical metamaterials (Schenk and Guest 2013; Wei, Guo et al. 2013) and self-folding structures (Antkowiak, Audoly et al. 2011; Chalapat, Chekurov et al. 2013; Ionov 2013).

A special family of origami, *rigid origami* refers to origami when each paper facet surrounded with crease lines is not stretching or bending during folding (Watanabe and Kawaguchi 2009). Rigid origami has attracted interest from researchers in both mathematics and engineering. Watanabe proposed a method to judge the rigidity of known origami patterns. Dai and Jones focused on the

kinematics and mobility of the rigid carton folds in packing manipulation, using screw theory to explain the folding of the mechanism from one distinctive configuration to another (Dai and Jones 1999, 2002). Due to the simple foldability, rigid origami patterns can be actuated with ease. The shape memory alloy actuators are often integrated into the structure in order to achieve programmable robots with precise actuation control (Onal, Wood et al. 2011; Byoungkwon and Rus 2012; Onal, Wood et al. 2013) and the planar fabrication of 3-D mechanisms (Onal, Wood et al. 2011). The stiffness of the rigid panels in the rigid origami pattern provides strong and robust resistance to external impacts, which fulfills the needs of civil engineering applications. Chudoba (Chudoba, van der Woerd et al. 2013) used the folding technique to produce spatial structures from continuously thin-walled rigid composite plates. It also reduced the complexity of the design and simulated the manufacture process of the deployable structures (Ario, Nakazawa et al. 2013). Rigid origami patterns possess the ability to be fully deployed into a flat state, which benefits the storage and transportation of the structures. Correspondingly, substituting the crease lines with hinges, 3-D structures can be deployed from a patterned flat sheet. Compared with traditional component manufacturing, patterned fabrications of the flat sheets are sped up considerably by current 3-D printing and monolithic fabrication technology (Sreetharan, Whitney et al. 2012).

1.2 Spherical 4*R* linkage

From a kinematic point of view, the movement of structures with rigid origami patterns is a type of mechanism motion (Tachi 2009a). When the facets and crease are replaced by rigid panels and hinges, the rigid origami patterns evolve into assemblies of linkages. In particular, when four fold creases intersect at a vertex, the creases and facets around this vertex can be represented by a *spherical 4R linkage* (Nojima 2002; Trautz and Künstler 2009). Thus, a pattern with multiple such vertices can be considered as an assembly of spherical linkages.

A spherical 4*R* linkage has four revolute joints with axes intersected at a single point; its links move on concentric spheres. Different aspects of the spherical 4*R* linkage have been studied in previous pieces of research. McCarthy (McCarthy and Soh 2011) and Cervantes (Cervantes-Sánchez and Medellín-Castillo 2002) introduced their classification schemes. Chiang (Chiang 1984) and (Medellín-Castillo and Cervantes-Sánchez 2005) focused on the mobility of the links. Ruth (Ruth and McCarthy 1999) and McCarthy (McCarthy and Bodduluri 2000) described computational methods for orientation and position synthesis. Due to its one degree of freedom (one-DOF) mobility, which means only one independent parameter (angle of rotation) is needed to define the configuration of the mechanical system, the spherical 4*R* linkage has been used as basic element to construct other mechanisms, such as Hooke's linkage and double Hooke's linkage (Mills 2007).

In recent years, researchers started to use the spherical 4*R* linkages to represent the mechanism of the rigid origami patterns. Wei and Dai analysed an origami carton by representing it with a single planar four-bar loop and two spherical 4*R* linkage loops (Wei and Dai 2009, 2014). Wu and You (Wu and You 2011) proposed a new crease pattern that allows a tall box-shaped bag with a rectangular base to be rigidly folded flat. Wang and Chen used the assembly of spherical 4*R* linkages to study a special rigid origami pattern (Chen 2003; Wang and Chen 2010). Using the tessellation method for mobile assemblies of spatial linkages, a mobile assembly of spherical 4*R* linkages was proposed to study Kokotsakis-type rigid origami patterns.

1.3 Deployable surfaces

Deployable structures are novel and unique engineering structures whose geometry can be changed greatly to satisfy different practical requirements. Examples include solar arrays in the aerospace industry, retractable roofs for large stadiums, expandable stents to treat blockages in blood vessels, etc. Similar to the rigid origami patterns, the flexibilities and deformations of the

deployable surfaces were studied in discrete differential geometry (Kokotsakis 1933; Karpenkov 2010). By analysing the spherical images of vertices, a new family of flexible Kokotsakis meshes has been discovered by Stachel (Stachel 2010). The author summarized five types of Kokotsakis meshes, and reestablished them with a 3 by 3 panel configuration. This nine-panel configuration is essential to the structure because in (Schief, Bobenko et al. 2008), it was proved that a polyhedral surface is continuously deformable only when its 3 by 3 sub-surfaces are continuously deformable. Here, only the polyhedral surfaces that have four facets around each vertex are of interest.

Through various approaches mentioned, six types of one-DOF mobile assemblies have been discovered: identical linkage type (line-symmetric type) (Kokotsakis 1933), planar-symmetric type (Stachel 2010), translational type (Stachel 2010), isogonal type (discrete Voss surface) (Stachel 2010), orthogonal type (Sauer and Graf 1931; Stachel 2010) and Miura-ori type (Miura 1989b; Stachel 2009). However, there is no such approach which covers all the types with explicit, necessary and sufficient geometric relationships.

1.4 Deployable prismatic structures

Deployable/foldable prismatic structures with origami patterns have attracted much interest from mathematicians, engineers, artists, etc. Cylindrical deployable structures with rigid quadrilateral panels were developed and analysed by Tachi (Tachi 2009b; Yasuda, Yein et al. 2013). Nojima (Nojima 2002, 2007) presented many types of patterns to axially fold cylinders and cones. The geometric and mechanical properties of triangulated patterns in cylinders (Guest and Pellegrino 1994) and conical structures (Ishida, Nojima et al. 2014) were studied. The thin-walled structure with origami patterns has been used in energy-absorbing devices (Ma, Le et al. 2010; Zhao, Hu et al. 2011; Song, Chen et al. 2012, 2013; Ma and You 2013a, 2013b). A diamond pattern has been created for beverage cans in Japan (Miura 2002) to reduce weight and to more easily crush the cans. Additionally, a cylinder that could be folded

radially has been used as a medical stent (Kuribayashi, Tsuchiya et al. 2006). Also, shape-memory alloy actuators have been integrated into structures to achieve programmable worm robots with desired motion control (Onal, Wood et al. 2013). Most of these structures incorporate non-rigid origami patterns to realize deployment and the folding process, i.e., large deformations occur on both the folding lines and panels in these continuous shell structures.

1.5 Patterned sheet

As one of the essential rigid origami patterns, the Miura-ori consists of identical parallelogram facets surrounding the vertices of degree 4 (Miura 1989a). When the facets and crease lines are replaced with rigid panels and revolute hinges, respectively, the Miura-ori can be represented by a mechanism (Trautz and Künstler 2009; Liu, Chen et al. 2013). In that case, the movement of the Miura-ori can uniquely be described kinematically (Schenk and Guest 2011b). The properties of rigid foldable, flat folding and developable (Tachi 2009a) grant the Miura-ori origami inspired structures with a wide range of potential applications. Here, the Miura-ori patterned sheet is studied as the basic folded core in sandwich structures.

Sandwich structures are widely used in the aircraft and automotive industries due to their high stiffness-to-weight ratio and configurable energy absorption performance (Lu and Yu 2003; Shen, Lu et al. 2013). However, the drawbacks of the conventional honeycomb core, namely, the accumulation of humidity, the complicated manufacture process and the vulnerability against impact loads, limit the applications of sandwich structures. In comparison, the Miura-ori patterned sheets have a number of advantages such as their open ventilation channels, a continuous manufacture process, superior energy absorption and better impact properties, etc. (Heimbs, Middendorf et al. 2007).

In recent years, studies on the Miura-ori patterned folded cores have gained popularity. Fischer et al. (Fischer, Drechsler et al. 2009a; Fischer, Heimbs et al.

2009b) produced and tested various folded cores with different unit cell geometries and different base materials. The base materials were tested in tension and compression to obtain their material data, which was subsequently used in FE simulation. Heimbs et al. (Heimbs, Middendorf et al. 2007; Heimbs, Cichosz et al. 2009; Heimbs, Cichosz et al. 2010) studied their mechanical behavior under compression, shearing and impact loads on the folded cores made from prepreg sheets of carbon fiber/aramid fiber. In addition, a dual-core configuration with two folded cores was investigated. Lebée and Sab (Lebée and Sab 2010b) derived upper and lower bounds for the effective transverse shear moduli of a chevron folded core and compared it to finite element computations. Schenk and Guest (Schenk, Allwood et al. 2011a; Schenk and Guest 2013) proposed a novel manufacturing process, which used cold gas-pressure to fold sheets into Miura-ori. Two folded metamaterials were also introduced based on a stacking of individual Miura-ori layers. Wei et al. (Wei, Guo et al. 2013) analysed the Poisson's ratio of the Miura-ori metamaterial and the effective bending stiffness of the unit cell, and solved the inverse design problem for the optimal geometric and mechanical response. Zhou et al. (Zhou, Wang et al. 2014) presented a parametric study on the Miura-based folded core models using the finite element method. The folded core models are compared to a honeycomb core model with the same density and height.

1.6 Aim and scope

The aim of this thesis is two-fold. Firstly, it intends to explore the kinematic deformation and rigid mobility of deployable structures, including the surfaces and prismatic structures. The deployable structures of interest specifically have one degree of freedom, consisting of rigid planar quadrilateral facets, and degree-4 vertices. Thus, the mobile assemblies of the spherical 4*R* linkages are employed to model the deployable structures. The spherical 4*R* linkages are assembled in two different ways to represent the surfaces and the prismatic structures, respectively. Apart from the existing types, a variety of new deployable surfaces and prismatic structures are derived, with explicit

geometric relationships given, as a way to explore new applications within engineering.

Secondly, the focus is on the deformations of Miura-ori patterned sheet under quasi-static load conditions. As a display of the simple manufacturing process, the Miura-ori patterned sheets made of copolymer Elvaloy are manufactured by compression moulding. To investigate the mechanical properties, mechanical tests were carried out on the material and patterned sheet. FE model in ABAQUS/Explicit are validated by experimental results and subsequently used to analyse the deformation patterns and the energy absorption capacities in different load conditions. To further understand the mechanics of the patterned sheet, theoretical analyses are performed. Comprehensive investigation on the patterned sheet achieves the aim of predicting the mechanical behaviour, and proving that the geometry and material of the patterned sheet can be designed to meet the requirements of a certain application.

1.7 Contributions

In this thesis, the contributions include the follows.

A kinematic model has been introduced, representing all the deployable surfaces with one degree of freedom and consisting of rigid planar quadrilaterals and degree-4 vertices. New types of deployable surfaces have been derived; networks, rigid origmai patterns, hybrid types have been discussed

To model deployable prismatic structures, a kinematic model has also been introduced. Two groups of 2n-sided deployable prismatic structures have been derived; the multilayer, straight and curvy prismatic structures have been constructed.

To investigate the Miura-ori patterned sheet, the specimens have been made from copolymer Elvaloy by compression moulding. The deformation behaviour has been investigated experimentally as well as with finite element analysis. A

theoretical analysis has been carried out associated with the deformation patterns obtained in the FE simulations.

1.8 Outline of thesis

The layout of the thesis is as follows. First, an extended review of the researches is given in Chapter 2, covering all the relevant topics regarding deployable surfaces, deployable prismatic structures, and patterned sheets.

Then the following two chapters will focus on the kinematic modeling of the deployable structures. In Chapter 3, the kinematics model of the deployable surfaces based on the adjacent assembly of four spherical 4R linkages will be introduced. The existing and new types of one-DOF deployable surfaces will be derived from the model. The discussions will be carried out on the deployable surfaces, regarding the relationships of kinematic variables, the hybrid assemblies, networks and rigid origami patterns for flat surfaces.

In Chapter 4, focusing on constructing deployable prismatic structures with a rigid origami pattern, the opposite assembly of the spherical 4*R* linkages will be introduced to model the deployable prismatic structures. The kinematic compatibility conditions for the model will be derived. The rigid origami patterns for two groups of even-sided prismatic structures will be obtained. The straight and curvy multi-layer structures will be proposed. In addition, a general design method for multi-layer deployable prismatic structures will be presented.

Next, Chapter 5 is devoted to the deformations of the Miura-ori patterned sheet. The manufacturing process of the Miura-ori patterned sheet will be introduced. The setup and results of the quasi-static experiments will be presented and then compared with the FE simulation results in ABAQUS/Explicit. The theoretical analysis will be performed to further investigate the mechanics of the patterned sheets.

Finally, the main contributions of the thesis and the suggestions for future work are presented in Chapter 6, which concludes the thesis.

Chapter 2

Literature Review

This thesis is to explore the fundamental kinematics, mechanics and the application perspectives of rigid origami inspired structures. This chapter will review relevant topics covering design to manufacturing, using both experimental and numerical analysis, presenting and citing all relevant studies.

2.1 Rigid origami

Origami is the traditional art of paper folding into sculpture. It is a continuous, one-to-one mapping of a crease pattern to create a three-dimensional object. The mapping must be smooth (differentiable) everywhere except along creases. A *crease pattern* is defined here as a finite planar straight-line graph drawn on a convex planar region. A *crease* is an edge of the planar graph (Bern and Hayes 1996).

Rigid origami is a branch of origami which is defined as origami whose surfaces surrounded with crease lines are not stretching and bending (Watanabe and Kawaguchi 2009). It can be used to realize a mechanism, and its facets and crease lines can be replaced by rigid panels and hinges (Trautz and Künstler 2009). To judge the rigidity of origami, two mathematical models have been proposed: the matrix model (Belcastro and Hull 2002) and the geometric model (Gaussian Curvature) (Huffman 1976; Miura 1989a).

2.2 Spherical 4*R* linkage and its assembly

A four-bar linkage is the simplest movable closed chain linkage. It consists of four bodies, called bars or links, connected in a loop by four joints. Generally, the joints are configured so that the links move in parallel planes; the assembly

is called a planar four-bar linkage. If all four joints are revolute joints, the planar four-bar linkage is called a *planar 4R linkage*.

If the linkage has four revolute joints with axes angled to intersect at a single point, then the links move on concentric spheres and the assembly is called a *spherical 4R linkage*, i.e. the Hooke's linkage and the double Hooke's linkage (Mills 2007). Spherical 4*R* linkage can also be viewed as spherical quadrilaterals with vertices that are hinged joints, denoted R for revolute. The axes of these hinges must intersect in a single point in order for the spherical 4R linkage to provide a one-degree-of-freedom rotational, or spherical, movement (Ruth and McCarthy 1999). In fact, planar 4*R* linkage is a special case of spherical 4*R* linkage in which the radius of the sphere extends to infinity. The spherical 4*R* linkage, being analogous to the 4*R* linkage in plane mechanisms, is the basic form of all spherical mechanisms (Chiang 1984).

Unlike the planar 4*R* and spherical 4*R* linkages which have couplers that move along a plane or on a sphere, respectively, a *spatial 4R linkage* is the 4*R* closed chain that guides a coupler through a spatial trajectory (Perez and McCarthy 2002). The Bennett's linkage is a spatial 4*R* linkage with hinged joints that have their axes angled in a particular way that makes the system movable (Bennett 1903; Song 2013).

Compared with plane and spatial linkages, spherical linkages have the following advantages. First of all, a spherical mechanism takes up the least space. It is possible by coupling two spherical 4*R* linkages to obtain a variety of transmission characteristics, and also by combining a spherical 4*R* linkage with a pair of bevel gears it is easy to obtain a rotary dwell mechanism. A spherical mechanism is a rather direct solution to the problems in transmitting a rotary motion from one shaft to another shaft whose axis is intersecting at an angle with the axis of the fist shaft. It is even possible to obtain from a single spherical 4*R* linkage, the so-called proportional mechanism, i.e. a mechanism

with approximately constant angular velocity ratio over a certain range of the input angle (Chiang 1988).

Most recently, Wang and Chen used the assembly of spherical 4R linkages to study rigid origami patterns (Chen 2003; Wang and Chen 2010). Wang and Chen pointed out that the fold creases can be considered as a revolute joint. If several creases intersect at a single vertex, the rigid origami pattern is a spherical linkage (Nojima 2002). When 4 fold creases intersect at a vertex, the origami pattern becomes a spherical 4*R* linkage (Guest and Pellegrino 1994). It was found that a spherical 4*R* linkage has only one degree of freedom. The kinematic representation of a spherical 4*R* linkage are established as shown in Fig. 2.1.

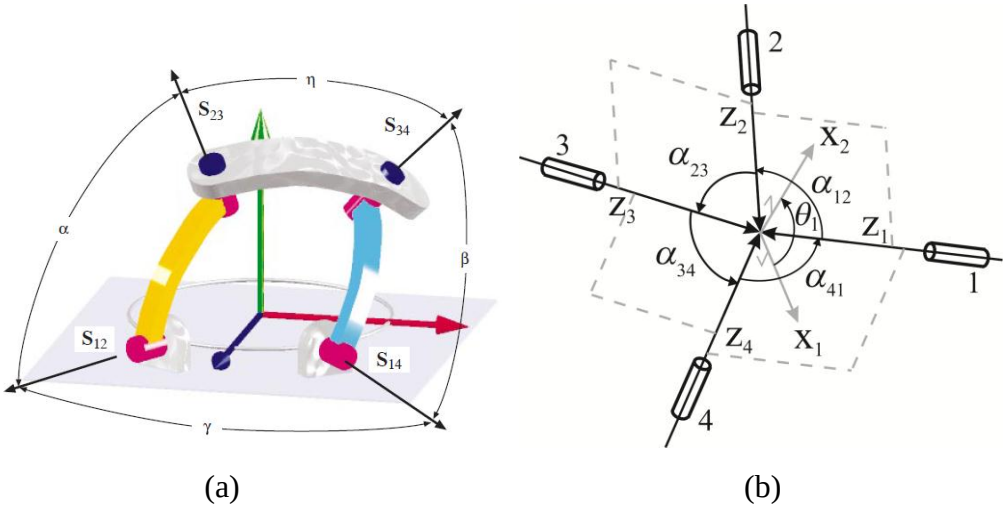

(a) (b)

Fig. 2.1 (a) A spherical 4*R* linkage (Ruth and McCarthy 1999); (b) a single spherical 4*R* linkage is used to represent a rigid origami pattern.

Denavit and Hartenberg (Denavit and Hartenberg 1955) pointed out that, for a simple close-loop in a linkage, the product of all the transform matrices equals the unit matrix. So the loop closure equation becomes

$$\mathbf{T}_{21}\mathbf{T}_{32}\mathbf{T}_{43}\mathbf{T}_{14} = \mathbf{I}, \tag{2.1}$$

in which $\mathbf{T}_{ij}$ is the transformation matrix from coordinate frame *j* to *i*. As shown in Fig. 2.2, the spherical 4*R* linkages are assembled by connecting axes of every adjacent linkages. The shared axis is considered as a common joint, and all the common joints form a closed loop.

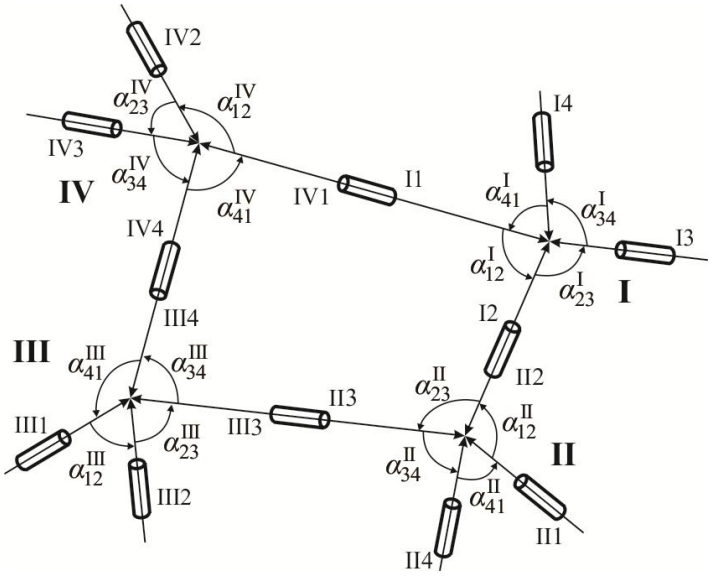

Fig. 2.2 Assembly of four spherical 4*R* linkages.

2.3 Deployable surface

2.3.1 Design method

Numerious studies have analysed the mechanism of deployable surfaces by using mathmatical and geometric methods. The deployable surfaces of interest here have one-degree of freedom and are constituted by rigid quadrilateral surfaces and degree-4 vertices.

(1) Discrete differential geometry

Studies (Bobenko and Pinkall 1996; Bobenko and Suris 2008; Schief, Bobenko et al. 2008) in the field of *discrete differential geometry* revealed that when

each quadrilateral is rigid and only the dihedral angles can vary, a complex of eight planar quadrilaterals is always deformable while a 3×3 complex is generically rigid. A discrete conjugate net, which is the discrete surfaces composed of planar quadrilaterals, in general position is continuously flexible if and only if all its 3×3 complexes, i.e., all included Kokotsakis meshes, are continuously flexible. The *discrete Voss surfaces* were defined as a non-degenerate discrete conjugate net whose opposite angles at each vertex are equal. The discrete Voss surfaces are one-DOF flexibile.

(2) Kokotsakis mesh

A *Kokotsakis mesh* is a polyhedral structure consisting of an n-sided central polygon surrounded by a belt of polygons (Schief, Bobenko et al. 2008; Karpenkov 2010). Stachel focused on the question of under what conditions is a Kokotsakis mesh infinitesimally or continuously flexible (Stachel 2010).

Stachel proposed that a Kokotsakis mesh is of k-th order infinitesimally flexible or continuously flexible if and only if its spherical image is of k-th order infinitesimally or continuously flexible, respectively. When the central polygon is a quadrilateral ($n=4$), the Kokotsakis mesh is constituted of 9 rigid faces and 12 variable dihedral angles (Izmestiev 2009). In (Stachel 2010), the spherical image of a Kokotsaki mesh ($n=4$) is used to study the flexibility of the mesh.

(3) Flat-foldable quadrilateral-mesh origami

A quadrilateral-mesh surface, consisting of degree-4 vertices, is overconstrained and does not enable rigid foldablility. To obtain a rigid deployment mechanism with one degree of freedom, the necessary and sufficient condition for the existence of finite rigid motion of general flat-foldable *quadrilateral-mesh origami* was derived in (Tachi 2009a). The crease pattern of a single vertex with developablility and flat-foldability was proved to be completely defined by two independent dehedral angles. A variety of

quadrilateral-mesh origami shapes were derived, which are one-DOF finite rigid-foldable, developable and flat-foldable. The developability is represented by the Gauss area around each vertex to be 0, which equals 2π minus the sum of the sector angles. The flat-foldability is satisfied if the alternating sum of the sector angles around each vertex is 0 and the overlapping order can be determined (Bern and Hayes 1996).

2.3.2 Existing one-DOF rigid origami patterns

There are six types of one-DOF flexible quadrilateral surfaces which can be considered as rigid origami patterns, consisting of planar rigid quadrilaterals, introduced and examined by previously mentioned studies. The relationship between the twist angles in each type is given according to the definition in Fig. 2.2.

1) **The identical linkage type** (Kokotsakis 1933): this type was originally introduced by Kokotsakis. In (Wang and Chen 2010), a spherical 4*R* linkage was employed to represent the assembly of four quadrilaterals with edges intersecting at the vertex. Thus, the whole structure, constituted of nine quadrilaterals, can be considered as the assembly of four identical spherical 4*R* linkages following a rotaitonal configuration.

$$\alpha_{i(i+1)}^{\mathrm{I}} = \alpha_{i(i+1)}^{\mathrm{II}} = \alpha_{i(i+1)}^{\mathrm{III}} = \alpha_{i(i+1)}^{\mathrm{IV}}. \tag{2.2}$$

2) **Planar-symmetric type** (Kokotsakis 1933): The reflection in the plane of symmetry maps each horizontal fold onto itself while the two vertical folds are exchanged.

$$\begin{aligned}
&\alpha_{12}^{\mathrm{I}} = \alpha_{23}^{\mathrm{II}}, \quad \alpha_{12}^{\mathrm{III}} = \alpha_{23}^{\mathrm{IV}}, \\
&\alpha_{23}^{\mathrm{I}} = \alpha_{12}^{\mathrm{II}}, \quad \alpha_{23}^{\mathrm{III}} = \alpha_{12}^{\mathrm{IV}}, \\
&\alpha_{34}^{\mathrm{I}} = \alpha_{41}^{\mathrm{II}}, \quad \alpha_{34}^{\mathrm{III}} = \alpha_{41}^{\mathrm{IV}}, \\
&\alpha_{41}^{\mathrm{I}} = \alpha_{34}^{\mathrm{II}}, \quad \alpha_{41}^{\mathrm{III}} = \alpha_{34}^{\mathrm{IV}}.
\end{aligned} \tag{2.3}$$

3) **Translational type** (Stachel 2010): There is a translation mapping the three faces on the right-hand side of the vertical fold onto the triple on the left-hand side of the vertical fold.

$$\begin{aligned}
&\alpha_{12}^{\mathrm{I}} + \alpha_{23}^{\mathrm{II}} = \pi, \quad \alpha_{12}^{\mathrm{III}} = \alpha_{23}^{\mathrm{IV}}, \\
&\alpha_{23}^{\mathrm{I}} + \alpha_{12}^{\mathrm{II}} = \pi, \quad \alpha_{23}^{\mathrm{III}} = \alpha_{12}^{\mathrm{IV}}, \\
&\alpha_{34}^{\mathrm{I}} = \alpha_{41}^{\mathrm{II}}, \quad \alpha_{34}^{\mathrm{III}} + \alpha_{41}^{\mathrm{IV}} = \pi, \\
&\alpha_{41}^{\mathrm{I}} = \alpha_{34}^{\mathrm{II}}, \quad \alpha_{41}^{\mathrm{III}} + \alpha_{34}^{\mathrm{IV}} = \pi.
\end{aligned} \tag{2.4}$$

4) **Isogonal type (**Kokotsakis 1933; Bobenko and Suris 2008): At each vertex opposite angles are congruent, i.e.

$$\alpha_{12}^{j} = \alpha_{34}^{j}, \quad \alpha_{23}^{j} = \alpha_{41}^{j}. \tag{2.5}$$

5) **Orthogonal type** (Sauer and Graf 1931): Here the horizontal folds are located in parallel planes, the vertical folds in vertical planes.

$$\alpha_{12}^{\mathrm{I}}+\alpha_{23}^{\mathrm{II}}=\pi,\quad \alpha_{23}^{\mathrm{I}}+\alpha_{12}^{\mathrm{II}}=\pi,$$

$$\alpha_{34}^{\mathrm{III}}+\alpha_{41}^{\mathrm{IV}}=\pi,\quad \alpha_{41}^{\mathrm{III}}+\alpha_{34}^{\mathrm{IV}}=\pi,$$

$$\cos\alpha_{12}^{j}\cos\alpha_{34}^{j}=\cos\alpha_{23}^{j}\cos\alpha_{41}^{j}, \tag{2.6}$$

$$\alpha_{12}^{\mathrm{I}}=\alpha_{41}^{\mathrm{IV}},\quad \alpha_{41}^{\mathrm{I}}=\alpha_{12}^{\mathrm{IV}},$$

$$\alpha_{23}^{\mathrm{II}}=\alpha_{34}^{\mathrm{III}},\quad \alpha_{34}^{\mathrm{II}}=\alpha_{23}^{\mathrm{III}}.$$

6) **Miura-ori type** (Miura 1989b; Stachel 2009): Miura-ori is a Japanese folding technique named after Prof. Koryo Miura in University of Tokyo. It is used for solar panels because it can be unfolded into its rectangular shape by pulling on one corner only.

$$\begin{aligned}&\alpha_{41}^{\mathrm{I}}=\alpha_{12}^{\mathrm{I}}=\alpha_{41}^{\mathrm{II}}=\alpha_{12}^{\mathrm{II}}=\alpha_{23}^{\mathrm{III}}=\alpha_{34}^{\mathrm{III}}=\alpha_{23}^{\mathrm{IV}}=\alpha_{34}^{\mathrm{IV}},\\&\alpha_{23}^{\mathrm{I}}=\alpha_{34}^{\mathrm{I}}=\alpha_{23}^{\mathrm{II}}=\alpha_{34}^{\mathrm{II}}=\alpha_{41}^{\mathrm{III}}=\alpha_{12}^{\mathrm{III}}=\alpha_{41}^{\mathrm{IV}}=\alpha_{12}^{\mathrm{IV}}.\end{aligned} \tag{2.7}$$

2.4 Deployable prismatic structures

Cylindrical, deployable and collapsible structures composed of two-dimensional elements are useful in various designs. Such a structure can form a watertight surface that encloses a certain desired volume by the addition of two surfaces at the ends, and the surfaces can be compactly folded down into a two-dimensional state. Several flat-foldable cylindrical deployable structures have been proposed thus far, e.g., by Hoberman (Hoberman 1993), Guest and Pellegrino (Guest and Pellegrino 1994), Sogame and Furuya (Sogame and Furuya 2000) and Nojima (Nojima 2007). However, all of the existing deployable tubes are bi-stable structures whose transformation mechanisms rely on the in-plane elastic deformation. Since the mechanism of such a structure relies on the material flexibility, the applications were limited, e.g., an energy

absorption device that can be used only once, as proposed by Wu (Wu, Hagiwara et al. 2007), a small-scale medical device by Kuribayashi (Kuribayashi, Tsuchiya et al. 2006), a deployable membrane structure for use in space proposed by Sogame and Furuya (Sogame and Furuya 2000).

Tachi has presented a novel cylindrical, deployable structure in which every element of the surface is geometrically free of distortion (Tachi 2009b). In addition, the cylindrical, deployable structure has the following characteristics:

1) Flat-foldable: The shape flattens into a compact 2D configuration.

2) Rigid-foldable: Each element does not deform throughout the transformation.

3) One-DOF: The mechanism has exactly one degree of freedom.

4) Thick: Facets can be substituted with thick or multilayered panels without introducing the distortion of elements.

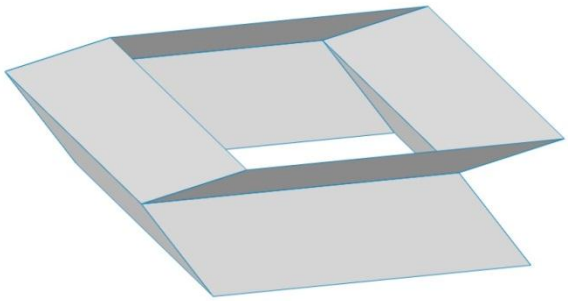

Fig. 2.3 A basic unit.

The basic unit structure is constructed by joining two pieces: a single vertex origami with four congruent parallelograms and its mirror image with respect to the plane of reflection, as shown in Fig. 2.3.

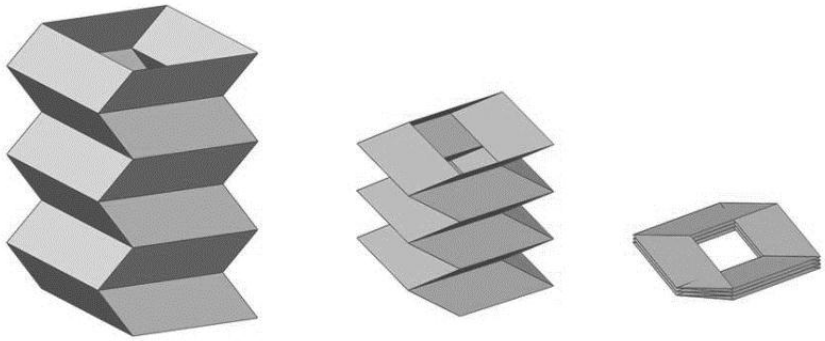

Fig. 2.4 A rigid-foldable cylindrical structure.

The vertex produces a one-DOF folding mechanism in which the edges on the plane of reflection always lie on the plane. This enables the formation of a valid joint structure from two pieces. The rhombus at each open end is maintained as co-planar throughout the folding process. This enables the repetition of the units in the axial direction, to construct a cylinder of an arbitrary length (Fig. 2.4).

2.5 Applications of the deployable structures

Structures inspired by rigid origami patterns have significant potential in various state of the art applications.

2.5.1 Thin-walled structures with origami patterns

The thin-walled structures with origami patterns are introduced to improve energy absorption. Thin-walled tubes are used as energy absorption devices in automobiles. In (Song, Chen et al. 2012), to minimize the initial peak and the subsequent fluctuations in axial crushing, tubes of square, hexagonal, and octagonal cross-sections with origami patterns were investigated numerically and experimentally. The crushing mode follows the origami pattern of the tube, which leads to a lower initial peak force and more uniform crushing load. The improved behavior under crushing of the origami patterned tubes inspired the windowed tubes introduced in (Song, Chen et al. 2013), which showed

enhanced performance while being crushed and energy absorption over the conventional tube.

The thin-walled structure with origami patterns were further studied in (Ma and You 2013a). The origami beams were subjected to the quasi-static lateral load in FE simulations. Two new collapse modes were triggered, which also resulted in higher energy absorption and lower peak force than those of conventional structures. The origami crash box pre-fold in the thin-walled tubes was introduced in (Ma and You 2013b) to create a type of geometric imperfection to lower the initial buckling force and trigger a collapse with better energy absorption performance. Numerical investigation showed the origami crush box absorbed significantly more energy than existing thin-walled crash boxes during a collision.

2.5.2 Programmable folding sheet

Origami can fold a flat sheet into three dimensional structures that can be utilized as robot bodies. In Hawkes' paper (Hawkes, An et al. 2010), the author defined the programmable matter as a material whose properties can be programmed to achieve specific shapes or levels of stiffness upon command (Guo, Li et al. 2009). The self-folding origami sheet that composed of universal crease patterns and interconnected triangular sections was designed and fabricated; it was one that could fold itself into a little boat and an airplane (Demaine and Demaine 2001; Benbernou, Demaine et al. 2009).

In (Byoungkwon and Rus 2012), a sheet with box-pleated patterns was used to realise self-folding robots. In (Onal, Wood et al. 2011, 2013), the laser-engraved origami patterns were employed to build a new class of robotic system. The shape memory alloy actuators were integrated into the structures to achieve programmable robots with precise actuation control and the planar fabrication of 3-D mechanisms. In (Felton, Tolley et al. 2014), a crawling robot

that folds itself was developed. Electronics and shape-memory composite was embedded on a flat sheet with patterns derived from computational origami.

2.5.3 Self-deployable origami stent graft

In (Kuribayashi, Tsuchiya et al. 2006), the origami patterned deployable cylinder was employed to build the stent graft for a biomedical application (Ryhänen 1999). The design, manufacturing and properties of a new type of stent graft, the origami stent graft, were presented. Unlike conventional stent grafts which consist of a wire mesh stent and a covering membrane, the new origami stent graft is made from a single foldable foil with hill and valley folds. The Ni-rich titanium/nickel (TiNi) shape memory alloy (SMA) foil made by the ultrafine laminates method was used in order to produce the stent graft (Reynaerts, Peirs et al. 1995). The pattern of folds on the foil was produced by negative photochemical etching (Allen 1986). The deployment of the stent graft is achieved either by SMA effect at the body temperature or by making use of the property of superelasticity. A number of prototypes of the stent graft, which are the same size as standard esophageal and aortal stent grafts, have been produced successfully.

2.5.4 Deployable structures for space structures

Deployable structures are widely used in space technology. Construction in low-gravity or zero-gravity environments is quite difficult, so space structures such as residential shelters are designed as deployable assemblies (Gruber, Häuplik et al. 2007). The solar panels (Rauschenbach. 1980; Malone, Crawford et al. 1993; Botke, Murphy et al. 2002), antennas (Onoda 1988; Kanemitsu 1998; Focatiis and Guest 2002) and masts (Bodle and Lungerhausen 1987; Tibert and Pellegrino 2003) of the satellites are generally deployable to keep the device compact during launch.

In (Gruber, Häuplik et al. 2007; Kiper and Soylemez 2009), the feasibility of applying deployable structures to build a human lunar base were studied.

Several potential ideas for deployable structures were introduced, which were assembled by planar panels connected by hinges. Their basic units can be repeatedly folded along the longitudinal axes to create self-deployable tubes. The suggestions could be fully deployed into large volume tubes or compactly folded into small volume packages (Guest and Pellegrino 1994; Buri and Weinand 2008; Kiper and Soylemez 2009).

2.6 Patterned sheet

Sandwich structures are widely used in the aircraft and automotive industries due to their high stiffness-to-weight ratio and configurable energy absorption performance (Lu and Yu 2003; Shen, Lu et al. 2013). However, the drawbacks of the conventional honeycomb cores, namely, the accumulation of humidity, the complicated manufacture process and the vulnerability against impact loads, limit the applications of the sandwich structures (Heimbs, Middendorf et al. 2007).

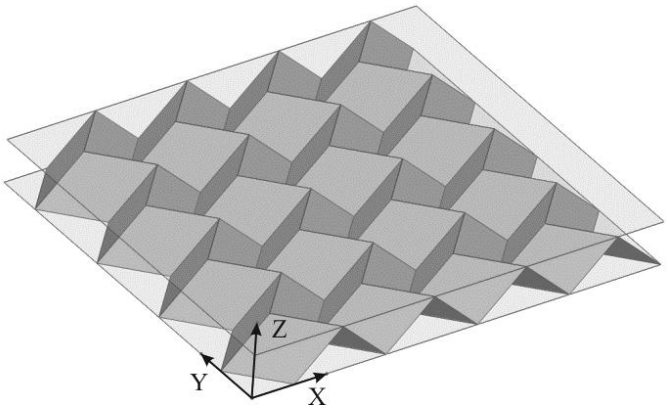

Fig. 2.5 The Miura-ori foldcore

Miura-ori patterned sheets can be used as the core of sandwich structures, see Fig. 2.5, which is called the foldcore, folded core, zeta-core, zigzag or chevron core. For obtaining high strength to weight ratios and overcoming the disadvantages of the known core structures, such as, manufacturing difficulties, expense of production, the required use of special assembly and fastening

techniques, and also to deal with the high operating temperatures resulting from skin friction in the aircraft, a new sandwich core was invented in (Rapp 1960). It could be folded from a single sheet or stripe material, with only bending operations. It provides flow paths through the structure for improved cooling effects and increases the strength properties in both shear and bending stress.

Miura (Miura 1972) derived the zeta-core by a topological transformation of a single plane. The core can be manufactured from a single sheet. It is easy to manufacture, scale independent, suitable for flat and curved sandwiches, able to circulating fluid between facings and its shear modulus can be controlled to be orthoropic and isotropic. The zeta-core made from aluminium, plastics and G.R.P sheet materials were presented.

In recent years, the studies on the Miura-ori inspired folded cores have gained great popularity in the fields of mathematics, physics and engineering. The relevant research is here reviewed and summarized as follows.

2.6.1 Design

Nojima (Nojima and Saito 2006) devised a series of core structures by folding thin flat sheets with periodically set slits or punched out portions into three dimensions. The geometries created by origami techniques are very complicated. The research studies were mainly focused on the relatively simple zigzag or chevron Miura-ori patterned cores and their variations.

Klett (Yves and Klaus 2011) explored two design strategies: bottom-up and top-down. The bottom-up approach derives a set of parametric equations that describe the folding kinematics of a certain unit cell type under the assumption of zero-thickness surfaces, and subsequently design the geometric and mechanical properties of the foldcore. The top-down approach is to directly generate unit cells that are suited for the desired application.

In (Schenk 2011c), Schenk focused on the folded sheet structures which only consisted of straight fold lines, planar facets and regular tiling of degree-4 vertices. The planar Miura and Eggbox sheets were used to investigate the mechanical properties.

Gattas and You have carried out a series of foldcore focused studies in recent years. Gattas (Gattas and You 2013b) conducted impact resistance analysis on five non-Miura patterns, namely the Eggbox, Pyramid 1 and 2, cube 1 and 2, which are also rigid-foldable and tessellated. The authors defined twelve parameters in the Miura pattern (Gattas, Wu et al. 2013a), including constants and pattern variables. Due to the six independent geometric relations established, six independent parameters are required to find all remaining parameters and a unique Miura pattern configuration. The first-level derivative patterns were generated by altering a single characteristic of the Miura pattern in turn. Crease orientation, crease alignment, developability, flat-foldability, and rectilinerarity were each altered. By modifying each characteristic, five derivative patterns, including the Arc, Arc-Miura, Non-Developable Miura, Non-Flat foldable Miura and tapered Miura patterns, were constructed in MATLAB and from sheet materials. The piecewise geometries assembled by the first-level derivatives were presented. In (Gattas and You 2014a), a new method was presented for generating and parameterising rigid-foldable, curved-crease geometries. By adding a single parameter to the straight-crease pattern, a curved-crease Miura pattern was generated and completely defined. The method was then used to generate the curved-crease variants of Tapered Miura, Arc, Arc Miura. To achieve higher and uniform energy absorption in (Gattas and You 2014b), the indented foldcore was created by placing sub-folds in the ridge of the standard form.

The wedge-shaped cores are relevant to the panels used in the wing of a small-sized aircraft. In (Zakirov and Alekseev 2010), the chevron folded structure, with units of variable heights, was folded into wedge geometry. The folding pattern and designing method were presented.

The configuration of the multilayer of foldcores has also been proposed and studied. In (Heimbs, Cichosz et al. 2010), a dual-core sandwich consisting of two layers of different fibre-reinforced composites (CFRP and AFRP) was investigated in a two-fold energy absorption process. Schenk and Guest stacked individual folded layers to form a cellular metamaterial, in which the layers were bonded along joining fold lines (Schenk and Guest 2013).

2.6.2 Manufacturing process

To manufacture the foldcore cost effectively and for it to have comparable performance to conventional cores, like the honeycomb, numerous different approaches have been proposed.

Schenk gave a comprehensive overview of the manufacturing methods where the sheet material is only subjected to bending operation and material strains are minimal (Schenk 2011c). The manufacturing processes were distinguished into synchronous, gradual folding and pre-gathering processes. In the synchronous processes, the folding of the ridges takes place simultaneously, whereas in the gradual folding processes, the sheet folds gradually from flat to a desired folded state. In the pre-gathering processes, the single corrugation and double corrugation of sheets are formed in succession. The synchronous processes can be vacuum or mechanically actuated; it also includes approaches such as the successive stamping and self-assembly of foldcore pattern. The gradual folding process can be achieved using a gradually deepening set of dies, or applying the patterning and gathering method. The pre-gathering processes were divided into sub-groups, which are the cylic forming, the bunch and crunch, the oscillating discs and the continuous inversion.

In (Schenk, Allwood et al. 2011a), a novel manufacturing process to fold a flat sheet into 3D structure was introduced, which used cold gas-pressure to fold the sheets with a perforation fold pattern. Between two parallel sheets, the spacers were placed along the mountain ridges. The combination was packed into an

air-tight bag which was evacuated to near vacuum. The external pressure was increased to create enough pressure difference to fold the sheet, and the fold depth is determined by the height of the spacers.

For an easy understanding, Heimbs classified the manufacturing processes into discontinuous and continuous processes (Heimbs 2013). Discontinuous manufacturing was found to be ideal to construct the limited size of foldcore prototypes in an interrupted process for research purposes. It involved methods such as cold gas-pressure folding (Schenk, Allwood et al. 2011a). The continuous manufacturing of the foldcore treats the sheet of material in a machine, where the forming of the structure is continuous. In (Elsayed and Basily 2004), foldcores were made by embossing and folding thin sheets of material. The continuous process allows for higher efficiency than the discontinuous process.

2.6.3 Material

A wide range of materials, which are not too brittle or too elastic, have been used to produce foldcores (Heimbs 2013). The materials were summarised into groups of metals, plastics, fibre-reinforced composites, aramid paper, cardboard/Kraft paper. The zeta-core was made from aluminium, plastics and G.R.P sheet materials in (Miura 1972). The paper, copper, aluminum and stainless steel sheets were used in (Elsayed and Basily 2004) to produce foldcores by a continuous process. The fibre-reinforced composites, namely the carbon fibre-reinforced composite (CFRP) and Aramid fibre-reinforced composite (ARFP), were tested in impact experiments in (Heimbs, Cichosz et al. 2010). The foldcores made from different materials, including carbon fibre-reinforced composite and Aramid fibre-reinforced composite and aluminum foil, and with different unit cell geometries were produced in (Fischer, Heimbs et al. 2009b). In (Gattas and You 2013b, 2014b), the prototypes of the Miura-ori derivatives are made from card paper, aluminium and polypropylene sheets.

2.6.4 Mechanical experiment

To explore the mechanical properties of the foldcore made from various materials, such as its Young's modulus, Passion ratio, stiffness, etc., comprehensive experiments with a series of load conditions have been conducted.

The Miura sheet and the Eggbox sheet were extended, twisted and bent by hand in (Schenk 2011c). Without stretching the facets, the folded sheets could undergo large deformation and change of their global Gaussian curvature. The Eggbox sheet displayed a positive Poisson's ratio under extension, but negative under bending. The Miura sheet behaves as an auxetic material (negative Poisson's ratio) in planar deformation, whilst it shows a typical behaviour for materials with a positive Poisson's ratio when subjected to bending.

In (Gattas and You 2014b), the indented foldcore was investigated using quasi-static impact test, which achieves a higher and more uniform energy absorption rate than the standard foldcore structure by triggering a high-order travelling hinge line failure mode. In (Gattas and You 2014c), two curved-crease foldcore tessellations were manufactured and investigated under quasi-static impact load. Their behaviors were compared with standard and indented foldcores, which showed the core aspect ratio has a greater effect on energy-absorption capabilities than the configuration of the tessellation, and that the curved-crease foldcores have significantly higher energy-absorption capability than straight-crease foldcores.

Heimbs carried out a serious of impact tests on foldcore sandwich structures made from fibre-reinforced composite materials. In (Heimbs, Middendorf et al. 2007), the foldcores made of phenolic resin-impregnated aramid paper and carbon fibre-reinforced plastics (CFRP) were tested in flatwise (out-of-plane) compression (DIN3291). The mechanical behaviour of the four types of textile-reinforced composite foldcores, including a dual-core configuration, was

studied in (Heimbs, Cichosz et al. 2010). The standard tests on the materials derived the mechanical properties. The flatwise compression and transverse shear tests were carried out on all the foldcore sandwiches. The low and high velocity impact tests were performed only on the types with greater energy absorption capability, i.e. type C and D, where the damages were assessed with the ultrasonic C-scans and Micro-CT scan images.

High-Rate Dynamic Compression Tests were performed in (Basily and Elsayed 2004; Elsayed and Basily 2004; Kazemahvazi, Kiele et al. 2010). Through quasi-static and dynamic compression tests, the out-of-plane impact properties of corrugated carbon fibre composite cores have been investigated in (Kazemahvazi, Kiele et al. 2010). Utilising a drop tower, the dynamic compression testing of laminated block of foldcore in out-of-plane direction and both in-plane directions has been documented in (Basily and Elsayed 2004; Elsayed and Basily 2004). The tests indicated the laminated block of foldcore, made from the Kraft paper, can surpass the honeycomb cores in energy absorption despite being made of the same material.

To investigate the impact behaviour and the subsequent residual strength in (Klaus and Reimerdes 2009), the impact and four-point-bending tests and the FE simulations were performed on the sandwich specimens with aramid paper foldcore and two CFRP shins. The influence of the impact on the bending behaviour of the sandwich structure was displayed. The three-point-bending tests were covered in (Basily and Elsayed 2005) on the Kraft paper foldcore. The effect of the geometry and orientation of the foldcore on flexural rigidity of the sandwich was investigated.

The mechanical properties of the materials, including carbon fibre-reinforced composite and Aramid fibre-reinforced composite and aluminum foil, were derived from the tension, compression, bending, and bulking tests. The flatwise compression and transverse shear tests in longitudinal and transverse directions

were performed on the foldcore sandwich structures (Fischer, Drechsler et al. 2009a; Fischer, Heimbs et al. 2009b).

2.6.5 Finite element simulation

In addition to those experiments, further investigation on the mechanical behavior of the foldcore under various loading conditions can be achieved in finite element simulations. A validated FE model of the specimen can provide comprehensive details, such as energy absorption, deformation pattern, crushing, etc. The geometry optimisation of the foldcore for specific requirements can also be derived. The essential aspects of a FE simulation include the software, material model, explicit and implicit simulation, sensitivity study and geometric imperfections. The explicit simulations are favourable to cover the strong nonlinearities and crushing of the foldcore, but for quasi-static loading an explicit simulation is time consuming. Thus, the sensitivity studies on the model size, element size/type, loading rate, mass scaling need to be carried out to obtain accurate simulation results within an acceptable timeframe. Geometric imperfections are sometimes considered to match potential defects on the specimens.

In (Gattas and You 2013b), to be compared with the typical Miura-ori pattern, Quasi-static impact loads in the *H* direction were applied to the models in ABAQUS/Explicit and two of them had comparable or improved energy-absorption capabilities, which are the cube 1 pattern and the Eggbox pattern. The prototypes of the cube 1 and Eggbox were constructed from polypropylene sheets. The experiments on the prototypes showed reasonable correlation with the numerical results. An optimum indented foldcore configuration was obtained using the numerical parametric study in (Gattas and You 2014b), it was followed by experimental analysis on the aluminium prototypes. The numerical and experimental results were compared, which lead to the conclusion that the travelling hinge behavior displays as predicted on the prototype without visible geometric imperfections. In (Gattas and You 2014c),

an optimisation study of the curved-crease foldcore was performed in Abaqus/Explicit, this provided comparable mechanical behaviors to a honeycomb core. The geometry imperfections were generated in the FE model.

In (Zhou, Wang et al. 2014), the virtual quasi-static tests were presented, namely, the compression in *H* direction, shearing and bending in two principal directions, both on standard and variations of the Muria-based foldcore models. The foldcore models with curved fold lines have superior mechanical properties in compression and shearing. The multilayer foldcore outperformed others in bending. The foldcores were also comparable to or exceeded the performance of the honeycomb core in shearing and bending tests.

In (Heimbs, Middendorf et al. 2007), the FE simulations with explicit solver PAM-CRUSH and LS-DYNA were validated by the experimental data. The FE model, focused on the imperfection of the cell wall and the representation of buckling, folding or crush phenomena, was proved to be a promising tool to obtain mechanical properties and optimise the geometry of a foldcore. In (Heimbs 2009), the virtual testing was carried out on four types of sandwich structures, either with hexagonal and over-expanded Nomex honeycomb core or with foldcores made of Kevlar paper and carbon fibre (CFRP), respectively. In the FE models, modelling for imperfections was included. The visual testing, including flatwise compression on all four types, a transverse shear on a hexagonal honeycomb and Kevlar foldcore sandwiches, and in-plane compression on a hexagonal honeycomb sandwich, obtained a good correlation with the experimental data. The analysis of the deformation patterns and failure modes, and the optimisation study of the CFRP foldcore with respect to its compressive behaviour were performed using the established model. In (Heimbs, Mehrens et al. 2007), the established model of Kevlar foldcore was used in the virtual quasi-static material testing, which included out-of-plane compression, in-plane compressions in two directions and shear tests in three directions. In (Heimbs, Cichosz et al. 2010), the experiment's data was used in simulations to define and validate the FE models of four types of composite

foldcores. The simulations showed good correlation with the experiments, which allowed the FE model to be employed for parameter studies, evaluations of damage patterns and energy absorption mechanisms.

To successfully apply the FE simulations to test the design of foldcore geometries and saving testing efforts, in (Fischer, Drechsler et al. 2009a), the mechanical properties of aramid paper were used for defining a material model. A user defined material law was programmed in FORTRAN and implemented in ABAQUS. The implicit simulations of the material tests and static tests on foldcore sandwich structures were performed in ABAQUS, whereas the explicit simulations were carried out in PAM-CRASH with a simplified material model. The simulation results showed a good correlation with the experimental data. The detailed mesoscale and the homogenized macroscale FE models of the foldcore were subsequently proposed and analysed in (Fischer, Heimbs et al. 2009b). The multiscale model, combining the mesoscale model and the macroscale model, was found to be efficient when simulating the low velocity impact loading on a local area. The geometrical imperfections of the cell walls were represented in the meso-model.

In (Baranger, Cluzel et al. 2011), in order to model the compaction behaviour of foldcore, a laminate like material model was proposed for the aramid paper based on the micro observations. The geometric defects were considered in the model of foldcore by perturbing the folding pattern; this led to the deformation shape in the implicit Abaqus simulation which agreed with the experimental results.

Sandmesh, developed using Ansys Parametric Design Language (APDL), was applied to mesh the sandwich structures in (Nguyen, Jacombs et al. 2005). The impact simulation in LS-Dyna was validated through the testing and analysis of aluminium honeycomb specimens. The Sandmesh was then applied to the foldcore sandwiches with composite skins to estimate the impact characteristics and to perform parametric studies on the foldcore.

2.6.6 Theoretical analysis

Theoretical methods are employed to explain the mechanism beneath the mechanical behavior of the foldcore. The sheer modulus of the zeta-core was obtained by an approximate analysis in (Miura 1972). As a result, any orthotropy including isotropy in shear modulus can be designed.

Kelsey et al. (Kelsey, Gellatly et al. 1958) proposed bounds for estimating the shear force stiffness of the sandwich panels within the honeycomb structure. To replace the action of the skins, a uniform shear stress/strain was applied directly to the core alone. Kelsey's unit load method (First Order Shear Deformation Theory) was then used in (Lebée and Sab 2010b) to derive the upper and lower bounds for the effective transverse shear modulus of a chevron foldcore. The results were compared to FE simulations, which showed loose correlation (more than 100% discrepancy). A more refined homogenization method, the Cecchi and Sad high order homogenization method (Cecchi and Sab 2007), was applied to compute the exact shear modulus in (Lebée and Sab 2010a), which takes the influence of the skins on the transverse shear stiffness into consideration. In (Lebée and Sab 2012), a new plate theory for thick plates, the Bending-Gradient plate theory (Lebée and Sab 2011), was applied to the sandwich structure with a chevron core. The skin distortion phenomenon was found to influence the shear force stiffness of the sandwich panel significantly.

In (Schenk, Allwood et al. 2011a), the required forming pressure of the cold gas-pressure manufacturing process was calculated using the principle of virtual work with three assumptions that the material was an ideal plastic, a plastic hinge was formed along each fold line and the folding process of the sheet can be represented by a single unit cell. The results were compared with experiments; these showed the calculation underestimated the required forming pressure. An improvement on the method could be achieved by a more accurate material model and consideration of large deformations. The folded sheets were modelled as pin-jointed frameworks in (Schenk and Guest 2011b, 2013), where

the fold lines and vertices were represented by bars and pin-joints. The underlying assumption was that the fold lines remained straight during deformation. To approximately represent the bending of facets in a first-order deformation and avoid trivial internal mechanisms, the parallelogram facets were triangulated by the short diagonal. This model enabled a transition from a purely kinematic to a stiffness matrix approach. The key mechanical behaviour observed in the paper models was successfully represented by the numerical model. The Miura fold pattern was proved to provide a negative Poisson's ratio for in-plane deformations and a positive Poisson's ratio for out-of-plane bending. Remarkably, these Poisson's ratios were equal and opposite. The model also indicated that the dominant mechanics of the folded sheets were a result of the geometry rather than the material properties.

It was also pointed out in (Wei, Guo et al. 2013) that the in-plane and out-of-plane Poisson's ratios were equal in magnitude, but opposite in sigh, independent of material properties. To describe out-of-plane bending deformation isometrically, a similar approach as in (Schenk and Guest 2013) was used, introducing the short diagonal fold to each facet. The effective bending stiffness of the unit cell was proved to be singular, allowing the two-dimentional deformation of Miura-ori plate to be described by a one-dimentional beam theory.

In (Tolman, Delimont et al. 2014), by applying compliant mechanism theory to a single fold of the origami-inspired structure, the fold was considered to be a small-length flexural pivot, which was further modeled as two rigid links that were pinned with a linear torsional spring, applying the pseudo-rigid-body-model (PRBM) approach (Howell 2001). To select materials for origami-inspired structures and meet the requirements, namely, elastic deformation, absorption of elastic strain energy, light weight and cost effective, two material indices were obtained. The FE simulations on the Miura-ori tessellation and triangular wave corrugation were performed to investigate the effects of the material stiffness (stiffness ratio) on the energy absorption and force

distribution characteristics. The Ashby plots for material selection were derived and then utilised in an application example.

In (Silverberg, Evans et al. 2014), each unit of the Miura-ori tessellation was described as mechanically bistable. By applying force to a vertex in the normal direction and popping it into a different mechanical stable state, it could be considered as the lattice defects (Pop-Through Defect) in the crystallographic structures. The Pop-Through Defects involve only elastic facet bending and hence are reversibly removable. As a result, the compressive modulus of the overall structure could be reversibly tuned. The programmable modulus was demonstrated in the experiments on Miura-ori folded sheets with a series of complex defect structures.

2.6.7 Application

The advanced properties of foldcore, namely, light weight, superior energy absorption, tunable mechanical properties, compatibility with wide range of material and simple manufacturing process lead to great deal of potential in application.

To avoid the water accumulation problem of the sandwich panels with honeycomb core, the sandwich structure with foldcore is suitable for the aircraft industry. It provides venting channels and comparable mechanical properties to a honeycomb core. Airbus has investigated sandwich with foldcore to replace the sandwich panels for the aircraft fuselage (Heimbs, Mehrens et al. 2007). The wedge-shape cores presented in (Zakirov and Alekseev 2010) can be used as an alternative solution to the current wing structure of a small-sized airplane. The soundproof characteristic of the sandwich plates with foldcore were investigated in (Wang and Xu 2006), which indicated that the double layers of foldcore can be utilised for soundproof devices. The foldcore structure can also be applied in other fields, such as packaging, civil infrastructures, transportation, military, etc., as listed in (Elsayed and Basily 2004).

Chapter 3

The Mobile Assemblies of Spherical 4*R* Linkages

3.1 Introduction

Spherical 4R linkage can be used as the basic element to construct deployable structures due to its one degree of freedom mobility. Here, a kinematic model of the mobile assemblies is proposed based on the closed adjacent assembly of four spherical 4R linkages. To obtain the assemblies of one degree of freedom, the kinematic compatibility conditions of the model will be studied. The solutions to the compatibility conditions will be derived, which will include the existing one-DOF mobile assemblies, as well as novel ones. Based on the solutions, the relationships between kinematic variables will be discovered. Hybrid assemblies, networks consisting of an unlimited number of linkages, and rigid origami patterns for flat surfaces will be obtained. To test and display the mobility of the assemblies, their simulation models will be built accordingly.

The layout of the chapter is as follows. Firstly, the kinematics of spherical 4R linkage will be introduced in section 3.2. Section 3.3 derives the one-DOF mobile assemblies of four spherical 4*R* linkages. In section 3.4, the discussions are carried out on relationships between kinematic variables, the hybrid assemblies, networks and rigid origami patterns for flat surface. The summary in section 3.5 ends the chapter.

3.2 The kinematics of the adjacent assembly of spherical 4*R* linkages and compatibility conditions

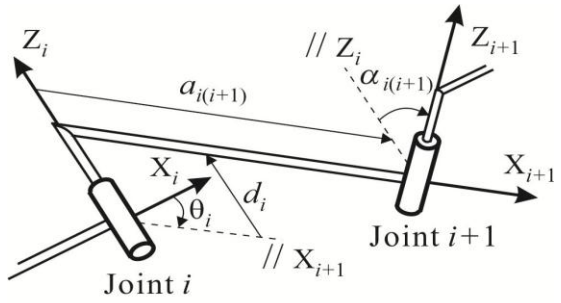

Fig. 3.1 Setup of the coordinate system and linkage geometric parameters in links (i-1)i and i(i+1) connected by joint i.

In Fig. 3.1, the coordinate frames for the links and joints are created by following the D-H parameters (Denavit and Hartenberg 1955), in which

Z_i Coordinate axis along the revolute axis of joint i;

X_i Coordinate axis commonly normal to Z_{i-1} and Z_i, and $X_i = Z_{i-1} \times Z_i$;

Y_i Coordinate axis commonly normal to X_i and Z_i, and $Y_i = Z_i \times X_i$;

θ_i Revolute variable of joint i, which is the rotation angle from X_i to X_{i+1}, positive about Z_i.

d_i Offset of joint i, which is the common normal distance from X_i to X_{i+1}, positive along axis Z_i;

$a_{i(i+1)}$ Length of link i(i+1), which is the common normal distance from Z_i to Z_{i+1}, positive along axis X_{i+1};

$\alpha_{i(i+1)}$ Twist of link $i(i+1)$, which is the rotation angle from Z_i to Z_{i+1}, positive about axis X_{i+1}.

Thus, the coordinate transformation from frame $\mathbf{F}_i : \mathrm{X}_i\ \mathrm{Y}_i\ \mathrm{Z}_i$ to frame $\mathbf{F}_{i+1} : \mathrm{X}_{i+1}\ \mathrm{Y}_{i+1}\ \mathrm{Z}_{i+1}$, which includes translations and rotations, can be represented as

$$\mathbf{R}_z(\theta_i)\mathbf{T}_z(d_i)\mathbf{T}_\mathbf{x}(a_{i(i+1)})\mathbf{R}_\mathbf{x}(\alpha_{i(i+1)})\mathbf{F_i} = \mathbf{F_{i+1}}, \tag{3.1}$$

in which,

$$\mathbf{R}_\mathrm{z}(\theta_i) = \begin{bmatrix} \cos\theta_i & -\sin\theta_i & 0 & 0 \\ \sin\theta_i & \cos\theta_i & 0 & 0 \\ 0 & 0 & 1 & 0 \\ 0 & 0 & 0 & 1 \end{bmatrix} \tag{3.2}$$

are the homogeneous matrices of rotation θ_i about axis Z_i,

$$\mathbf{T}_\mathrm{z}(d_i) = \begin{bmatrix} 1 & 0 & 0 & 0 \\ 0 & 1 & 0 & 0 \\ 0 & 0 & 1 & d_i \\ 0 & 0 & 0 & 1 \end{bmatrix} \tag{3.3}$$

is the translation d_i along axis Z_i,

$$\mathbf{T}_\mathrm{x}(a_{i(i+1)}) = \begin{bmatrix} 1 & 0 & 0 & a_{i(i+1)} \\ 0 & 1 & 0 & 0 \\ 0 & 0 & 1 & 0 \\ 0 & 0 & 0 & 1 \end{bmatrix} \tag{3.4}$$

is the translation $a_{i(i+1)}$ along axis X_{i+1}, and

$$\mathbf{R}_{\mathrm{x}}(\alpha_{i(i+1)})=\begin{bmatrix}1 & 0 & 0 & 0\\ 0 & \cos\alpha_{i(i+1)} & -\sin\alpha_{i(i+1)} & 0\\ 0 & \sin\alpha_{i(i+1)} & \cos\alpha_{i(i+1)} & 0\\ 0 & 0 & 0 & 1\end{bmatrix} \tag{3.5}$$

is the rotation $\alpha_{i(i+1)}$ about axis X_{i+1}.

For a general spherical 4*R* linkage, all four revolute axes intersect at one vertex, as shown in Fig. 3.2. Hence, its parameters are

$$\begin{aligned} d_1 = d_2 = d_3 = d_4 = 0;\\ a_{12} = a_{23} = a_{34} = a_{41} = 0. \end{aligned} \tag{3.6}$$

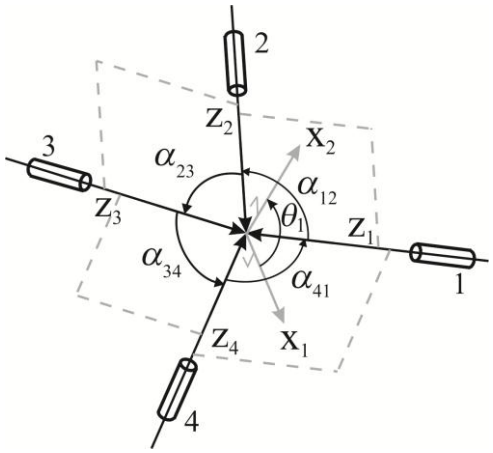

Fig. 3.2 Definition of a single spherical 4*R* linkage.

According to the D-H matrix method, the closure condition of the general spherical 4*R* linkage is

$$\mathbf{R}_{\mathrm{z}}(\theta_1)\mathbf{R}_{\mathrm{x}}(\alpha_{12})\mathbf{R}_{\mathrm{z}}(\theta_2)\mathbf{R}_{\mathrm{x}}(\alpha_{23})\mathbf{R}_{\mathrm{z}}(\theta_3)\mathbf{R}_{\mathrm{x}}(\alpha_{34})\mathbf{R}_{\mathrm{z}}(\theta_4)\mathbf{R}_{\mathrm{x}}(\alpha_{41})=\mathbf{I}, \tag{3.7}$$

which can be rearranged into two forms,

$$\mathbf{R}_z(\theta_1)\mathbf{R}_x(\alpha_{12})\mathbf{R}_z(\theta_2)\mathbf{R}_x(\alpha_{23}) = \mathbf{R}_x^{-1}(\alpha_{41})\mathbf{R}_z^{-1}(\theta_4)\mathbf{R}_x^{-1}(\alpha_{34})\mathbf{R}_z^{-1}(\theta_3), \tag{3.8}$$

$$\mathbf{R}_z(\theta_2)\mathbf{R}_x(\alpha_{23})\mathbf{R}_z(\theta_3)\mathbf{R}_x(\alpha_{34}) = \mathbf{R}_x^{-1}(\alpha_{12})\mathbf{R}_z^{-1}(\theta_1)\mathbf{R}_x^{-1}(\alpha_{41})\mathbf{R}_z^{-1}(\theta_4). \tag{3.9}$$

Eqns. (3.8) and (3.9) are expanded and the corresponding elements of the matrices at the left and right side of equations, $\mathbf{M}^L$ and $\mathbf{M}^R$ respectively, must be equal. Considering $\mathbf{M}_{3,3}^L = \mathbf{M}_{3,3}^R$ in both equations, the relationships between the revolute variables of two opposite joints, θ_i and θ_{i+2}, i.e. $\cos\theta_{i+2} = f_{i(i+2)}(\cos\theta_i)$, can be obtained as

$$\begin{aligned} &\frac{\cos\alpha_{(i+1)(i+2)}\cos\alpha_{(i+2)(i-1)} - \cos\alpha_{i(i+1)}\cos\alpha_{(i-1)i}}{\sin\alpha_{(i+1)(i+2)}\sin\alpha_{(i+2)(i-1)}} \\ &+\frac{\sin\alpha_{i(i+1)}\sin\alpha_{(i-1)i}}{\sin\alpha_{(i+1)(i+2)}\sin\alpha_{(i+2)(i-1)}}\cos\theta_i = \cos\theta_{i+2}, \end{aligned} \tag{3.10}$$

in which $i = 1, 2, 3, 4$ and cycles counter-clockwise as shown in Fig. 3.2. Considering $\mathbf{M}_{3,3}^L = \mathbf{M}_{3,3}^R$, $\mathbf{M}_{2,3}^L = \mathbf{M}_{2,3}^R$ and $\mathbf{M}_{3,2}^L = \mathbf{M}_{3,2}^R$, the relationships between two adjacent revolute variables θ_i and θ_{i+1}, i.e. $\theta_{i+1} = f_{i(i+1)}(\theta_i)$, are obtained.

$$\begin{aligned} &\cos\alpha_{(i+1)(i+2)}\sin\alpha_{(i-1)i}\sin\alpha_{i(i+1)}\cos\theta_i \\ &+\cos\alpha_{(i-1)i}\sin\alpha_{i(i+1)}\sin\alpha_{(i+1)(i+2)}\cos\theta_{i+1} \\ &-\sin\alpha_{(i-1)i}\sin\alpha_{(i+1)(i+2)}\sin\theta_i\sin\theta_{i+1} \\ &+\cos\alpha_{i(i+1)}\sin\alpha_{(i-1)i}\sin\alpha_{(i+1)(i+2)}\cos\theta_i\cos\theta_{i+1} \\ &+\cos\alpha_{(i+2)(i-1)} - \cos\alpha_{(i-1)i}\cos\alpha_{i(i+1)}\cos\alpha_{(i+1)(i+2)} = 0. \end{aligned} \tag{3.11}$$

Thus, when geometric parameters $\alpha_{i(i+1)}$ of a spherical 4*R* linkage are assigned, with one input rotation angle θ_i, the other 3 rotation angles can be derived, which confirms that a spherical 4*R* linkage is a one-DOF mechanism.

An assembly of two spherical 4*R* linkages, *j* and *j* + 1, is shown in Fig. 3.3. Notation *j* represents the spherical 4*R* linkages, where *j* = I, II, III…*N*. Thus, parameters $\alpha_{i(i+1)}^{j}$, θ_i^j, X_i^j, Z_i^j and f^j represent the twist $\alpha_{i(i+1)}$, the revolute variable θ_i, the axis X_i, the axis Z_i and function f of linkage *j*, respectively. Length L_{j+1}^{j} is the distance between the vertices of linkage *j* and *j*+1. The axes Z_i^j and Z_i^{j+1} are aligned, but in opposite directions to ensure the axes of each spherical 4*R* linkages are always pointed to its own sphere center. Then the links *i*(*i*+1) of linkage *j* and (*i*-1)*i* of linkage *j*+1, are integrated into one link. So are the links (*i*-1)*i* of linkage *j* and *i*(*i*+1) of linkage *j*+1. Therefore, the rotation angles θ_i^j and θ_i^{j+1} are synchronized during the movement of the assembly, i.e.

$$\Delta\theta_i^j = \Delta\theta_i^{j+1} \tag{3.12}$$

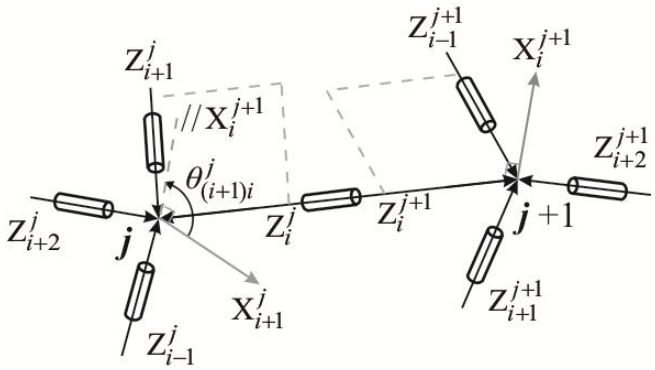

Fig. 3.3 An assembly of two spherical 4*R* linkages.

The plane $\mathrm{Z}_i^j \times \mathrm{Z}_{i+1}^j$ does not necessarily coincide with $\mathrm{Z}_{i-1}^{j+1} \times \mathrm{Z}_i^{j+1}$, i.e. their normal vectors X_{i+1}^j and X_i^{j+1} are not parallel. Thus, $\theta_{(i+1)i}^j$ is defined as the

rotation angle from axis X_{i+1}^{j} to X_{i}^{j+1}, positively about Z_{i}^{j}. $\theta_{(i+1)i}^{j}$ is a constant when the assembly is set up.

To study mobile assemblies, the spherical 4*R* linkages are assembled into chains in such a way that the shared joints in one linkage are adjacent, for example, the shared joints in linkage I, I1 and I2, are adjacent joints as shown in Fig. 3.4. This method of assembling the spherical 4*R* linkages is called *adjacent assembly*. Because the facets of the mobile assemblies we studied are quadrilaterals, only four linkages are assembled into a closed chain, which is considered as a unit. In a unit, the twists $\alpha_{i(i+1)}$ are constant geometric parameters, while rotation angles θ_i are kinematic variables. To simplify the assembly, the following assumption is made,

$$\theta_{32}^{\mathrm{I}} = \theta_{43}^{\mathrm{II}} = \theta_{14}^{\mathrm{III}} = \theta_{21}^{\mathrm{IV}} = 0, \tag{3.13}$$

which ensures the normal vectors $X_3^{\mathrm{I}} \perp X_2^{\mathrm{II}}$, $X_4^{\mathrm{II}} \perp X_3^{\mathrm{III}}$, $X_1^{\mathrm{III}} \perp X_4^{\mathrm{IV}}$ and $X_2^{\mathrm{IV}} \perp X_1^{\mathrm{I}}$. Due to the Eqns. (3.12) and (3.13), rotation angles θ_i should satisfy following relationships.

$$\theta_2^{\mathrm{I}} = \theta_2^{\mathrm{II}}, \theta_3^{\mathrm{II}} = \theta_3^{\mathrm{III}}, \theta_4^{\mathrm{III}} = \theta_4^{\mathrm{IV}}, \theta_1^{\mathrm{IV}} = \theta_1^{\mathrm{I}}. \tag{3.14}$$

Thus, $X_2^{\mathrm{I}} \perp X_3^{\mathrm{II}} \perp X_4^{\mathrm{III}} \perp X_1^{\mathrm{IV}}$ and the central facet I-II-III-IV is a planar quadrilateral. Thus, the sum of twist angles is always

$$\alpha_{12}^{\mathrm{I}} + \alpha_{23}^{\mathrm{II}} + \alpha_{34}^{\mathrm{III}} + \alpha_{41}^{\mathrm{IV}} = 2\pi. \tag{3.15}$$

Conditions in (3.13) and (3.14) ensure the closed adjacent assembly can be constructed by nine rigid flat panels connecting each other with revolute joints.

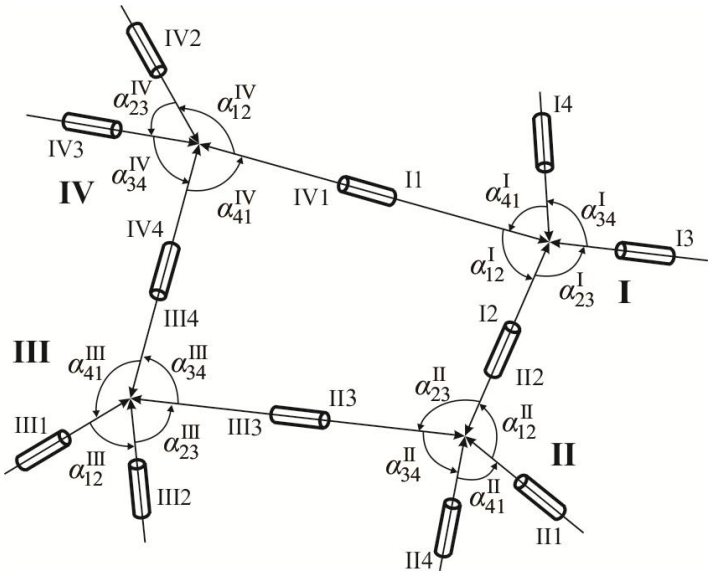

Fig. 3.4 The closed adjacent assembly of four spherical 4*R* linkages

3.2.1 The kinematic compatibility condition

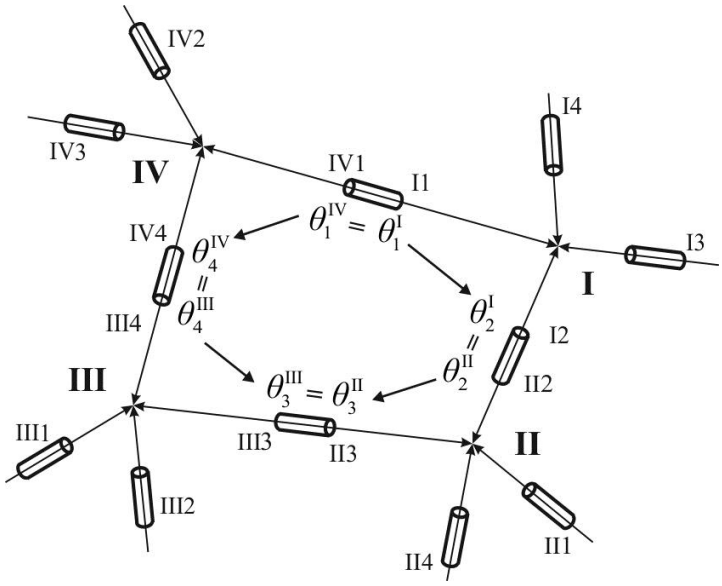

Fig. 3.5 The input and output relationship of the rotation angles in the closed adjacent assembly.

As shown in Fig. 3.5, the closed assembly can be considered as an open chain closed by connecting its head and tail. Rotation angles θ_1^{I} and θ_1^{IV} are

considered as inputs, through two paths on opposite sides to derive the outputs θ_3^{II} and θ_3^{III}, respectively. Due to the existing relationship in (3.14), the closure condition is

$$f_{23}^{\mathrm{II}}(f_{12}^{\mathrm{I}}(\theta_1^{\mathrm{I}})) = \theta_3^{\mathrm{II}} = \theta_3^{\mathrm{III}} = f_{34}^{-\mathrm{III}}(f_{41}^{-\mathrm{IV}}(\theta_1^{\mathrm{IV}})), \tag{3.16}$$

in which $f_{41}^{-\mathrm{IV}}$ and $f_{34}^{-\mathrm{III}}$ are the inverse function of f_{41}^{IV} and f_{34}^{III}. Eqn. (3.16) describes the kinematic compatibility conditions of the closed adjacent assembly. After substituting equation (3.11) into (3.16) and eliminating θ_2^{I}, θ_2^{II}, θ_4^{III} and θ_4^{IV}, formulas $f_{23}^{\mathrm{II}}(f_{12}^{\mathrm{I}}(\theta_1^{\mathrm{I}})) = \theta_3^{\mathrm{II}}$ and $\theta_3^{\mathrm{III}} = f_{34}^{-\mathrm{III}}(f_{41}^{-\mathrm{IV}}(\theta_1^{\mathrm{IV}}))$ can be represented as follows, respectively.

$$\begin{aligned}&(A1A2 - A3A4)^2\\ &+4(\mathrm{s}\alpha_{23}^{\mathrm{I}}\,\mathrm{s}\alpha_{41}^{\mathrm{I}}\,\mathrm{s}\theta_1^{\mathrm{I}}A2 - \mathrm{s}\alpha_{12}^{\mathrm{II}}\,\mathrm{s}\alpha_{34}^{\mathrm{II}}\,\mathrm{s}\theta_3^{\mathrm{II}}A4)(\mathrm{s}\alpha_{23}^{\mathrm{I}}\,\mathrm{s}\alpha_{41}^{\mathrm{I}}\,\mathrm{s}\theta_1^{\mathrm{I}}A3 - \mathrm{s}\alpha_{12}^{\mathrm{II}}\,\mathrm{s}\alpha_{34}^{\mathrm{II}}\,\mathrm{s}\theta_3^{\mathrm{II}}A1) = 0,\end{aligned} \tag{3.17}$$

$$\begin{aligned}&(A'1A'2 - A'3A'4)^2\\ &+4(\mathrm{s}\alpha_{23}^{\mathrm{III}}\,\mathrm{s}\alpha_{41}^{\mathrm{III}}\,\mathrm{s}\theta_3^{\mathrm{III}}A'2 - \mathrm{s}\alpha_{12}^{\mathrm{IV}}\,\mathrm{s}\alpha_{34}^{\mathrm{IV}}\,\mathrm{s}\theta_1^{\mathrm{IV}}A'4)(\mathrm{s}\alpha_{23}^{\mathrm{III}}\,\mathrm{s}\alpha_{41}^{\mathrm{III}}\,\mathrm{s}\theta_3^{\mathrm{III}}A'3 - \mathrm{s}\alpha_{12}^{\mathrm{IV}}\,\mathrm{s}\alpha_{34}^{\mathrm{IV}}\,\mathrm{s}\theta_1^{\mathrm{IV}}A'1) = 0,\end{aligned} \tag{3.18}$$

in which,

$$A1 = \mathrm{s}(\alpha_{12}^{\mathrm{I}} + \alpha_{23}^{\mathrm{I}})\,\mathrm{s}\alpha_{41}^{\mathrm{I}}\,\mathrm{c}\theta_1^{\mathrm{I}} - \mathrm{c}(\alpha_{12}^{\mathrm{I}} + \alpha_{23}^{\mathrm{I}})\mathrm{c}\alpha_{41}^{\mathrm{I}} + \mathrm{c}\alpha_{34}^{\mathrm{I}},$$

$$A2 = \mathrm{s}(\alpha_{23}^{\mathrm{II}} - \alpha_{12}^{\mathrm{II}})\,\mathrm{s}\alpha_{34}^{\mathrm{II}}\,\mathrm{c}\theta_3^{\mathrm{II}} - \mathrm{c}(\alpha_{23}^{\mathrm{II}} - \alpha_{12}^{\mathrm{II}})\mathrm{c}\alpha_{34}^{\mathrm{II}} + \mathrm{c}\alpha_{41}^{\mathrm{II}},$$

$$A3 = \mathrm{s}(\alpha_{23}^{\mathrm{II}} + \alpha_{12}^{\mathrm{II}})\,\mathrm{s}\alpha_{34}^{\mathrm{II}}\,\mathrm{c}\theta_3^{\mathrm{II}} - \mathrm{c}(\alpha_{23}^{\mathrm{II}} + \alpha_{12}^{\mathrm{II}})\,\mathrm{c}\alpha_{34}^{\mathrm{II}} + \mathrm{c}\alpha_{41}^{\mathrm{II}},$$

$$A4 = \mathrm{s}(\alpha_{12}^{\mathrm{I}} - \alpha_{23}^{\mathrm{I}})\,\mathrm{s}\alpha_{41}^{\mathrm{I}}\,\mathrm{c}\theta_1^{\mathrm{I}} - \mathrm{c}(\alpha_{12}^{\mathrm{I}} - \alpha_{23}^{\mathrm{I}})\,\mathrm{c}\alpha_{41}^{\mathrm{I}} + \mathrm{c}\alpha_{34}^{\mathrm{I}},$$

$$A'1 = \mathrm{s}(\alpha_{34}^{\mathrm{III}} + \alpha_{41}^{\mathrm{III}})\,\mathrm{s}\,\alpha_{23}^{\mathrm{III}}\,\mathrm{c}\,\theta_{3}^{\mathrm{III}} - \mathrm{c}(\alpha_{34}^{\mathrm{III}} + \alpha_{41}^{\mathrm{III}})\mathrm{c}\alpha_{23}^{\mathrm{III}} + \mathrm{c}\alpha_{12}^{\mathrm{III}},$$

$$A'2 = \mathrm{s}(\alpha_{41}^{\mathrm{IV}} - \alpha_{34}^{\mathrm{IV}})\,\mathrm{s}\,\alpha_{12}^{\mathrm{IV}}\,\mathrm{c}\,\theta_{1}^{\mathrm{IV}} - \mathrm{c}(\alpha_{41}^{\mathrm{IV}} - \alpha_{34}^{\mathrm{IV}})\mathrm{c}\alpha_{12}^{\mathrm{IV}} + \mathrm{c}\alpha_{23}^{\mathrm{IV}},$$

$$A'3 = \mathrm{s}(\alpha_{41}^{\mathrm{IV}} + \alpha_{34}^{\mathrm{IV}})\,\mathrm{s}\,\alpha_{12}^{\mathrm{IV}}\,\mathrm{c}\,\theta_{1}^{\mathrm{IV}} - \mathrm{c}(\alpha_{41}^{\mathrm{IV}} + \alpha_{34}^{\mathrm{IV}})\mathrm{c}\alpha_{12}^{\mathrm{IV}} + \mathrm{c}\alpha_{23}^{\mathrm{IV}},$$

$$A'4 = \mathrm{s}(\alpha_{34}^{\mathrm{III}} - \alpha_{41}^{\mathrm{III}})\,\mathrm{s}\,\alpha_{23}^{\mathrm{III}}\,\mathrm{c}\,\theta_{3}^{\mathrm{III}} - \mathrm{c}(\alpha_{34}^{\mathrm{III}} - \alpha_{41}^{\mathrm{III}})\mathrm{c}\alpha_{23}^{\mathrm{III}} + \mathrm{c}\alpha_{12}^{\mathrm{III}},$$

where "c" is for "cos" and "s" is for "sin". Eqn. (3.17) represents the relationship between θ_1^{I} and θ_3^{II}, Eqn. (3.18) represents the relationship between θ_1^{IV} and θ_3^{III}. It appears that the distances between linkages are not involved in the kinematic compatibility condition. Thus, the mobility of the assembly is scale-independent. In order to satisfy the compatibility condition, Eqns. (3.17) and (3.18) must be satisfied simultaneously. The derivation of Eqn. (3.17) and (3.18) is presented in Appendix A.

3.3 The one-DOF mobile assemblies

By solving the compatibility conditions using four approaches, four groups of one-DOF mobile assemblies can be obtained.

3.3.1 Group one

To reduce the complexity of the closed chain, Let

$$\theta_i^{\mathrm{I}} = \theta_i^{\mathrm{II}}, \quad \theta_i^{\mathrm{III}} = \theta_i^{\mathrm{IV}}, \tag{3.19}$$

the following relationships can be obtained

$$\alpha_{i(i+1)}^{\mathrm{I}} = \alpha_{i(i+1)}^{\mathrm{II}}, \quad \alpha_{i(i+1)}^{\mathrm{III}} = \alpha_{i(i+1)}^{\mathrm{IV}}. \tag{3.20}$$

Thus, linkages I and II are identical, and linkages III and IV are identical. Substituting Eqn. (3.20) into (3.17) and (3.18), and solving the equations, a group of mobile assemblies are derived, which are listed in Table 3.1. Among the assemblies in group one, 7 types, from type ID2 to ID8, are first introduced.

Table 3.1 Mobile assemblies group one

<table>
<tr><th>Name</th><th>Assumption</th><th>Relationships of θ_1^{I} and θ_3^{II}</th><th>Shape of central facet</th></tr>
<tr><td>Identical linkage</td><td rowspan="8">$\theta_i^{\mathrm{I}} = \theta_i^{\mathrm{II}}$,
$\theta_i^{\mathrm{III}} = \theta_i^{\mathrm{IV}}$</td><td rowspan="2">$\mathrm{s}\alpha_{23}^{\mathrm{I}}\,\mathrm{s}\alpha_{34}^{\mathrm{I}}\,\mathrm{c}\theta_3^{\mathrm{II}} - \mathrm{c}\alpha_{23}^{\mathrm{I}}\,\mathrm{c}\alpha_{34}^{\mathrm{I}}$
$= \mathrm{s}\alpha_{12}^{\mathrm{I}}\,\mathrm{s}\alpha_{41}^{\mathrm{I}}\,\mathrm{c}\theta_1^{\mathrm{I}} - \mathrm{c}\alpha_{12}^{\mathrm{I}}\mathrm{c}\alpha_{41}^{\mathrm{I}}$</td><td rowspan="2">convex quadrilateral</td></tr>
<tr><td>ID2</td></tr>
<tr><td>ID3</td><td rowspan="4">$\theta_1^{\mathrm{I}} = \theta_3^{\mathrm{II}}$</td><td rowspan="2">convex quadrilateral with $\alpha_{12}^{\mathrm{I}} = \alpha_{23}^{\mathrm{II}}$</td></tr>
<tr><td>ID4</td></tr>
<tr><td>ID5</td><td rowspan="3">convex quadrilateral</td></tr>
<tr><td>ID6</td></tr>
<tr><td>ID7</td><td>$\theta_1^{\mathrm{I}} + \theta_3^{\mathrm{II}} = 2\pi$</td></tr>
<tr><td>ID8</td><td>$\theta_1^{\mathrm{I}} + \theta_3^{\mathrm{II}} = \pi$</td></tr>
</table>

(1) Identical linkage type

$$\alpha_{i(i+1)}^{\mathrm{I}} = \alpha_{i(i+1)}^{\mathrm{II}} = \alpha_{i(i+1)}^{\mathrm{III}} = \alpha_{i(i+1)}^{\mathrm{IV}}. \tag{3.21}$$

According to (3.21), all four linkages in this assembly are identical. The linkages connect with each other in a rotational fashion (see Fig. 3.6). This assembly can be built by assembling identical convex quadrilaterals. This type was first introduced in (Kokotsakis 1933) and interpreted by the assembly of spherical 4*R* linkages recently in (Wang and Chen 2010).

(2) Type ID2

The twist angles of linkages I and II are supplementary to the corresponding angles of linkages III and IV (see Fig. 3.7) as follows,

$$\alpha_{i(i+1)}^{\mathrm{I}} = \alpha_{i(i+1)}^{\mathrm{II}} = \pi - \alpha_{i(i+1)}^{\mathrm{III}} = \pi - \alpha_{i(i+1)}^{\mathrm{IV}}. \tag{3.22}$$

(3) Type ID3

In linkages I and II, adjacent angles are equal; in linkages III and IV, opposite angles are equal (see Fig. 3.8).

$$\begin{aligned} &\alpha_{12}^{\mathrm{I}} = \alpha_{23}^{\mathrm{I}} = \alpha_{12}^{\mathrm{II}} = \alpha_{23}^{\mathrm{II}}; \\ &\alpha_{34}^{\mathrm{I}} = \alpha_{41}^{\mathrm{I}} = \alpha_{34}^{\mathrm{II}} = \alpha_{41}^{\mathrm{II}}; \\ &\alpha_{12}^{\mathrm{III}} = \alpha_{34}^{\mathrm{III}} = \alpha_{12}^{\mathrm{IV}} = \alpha_{34}^{\mathrm{IV}}; \\ &\alpha_{23}^{\mathrm{III}} = \alpha_{41}^{\mathrm{III}} = \alpha_{23}^{\mathrm{IV}} = \alpha_{41}^{\mathrm{IV}}. \end{aligned} \tag{3.23}$$

(4) Type ID4

In linkages I and II, adjacent angles are equal; opposite angles are supplementary in linkages III and IV (see Fig. 3.9).

$$\begin{aligned} &\alpha_{12}^{\mathrm{I}} = \alpha_{23}^{\mathrm{I}} = \alpha_{12}^{\mathrm{II}} = \alpha_{23}^{\mathrm{II}}; \\ &\alpha_{34}^{\mathrm{I}} = \alpha_{41}^{\mathrm{I}} = \alpha_{34}^{\mathrm{II}} = \alpha_{41}^{\mathrm{II}}; \\ &\alpha_{12}^{\mathrm{III}} = \pi - \alpha_{34}^{\mathrm{III}} = \alpha_{12}^{\mathrm{IV}} = \pi - \alpha_{34}^{\mathrm{IV}}; \\ &\alpha_{23}^{\mathrm{III}} = \pi - \alpha_{41}^{\mathrm{III}} = \alpha_{23}^{\mathrm{IV}} = \pi - \alpha_{41}^{\mathrm{IV}}. \end{aligned} \tag{3.24}$$

(5) Type ID5

Opposite angles in every linkage are equal (see Fig. 3.10).

$$\begin{aligned}
&\alpha_{12}^{\mathrm{I}} = \alpha_{34}^{\mathrm{I}} = \alpha_{12}^{\mathrm{II}} = \alpha_{34}^{\mathrm{II}},\\
&\alpha_{23}^{\mathrm{I}} = \alpha_{41}^{\mathrm{I}} = \alpha_{23}^{\mathrm{II}} = \alpha_{41}^{\mathrm{II}},\\
&\alpha_{12}^{\mathrm{III}} = \alpha_{34}^{\mathrm{III}} = \alpha_{12}^{\mathrm{IV}} = \alpha_{34}^{\mathrm{IV}},\\
&\alpha_{23}^{\mathrm{III}} = \alpha_{41}^{\mathrm{III}} = \alpha_{23}^{\mathrm{IV}} = \alpha_{41}^{\mathrm{IV}}.
\end{aligned} \tag{3.25}$$

(6) Type ID6

In linkages I and II, opposite angles are equal. In linkages III and IV, opposite angles are supplementary (see Fig. 3.11).

$$\begin{aligned}
&\alpha_{12}^{\mathrm{I}} = \alpha_{34}^{\mathrm{I}} = \alpha_{12}^{\mathrm{II}} = \alpha_{34}^{\mathrm{II}},\\
&\alpha_{23}^{\mathrm{I}} = \alpha_{41}^{\mathrm{I}} = \alpha_{23}^{\mathrm{II}} = \alpha_{41}^{\mathrm{II}},\\
&\alpha_{12}^{\mathrm{III}} = \pi - \alpha_{34}^{\mathrm{III}} = \alpha_{12}^{\mathrm{IV}} = \pi - \alpha_{34}^{\mathrm{IV}},\\
&\alpha_{23}^{\mathrm{III}} = \pi - \alpha_{41}^{\mathrm{III}} = \alpha_{23}^{\mathrm{IV}} = \pi - \alpha_{41}^{\mathrm{IV}}.
\end{aligned} \tag{3.26}$$

(7) Type ID7

Opposite angles in every linkage are supplementary (see Fig. 3.12).

$$\begin{aligned}
&\alpha_{12}^{\mathrm{I}} = \pi - \alpha_{34}^{\mathrm{I}} = \alpha_{12}^{\mathrm{II}} = \pi - \alpha_{34}^{\mathrm{II}},\\
&\alpha_{23}^{\mathrm{I}} = \pi - \alpha_{41}^{\mathrm{I}} = \alpha_{23}^{\mathrm{II}} = \pi - \alpha_{41}^{\mathrm{II}},\\
&\alpha_{12}^{\mathrm{III}} = \pi - \alpha_{34}^{\mathrm{III}} = \alpha_{12}^{\mathrm{IV}} = \pi - \alpha_{34}^{\mathrm{IV}},\\
&\alpha_{23}^{\mathrm{III}} = \pi - \alpha_{41}^{\mathrm{III}} = \alpha_{23}^{\mathrm{IV}} = \pi - \alpha_{41}^{\mathrm{IV}}.
\end{aligned} \tag{3.27}$$

(8) Type ID8

In each linkage, there is an angle larger than π (see Fig. 3.13).

$$\begin{aligned}
&\alpha_{12}^{\mathrm{I}} = 2\pi - \alpha_{34}^{\mathrm{I}} = \alpha_{12}^{\mathrm{II}} = 2\pi - \alpha_{34}^{\mathrm{II}},\\
&\alpha_{23}^{\mathrm{I}} = \alpha_{41}^{\mathrm{I}} = \alpha_{23}^{\mathrm{II}} = \alpha_{41}^{\mathrm{II}},\\
&\alpha_{12}^{\mathrm{III}} = 2\pi - \alpha_{34}^{\mathrm{III}} = \alpha_{12}^{\mathrm{IV}} = 2\pi - \alpha_{34}^{\mathrm{IV}},\\
&\alpha_{23}^{\mathrm{III}} = \alpha_{41}^{\mathrm{III}} = \alpha_{23}^{\mathrm{IV}} = \alpha_{41}^{\mathrm{IV}}.
\end{aligned} \tag{3.28}$$

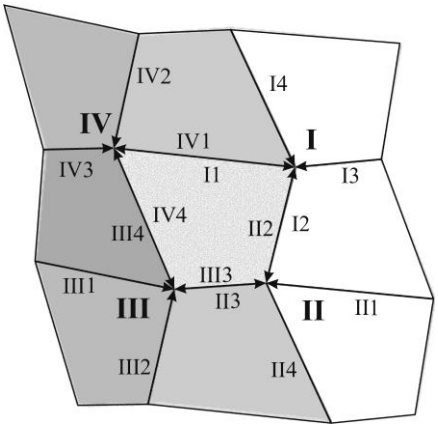

Fig. 3.6 Identical linkage type.

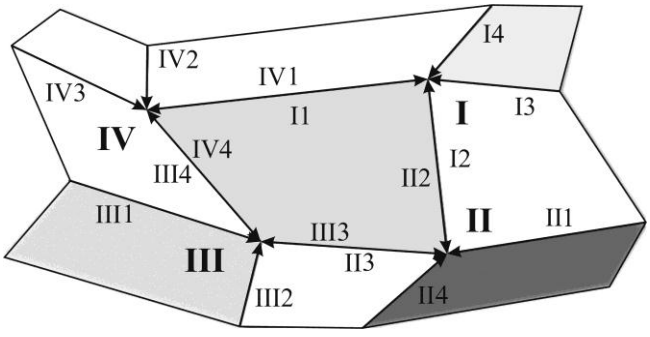

Fig. 3.7 Type ID2.

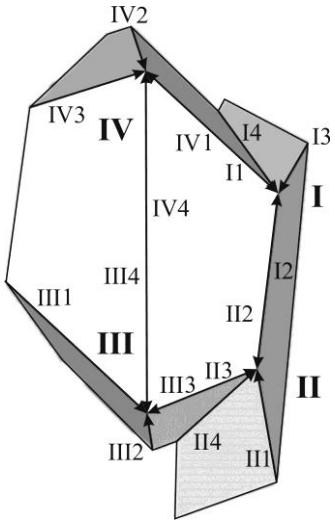

Fig. 3.8 Type ID3.

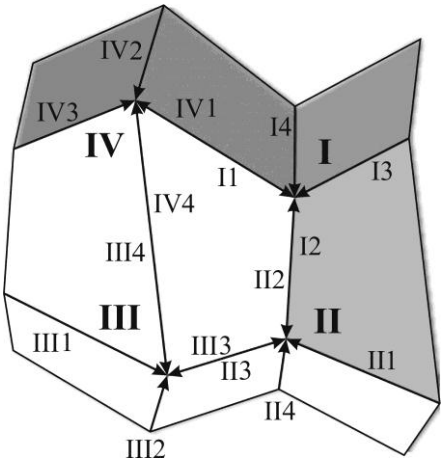

Fig. 3.9 Type ID4.

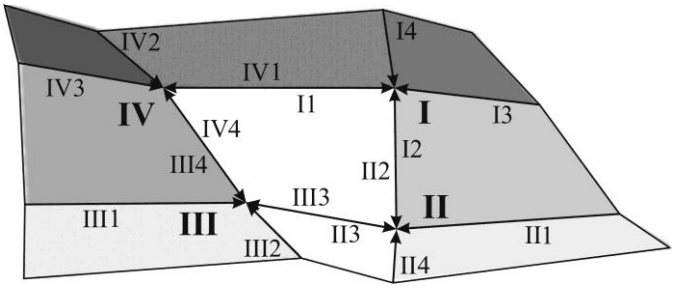

Fig. 3.10 Type ID5.

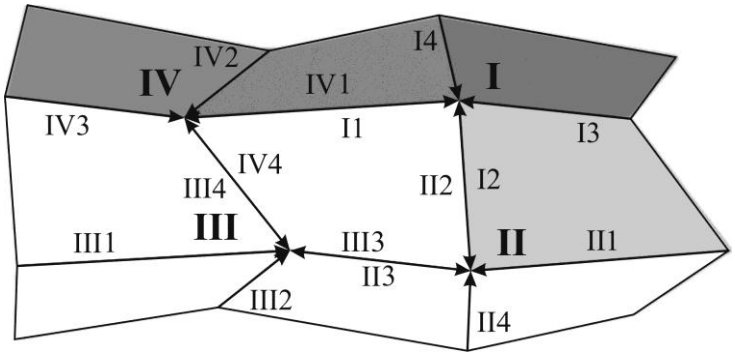

Fig. 3.11 Type ID6.

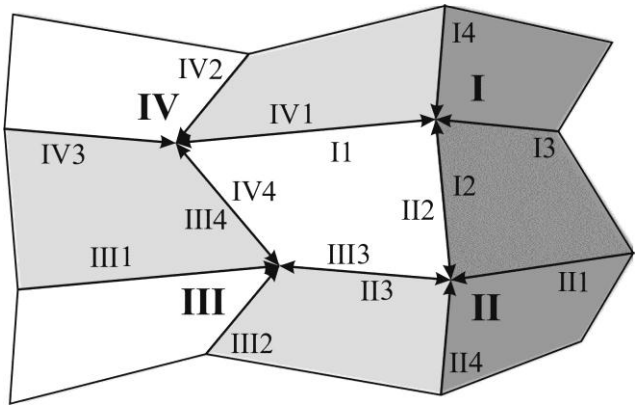

Fig. 3.12 Type ID7.

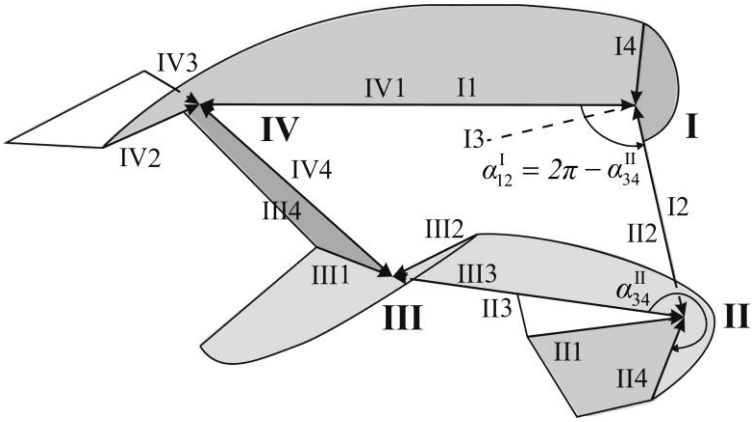

Fig. 3.13 Type ID8.

3.3.2 Group Two

Let

$$A1A2 = A3A4, \quad A'1A'2 = A'3A'4, \tag{3.29}$$

following conditions can be derived,

$$\begin{gathered}
\alpha_{12}^{\mathrm{I}} + \alpha_{23}^{\mathrm{II}} = \pi, \quad \alpha_{23}^{\mathrm{I}} + \alpha_{12}^{\mathrm{II}} = \pi, \\
\alpha_{34}^{\mathrm{III}} + \alpha_{41}^{\mathrm{IV}} = \pi, \quad \alpha_{41}^{\mathrm{III}} + \alpha_{34}^{\mathrm{IV}} = \pi, \\
\cos\alpha_{12}^{j}\cos\alpha_{34}^{j} = \cos\alpha_{23}^{j}\cos\alpha_{41}^{j}.
\end{gathered} \tag{3.30}$$

Relationships in (3.30) make axes IV3, IV1, I1 and I3 coplanar, also III1, III3, II3 and II1 coplanar, as shown in Fig. 3.14. To make the remains of Eqns. (3.17) and (3.18) equivalent, two types of assembly can be derived as listed in Table 3.2.

Table 3.2 Mobile assemblies group two

Name	Assumption	Shape of central facet
Orthogonal	$A1A2 - A3A4 = 0$, $A'1A'2 - A'3A'4 = 0$, i.e. axes IV3, IV1, I1 and I3 coplanar, also III1, III3, II3 and II1 coplanar.	Equilateral trapezoid
Miura-Ori's variation		Parallelogram

(1) The orthogonal type

The orthogonal type has following relationships,

$$\alpha_{12}^{\mathrm{I}}+\alpha_{23}^{\mathrm{II}}=\pi,\quad \alpha_{23}^{\mathrm{I}}+\alpha_{12}^{\mathrm{II}}=\pi,$$

$$\alpha_{34}^{\mathrm{III}}+\alpha_{41}^{\mathrm{IV}}=\pi,\quad \alpha_{41}^{\mathrm{III}}+\alpha_{34}^{\mathrm{IV}}=\pi,$$

$$\cos\alpha_{12}^{j}\cos\alpha_{34}^{j}=\cos\alpha_{23}^{j}\cos\alpha_{41}^{j}, \tag{3.31}$$

$$\alpha_{12}^{\mathrm{I}}=\alpha_{41}^{\mathrm{IV}},\quad \alpha_{41}^{\mathrm{I}}=\alpha_{12}^{\mathrm{IV}},$$

$$\alpha_{23}^{\mathrm{II}}=\alpha_{34}^{\mathrm{III}},\quad \alpha_{34}^{\mathrm{II}}=\alpha_{23}^{\mathrm{III}}.$$

The central facet is an equilateral trapezoid (see Fig. 3.14).

(2) Miura-Ori's variation

$$\alpha_{12}^{\mathrm{I}}+\alpha_{23}^{\mathrm{II}}=\pi,\quad \alpha_{23}^{\mathrm{I}}+\alpha_{12}^{\mathrm{II}}=\pi,$$

$$\alpha_{34}^{\mathrm{III}}+\alpha_{41}^{\mathrm{IV}}=\pi,\quad \alpha_{41}^{\mathrm{III}}+\alpha_{34}^{\mathrm{IV}}=\pi,$$

$$\cos\alpha_{12}^{j}\cos\alpha_{34}^{j}=\cos\alpha_{23}^{j}\cos\alpha_{41}^{j}, \tag{3.32}$$

$$\alpha_{12}^{\mathrm{I}}+\alpha_{41}^{\mathrm{IV}}=\pi,\quad \alpha_{41}^{\mathrm{I}}+\alpha_{12}^{\mathrm{IV}}=\pi,$$

$$\alpha_{23}^{\mathrm{II}}+\alpha_{34}^{\mathrm{III}}=\pi,\quad \alpha_{34}^{\mathrm{II}}+\alpha_{23}^{\mathrm{III}}=\pi.$$

In this assembly, the central facet is a parallelogram (see Fig. 3.15). Due to the parallelogram panels and coplanar feature presented in Eqns. (3.32), this type can be considered as Miura-Ori's variations.

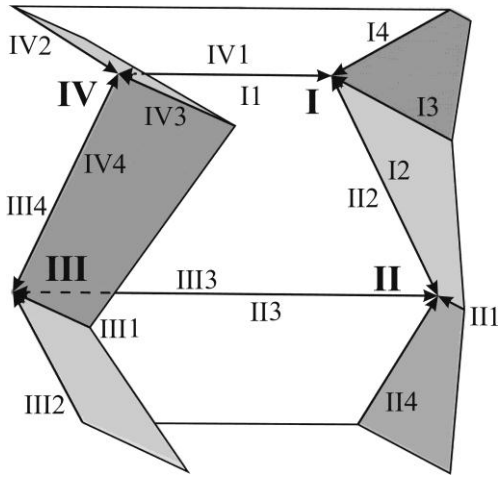

Fig. 3.14 Orthogonal type

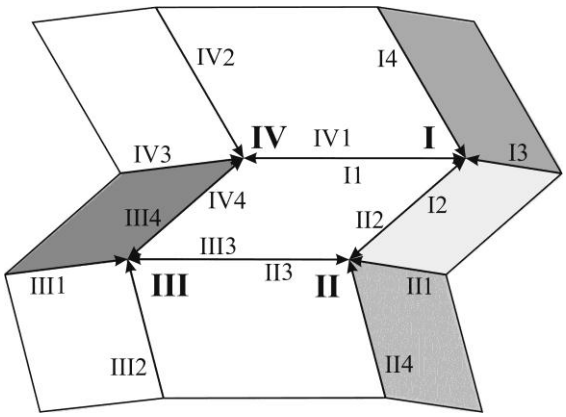

Fig. 3.15 Miura-Ori's variation

3.3.3 Group three

Let

$$A1 = A3,\ A2 = A4, \quad A'1 = A'3,\ A'2 = A'4, \tag{3.33}$$

and given different relationships of θ_1^{I} and θ_3^{II}, 4 types of assemblies can be derived from (3.17) and (3.18) as listed in Table 3.3.

Table 3.3 Mobile assemblies group three

Name	Assumption	Relationships of θ_1^{I} and θ_3^{II}	Shape of central facet
Planar-symmetric	$A1=A3, A2=A4$ $A'1=A'3, A'2=A'4$	$\theta_1^{\mathrm{I}}=\theta_3^{\mathrm{II}}$	Equilateral trapezoid
Rotational symmetric			
Translational		$\theta_1^{\mathrm{I}}+\theta_3^{\mathrm{II}}=\pi$	Trapezoid or parallelogram
Reverse supplementary		$\theta_1^{\mathrm{I}}+\theta_3^{\mathrm{II}}=2\pi$	

(1) The planar-symmetric type

The relationships of the planar-symmetric type are

$$\begin{aligned}
&\alpha_{12}^{\mathrm{I}}=\alpha_{23}^{\mathrm{II}}, \quad \alpha_{12}^{\mathrm{III}}=\alpha_{23}^{\mathrm{IV}},\\
&\alpha_{23}^{\mathrm{I}}=\alpha_{12}^{\mathrm{II}}, \quad \alpha_{23}^{\mathrm{III}}=\alpha_{12}^{\mathrm{IV}},\\
&\alpha_{34}^{\mathrm{I}}=\alpha_{41}^{\mathrm{II}}, \quad \alpha_{34}^{\mathrm{III}}=\alpha_{41}^{\mathrm{IV}},\\
&\alpha_{41}^{\mathrm{I}}=\alpha_{34}^{\mathrm{II}}, \quad \alpha_{41}^{\mathrm{III}}=\alpha_{34}^{\mathrm{IV}}.
\end{aligned} \tag{3.34}$$

The central facet is an equilateral trapezoid as shown in Fig. 3.16. The relationships in (3.34) make linkages I and III the mirror images of linkages II and IV, respectively. This type is named the planar-symmetric type in (Stachel 2010).

(2) Rotational symmetric type

The relationships of the rotational symmetric type are

$$\begin{aligned}
&\alpha_{12}^{\mathrm{I}} = \alpha_{23}^{\mathrm{II}}, \quad \alpha_{12}^{\mathrm{III}} = \alpha_{23}^{\mathrm{IV}}, \\
&\alpha_{23}^{\mathrm{I}} = \alpha_{12}^{\mathrm{II}} + \pi, \quad \alpha_{23}^{\mathrm{III}} = \alpha_{12}^{\mathrm{IV}} - \pi, \\
&\alpha_{34}^{\mathrm{I}} = \alpha_{41}^{\mathrm{II}}, \quad \alpha_{34}^{\mathrm{III}} = \alpha_{41}^{\mathrm{IV}}, \\
&\alpha_{41}^{\mathrm{I}} = \alpha_{34}^{\mathrm{II}} - \pi, \quad \alpha_{41}^{\mathrm{III}} = \alpha_{34}^{\mathrm{IV}} + \pi.
\end{aligned} \tag{3.35}$$

Angle $\alpha_{41}^{\mathrm{III}} = \alpha_{34}^{\mathrm{IV}} + \pi$ is shown in Fig. 3.17. In this type, every linkage has one reversed axis compared to the planar-symmetric type. Relationships in (3.35) show the central facet is also an equilateral trapezoid.

(3) The translational type

The translational type has following relationships.

$$\begin{aligned}
&\alpha_{12}^{\mathrm{I}} + \alpha_{23}^{\mathrm{II}} = \pi, \quad \alpha_{12}^{\mathrm{III}} = \alpha_{23}^{\mathrm{IV}}, \\
&\alpha_{23}^{\mathrm{I}} + \alpha_{12}^{\mathrm{II}} = \pi, \quad \alpha_{23}^{\mathrm{III}} = \alpha_{12}^{\mathrm{IV}}, \\
&\alpha_{34}^{\mathrm{I}} = \alpha_{41}^{\mathrm{II}}, \quad \alpha_{34}^{\mathrm{III}} + \alpha_{41}^{\mathrm{IV}} = \pi, \\
&\alpha_{41}^{\mathrm{I}} = \alpha_{34}^{\mathrm{II}}, \quad \alpha_{41}^{\mathrm{III}} + \alpha_{34}^{\mathrm{IV}} = \pi.
\end{aligned} \tag{3.36}$$

In this case, the central facet can be a trapezoid or a parallelogram, as shown in Fig. 3.18. Due to $\alpha_{34}^{\mathrm{I}} = \alpha_{41}^{\mathrm{II}}$, $\alpha_{41}^{\mathrm{I}} = \alpha_{34}^{\mathrm{II}}$, $\alpha_{12}^{\mathrm{III}} = \alpha_{23}^{\mathrm{IV}}$ and $\alpha_{23}^{\mathrm{III}} = \alpha_{12}^{\mathrm{IV}}$, three panels of linkages I and IV seems like being translated to the corresponding three panels

of linkages II and III, respectively. This type is first introduced in (Stachel 2010).

(4) The reverse supplementary type

The reverse supplementary type has following relationships.

$$\begin{gathered}\alpha_{12}^{\mathrm{I}}+\alpha_{23}^{\mathrm{II}}=\pi, \quad \alpha_{12}^{\mathrm{III}}=\alpha_{23}^{\mathrm{IV}}, \\ \alpha_{23}^{\mathrm{I}}+\alpha_{12}^{\mathrm{II}}=2\pi, \quad \alpha_{23}^{\mathrm{III}}+\alpha_{12}^{\mathrm{IV}}=\pi, \\ \alpha_{34}^{\mathrm{I}}=\alpha_{41}^{\mathrm{II}}, \quad \alpha_{34}^{\mathrm{III}}+\alpha_{41}^{\mathrm{IV}}=\pi, \\ \alpha_{41}^{\mathrm{I}}+\alpha_{34}^{\mathrm{II}}=\pi, \quad \alpha_{41}^{\mathrm{III}}+\alpha_{34}^{\mathrm{IV}}=2\pi.\end{gathered} \tag{3.37}$$

According to (3.37), the central facet can be a trapezoid or a parallelogram as shown in Fig. 3.19.

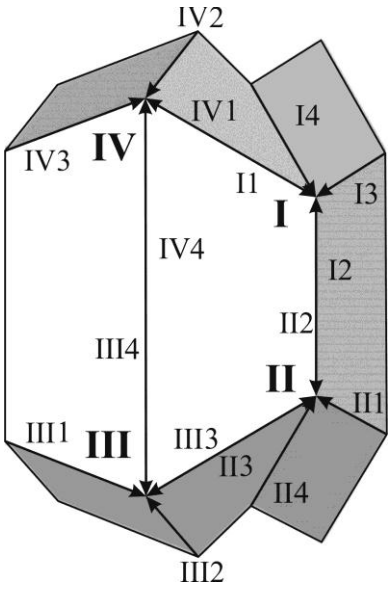

Fig. 3.16 Planar-symmetric type.

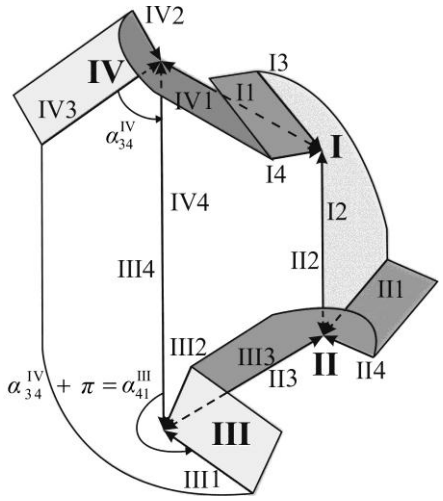

Fig. 3.17 Rotational symmetric type.

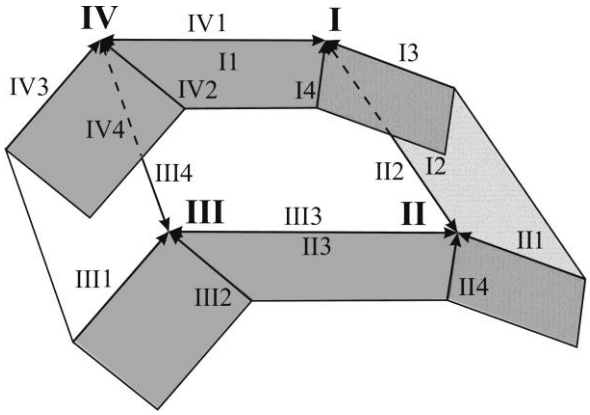

Fig. 3.18 Translational type.

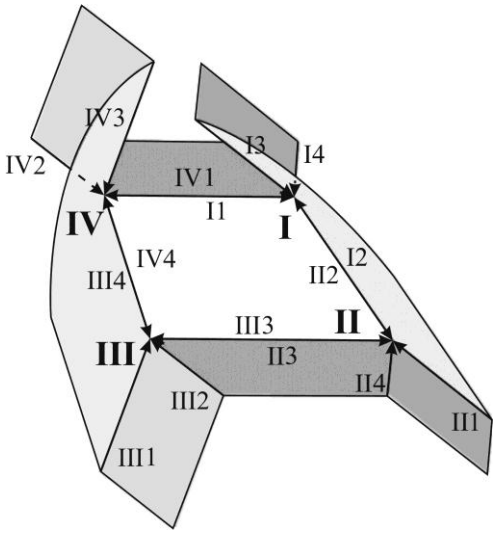

Fig. 3.19 Reverse supplementary type.

3.3.4 Group four

Let

$$A1=-A3,\ A2=-A4,\quad A'1=-A'3,\ A'2=-A'4, \tag{3.38}$$

three types of assemblies are derived and listed in Table 3.4.

Table 3.4 Mobile assemblies group four

Name	Assumption	Relationships of θ_1^{I} and θ_3^{II}	Shape of central facet
Supplementary	$A1=-A3, A2=-A4$ $A'1=-A'3, A'2=-A'4$	$\theta_1^{\mathrm{I}}+\theta_3^{\mathrm{II}}=2\pi$	Trapezoid or parallelogram
Reverse translational		$\theta_1^{\mathrm{I}}+\theta_3^{\mathrm{II}}=\pi$	
Reverse symmetric		$\theta_1^{\mathrm{I}}-\theta_3^{\mathrm{II}}=\pi$	Equilateral trapezoid

(1) The supplementary type

The supplementary type is represented as following.

$$\begin{aligned}
&\alpha_{12}^{\mathrm{I}}+\alpha_{23}^{\mathrm{II}}=\pi,\quad \alpha_{12}^{\mathrm{III}}+\alpha_{23}^{\mathrm{IV}}=\pi,\\
&\alpha_{23}^{\mathrm{I}}+\alpha_{12}^{\mathrm{II}}=\pi,\quad \alpha_{23}^{\mathrm{III}}+\alpha_{12}^{\mathrm{IV}}=\pi,\\
&\alpha_{34}^{\mathrm{I}}+\alpha_{41}^{\mathrm{II}}=\pi,\quad \alpha_{34}^{\mathrm{III}}+\alpha_{41}^{\mathrm{IV}}=\pi,\\
&\alpha_{41}^{\mathrm{I}}+\alpha_{34}^{\mathrm{II}}=\pi,\quad \alpha_{41}^{\mathrm{III}}+\alpha_{34}^{\mathrm{IV}}=\pi.
\end{aligned} \tag{3.39}$$

According to the relationships in Eqns. (3.39), the corresponding angles from two linkages are supplementary. The central facet can be a trapezoid or a parallelogram, see Fig. 3.20. The supplementary type is a novel type.

The isogonal type was introduced in (Stachel 2010). However, the condition that opposite angles of each linkage are equal is not sufficient to build the assembly with planar quadrilaterals. The isogonal type is included in the supplementary type with additional conditions

$$\alpha_{12}^{j}=\alpha_{34}^{j},\alpha_{23}^{j}=\alpha_{41}^{j}. \tag{3.40}$$

The isogonal type is shown in Fig. 3.21.

(2) The reverse translational type

The reverse translational type is represented by the relationships as follows.

$$\begin{aligned}
&\alpha_{12}^{\mathrm{I}}+\alpha_{23}^{\mathrm{II}}=\pi, \quad \alpha_{12}^{\mathrm{III}}+\alpha_{23}^{\mathrm{IV}}=\pi,\\
&\alpha_{23}^{\mathrm{I}}+\alpha_{12}^{\mathrm{II}}=\pi, \quad \alpha_{23}^{\mathrm{III}}-\alpha_{12}^{\mathrm{IV}}=\pi,\\
&\alpha_{34}^{\mathrm{I}}+\alpha_{41}^{\mathrm{II}}=\pi, \quad \alpha_{34}^{\mathrm{III}}+\alpha_{41}^{\mathrm{IV}}=\pi,\\
&\alpha_{41}^{\mathrm{I}}-\alpha_{34}^{\mathrm{II}}=-\pi, \quad \alpha_{41}^{\mathrm{III}}+\alpha_{34}^{\mathrm{IV}}=\pi.
\end{aligned} \tag{3.41}$$

The central facet is also a trapezoid or a parallelogram as shown in Fig. 3.22. This type is also novel.

(3) The reverse symmetric type

The relationships of the reverse symmetric type are list below.

$$\begin{aligned}
&\alpha_{12}^{\mathrm{I}}=\alpha_{23}^{\mathrm{II}},\quad \alpha_{12}^{\mathrm{III}}+\alpha_{23}^{\mathrm{IV}}=\pi,\\
&\alpha_{23}^{\mathrm{I}}=\alpha_{12}^{\mathrm{II}},\quad \alpha_{23}^{\mathrm{III}}+\alpha_{12}^{\mathrm{IV}}=\pi,\\
&\alpha_{34}^{\mathrm{I}}+\alpha_{41}^{\mathrm{II}}=\pi,\quad \alpha_{34}^{\mathrm{III}}=\alpha_{41}^{\mathrm{IV}},\\
&\alpha_{41}^{\mathrm{I}}+\alpha_{34}^{\mathrm{II}}=\pi,\quad \alpha_{41}^{\mathrm{III}}=\alpha_{34}^{\mathrm{IV}}.
\end{aligned} \tag{3.42}$$

The central facet is an equilateral trapezoid, as shown in Fig. 3.23. In the reverse symmetric type, the axes IV2 and I4 of this type are on the opposite directions of the corresponding axes in the planar-symmetric type. This type is also first introduced.

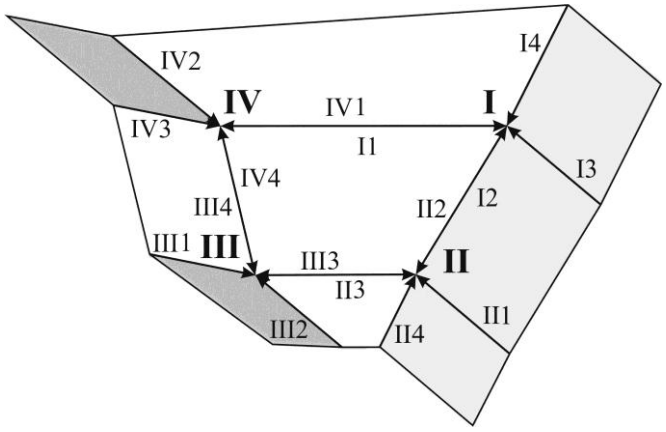

Fig. 3.20 Supplementary type

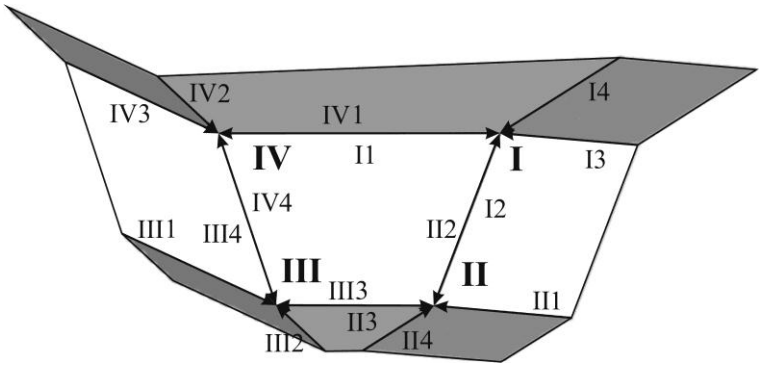

Fig. 3.21 Isogonal type

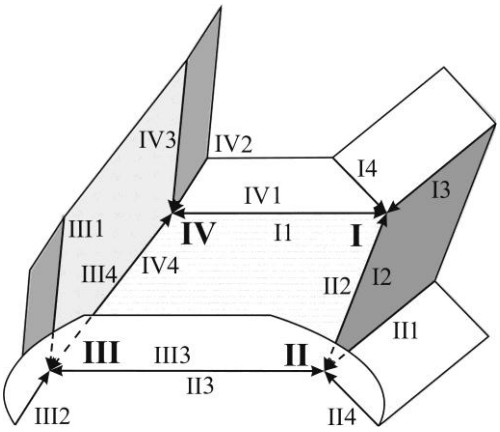

Fig. 3.22 Reverse translational type

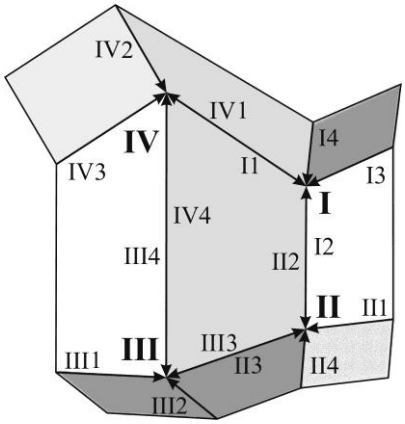

Fig. 3.23 Reverse symmetric type

3.4 Discussions

In the previous section, 17 distinctive types of mobile assemblies are obtained with explicit geometric relationships (listed in Table B.1), based on which 11 hybrid assemblies can be constructed. Assemblies which are first introduced here are marked in Table B.3. Networks with an unlimited number of spherical 4*R* linkages and rigid origami pattern for flat surface are also discussed as follows.

3.4.1 Hybrid Assemblies

The compatibility condition in Eqn. (3.16) can be satisfied as long as the output angles θ_3^{II} and θ_3^{III}, through chains I-II and IV-III respectively, are equal. Thus,

two mobile assemblies sharing the same relationship between θ_1^{I} and θ_3^{II} can be combined to form a hybrid assembly.

As listed in Table B.1, the types ID3, ID4, ID5, ID6, planar-symmetric and rotational symmetric share relationship $\theta_1^{\mathrm{I}}=\theta_3^{\mathrm{II}}$, and five distinctive hybrid assemblies can be derived from their combinations. The hybrid assemblies are listed in Table B.2. For example, the hybrid assembly of planar-symmetric and rotational symmetric type is shown in Fig. 3.24 a), which has the following relationships,

$$\begin{aligned}
&\alpha_{12}^{\mathrm{I}}=\alpha_{23}^{\mathrm{II}},\quad \alpha_{12}^{\mathrm{III}}=\alpha_{23}^{\mathrm{IV}},\\
&\alpha_{23}^{\mathrm{I}}=\alpha_{12}^{\mathrm{II}},\quad \alpha_{23}^{\mathrm{III}}=\alpha_{12}^{\mathrm{IV}}-\pi,\\
&\alpha_{34}^{\mathrm{I}}=\alpha_{41}^{\mathrm{II}},\quad \alpha_{34}^{\mathrm{III}}=\alpha_{41}^{\mathrm{IV}},\\
&\alpha_{41}^{\mathrm{I}}=\alpha_{34}^{\mathrm{II}},\quad \alpha_{41}^{\mathrm{III}}=\alpha_{34}^{\mathrm{IV}}+\pi.
\end{aligned} \tag{3.43}$$

Assemblies of the types ID7, translational and reverse translational share the relationship $\theta_1^{\mathrm{I}}+\theta_3^{\mathrm{II}}=\pi$, which form three distinctive hybrid assemblies. The example hybrid assembly of the translational and reverse translational type is shown in Fig. 3.24 b), which is designed as follows,

$$\begin{aligned}
&\alpha_{12}^{\mathrm{I}}+\alpha_{23}^{\mathrm{II}}=\pi,\quad \alpha_{12}^{\mathrm{III}}+\alpha_{23}^{\mathrm{IV}}=\pi,\\
&\alpha_{23}^{\mathrm{I}}+\alpha_{12}^{\mathrm{II}}=\pi,\quad \alpha_{23}^{\mathrm{III}}-\alpha_{12}^{\mathrm{IV}}=\pi,\\
&\alpha_{34}^{\mathrm{I}}=\alpha_{41}^{\mathrm{II}},\quad \alpha_{34}^{\mathrm{III}}+\alpha_{41}^{\mathrm{IV}}=\pi,\\
&\alpha_{41}^{\mathrm{I}}=\alpha_{34}^{\mathrm{II}},\quad \alpha_{41}^{\mathrm{III}}+\alpha_{34}^{\mathrm{IV}}=\pi.
\end{aligned} \tag{3.44}$$

Assemblies of the types ID8, supplementary and reverse supplementary share the relationship $\theta_1^{\mathrm{I}} + \theta_3^{\mathrm{II}} = 2\pi$, from which three distinctive hybrid assemble are obtained. For instance, the hybrid assembly of the reversed supplementary and supplementary type is shown in Fig. 3.24 c), which has relationships as follows,

$$\begin{gathered}
\alpha_{12}^{\mathrm{I}} + \alpha_{23}^{\mathrm{II}} = \pi, \quad \alpha_{12}^{\mathrm{III}} + \alpha_{23}^{\mathrm{IV}} = \pi, \\
\alpha_{23}^{\mathrm{I}} + \alpha_{12}^{\mathrm{II}} = 2\pi, \quad \alpha_{23}^{\mathrm{III}} + \alpha_{12}^{\mathrm{IV}} = \pi, \\
\alpha_{34}^{\mathrm{I}} = \alpha_{41}^{\mathrm{II}}, \quad \alpha_{34}^{\mathrm{III}} + \alpha_{41}^{\mathrm{IV}} = \pi, \\
\alpha_{41}^{\mathrm{I}} + \alpha_{34}^{\mathrm{II}} = \pi, \quad \alpha_{41}^{\mathrm{III}} + \alpha_{34}^{\mathrm{IV}} = \pi.
\end{gathered} \tag{3.45}$$

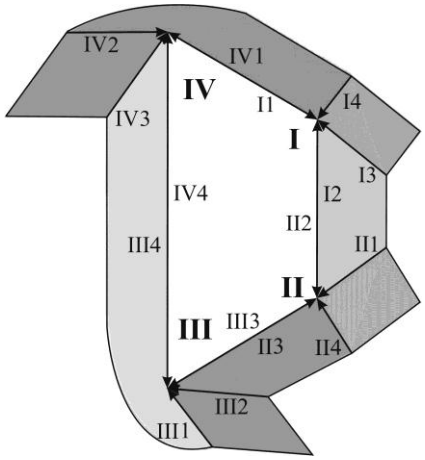

a)

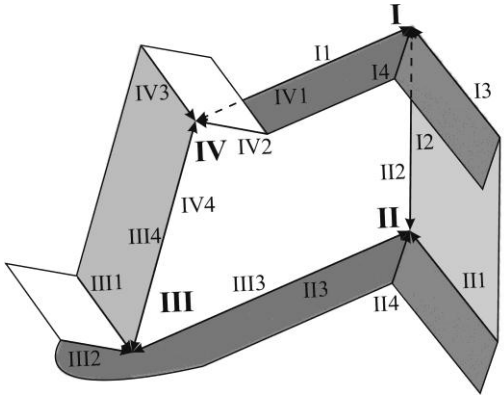

b)

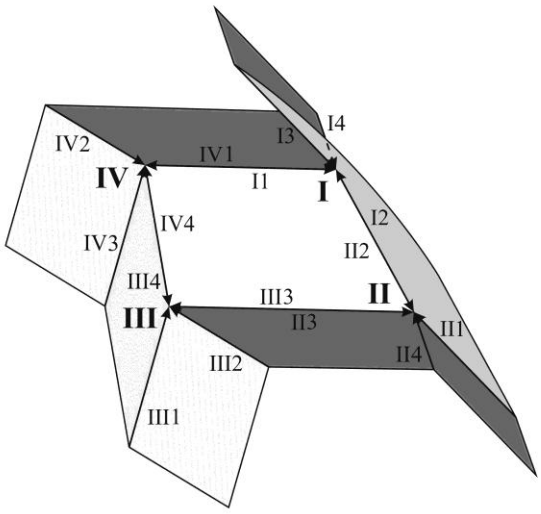

c)

Fig. 3.24 Hybrid assemblies generated from a) planar-symmetric and rotational symmetric type, b) translational and reverse translational type, c) reversed supplementary and supplementary type.

3.4.2 Networks

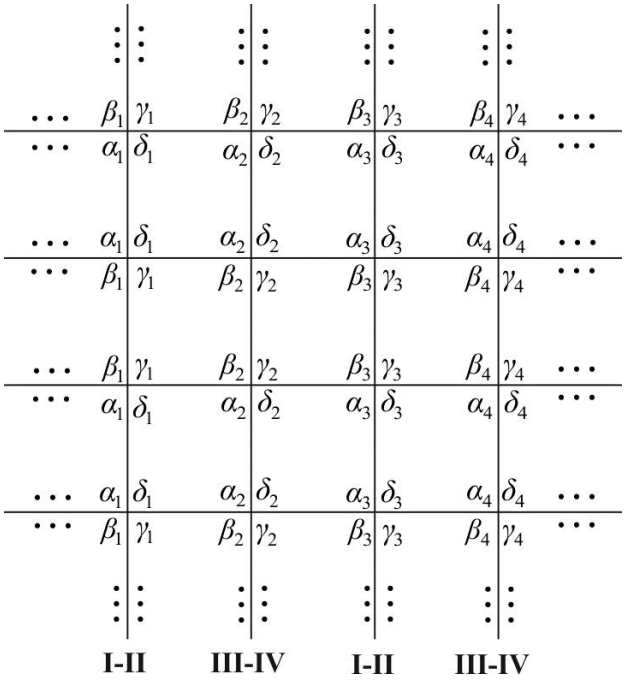

Fig. 3.25 The construction of the network of planar-symmetric assembly.

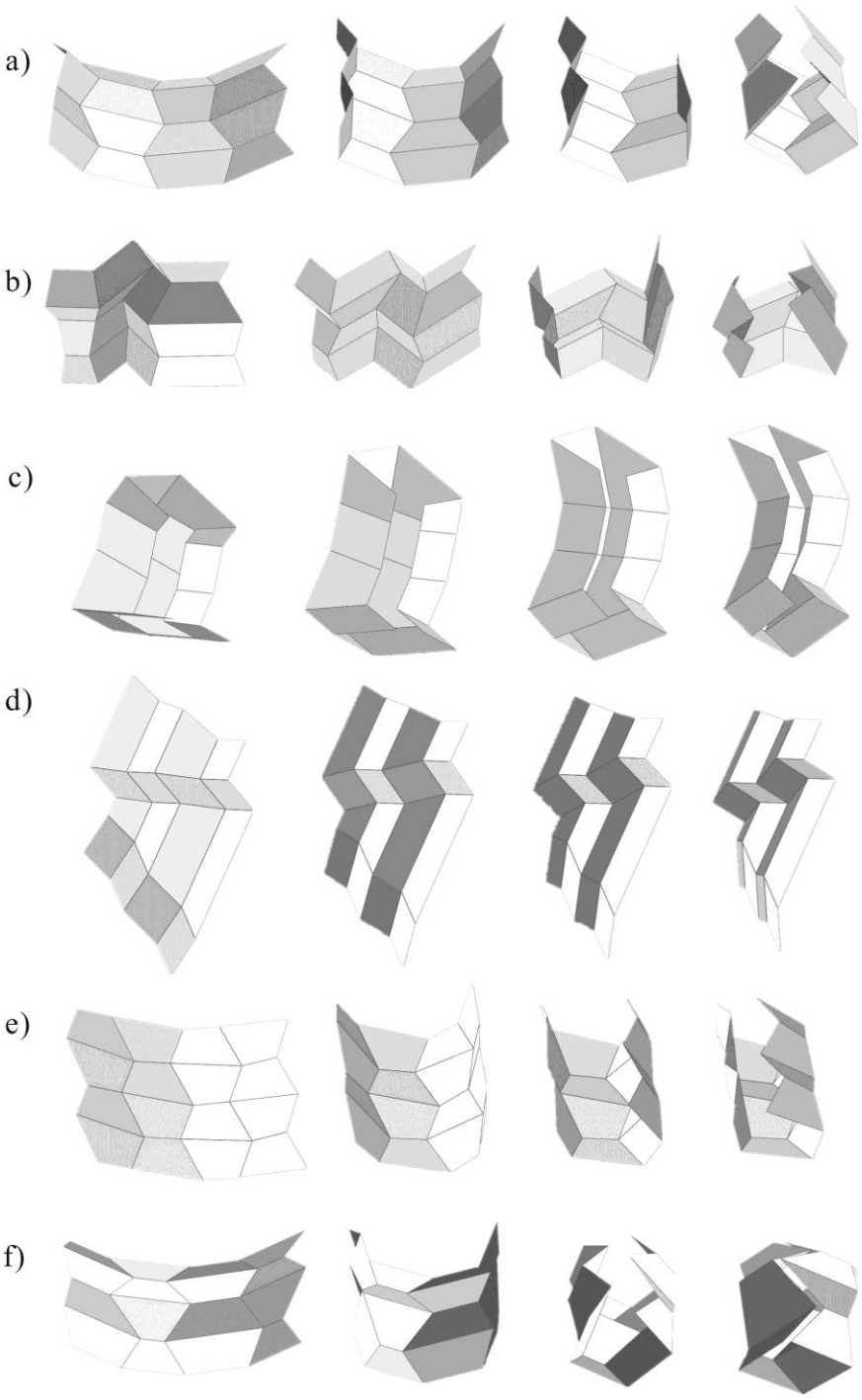

Fig. 3.26 The examples of the networks: a) planar-symmetric type; b) reverse symmetric type; c) translational type; d) supplementary type; e) identical linkage type; f) orthogonal type.

The assemblies can be extended to networks consisting of an unlimited number of linkages. A network can be constructed by connecting chains of linkages with the same θ_1^{I} and θ_3^{II} relationship. Thus, various combinations of different types, including the hybrid assemblies, are feasible. One of the simplest ways of constructing a network is to repeatedly connect chains I-II and III-IV. As shown in Fig. 3.25, chains I-II and III-IV of the planar-symmetric type are used to construct the network.

Due to the 2π limitation of a planar quadrilateral, the rotational symmetric, reverse translational, reverse supplementary types and the 8 hybrid assemblies can't be used in constructing networks. The types that can be used to construct networks are listed in Table B.3. The examples of networks are shown in Fig. 3.26.

3.4.3 Rigid origami patterns for flat surface

Given the flat surface condition at every vertices

$$\sum_{i=1}^{4} \alpha_{i(i+1)}^{j} = 2\pi, \tag{3.46}$$

the networks can be fold from a flat rigid piece of paper, which are considered as rigid origami patterns. The types that can generate rigid origami patterns are given in Table B.3. The examples are shown in Fig. 3.27.

3.5 Summary

In this chapter, a kinematic model of the mobile assemblies has been proposed based on the closed adjacent assembly of four spherical 4*R* linkages. To obtain assemblies of one degree of freedom, the kinematic compatibility conditions have been studied systematically. 17 types of mobile assemblies were obtained by solving the compatibility conditions. The solutions include the existing one-DOF mobile assemblies, as well as 12 novel ones (see Table B.3). Based on the

solutions, the relationships of kinematic variables were discovered, which inspired 11 types of hybrid assemblies; the hybrid assemblies are also newly introduced. 16 types of networks have been derived, which can be constructed by an unlimited number of linkages. Given the flat surface condition, 14 types of rigid origami patterns for flat surfaces have been obtained.

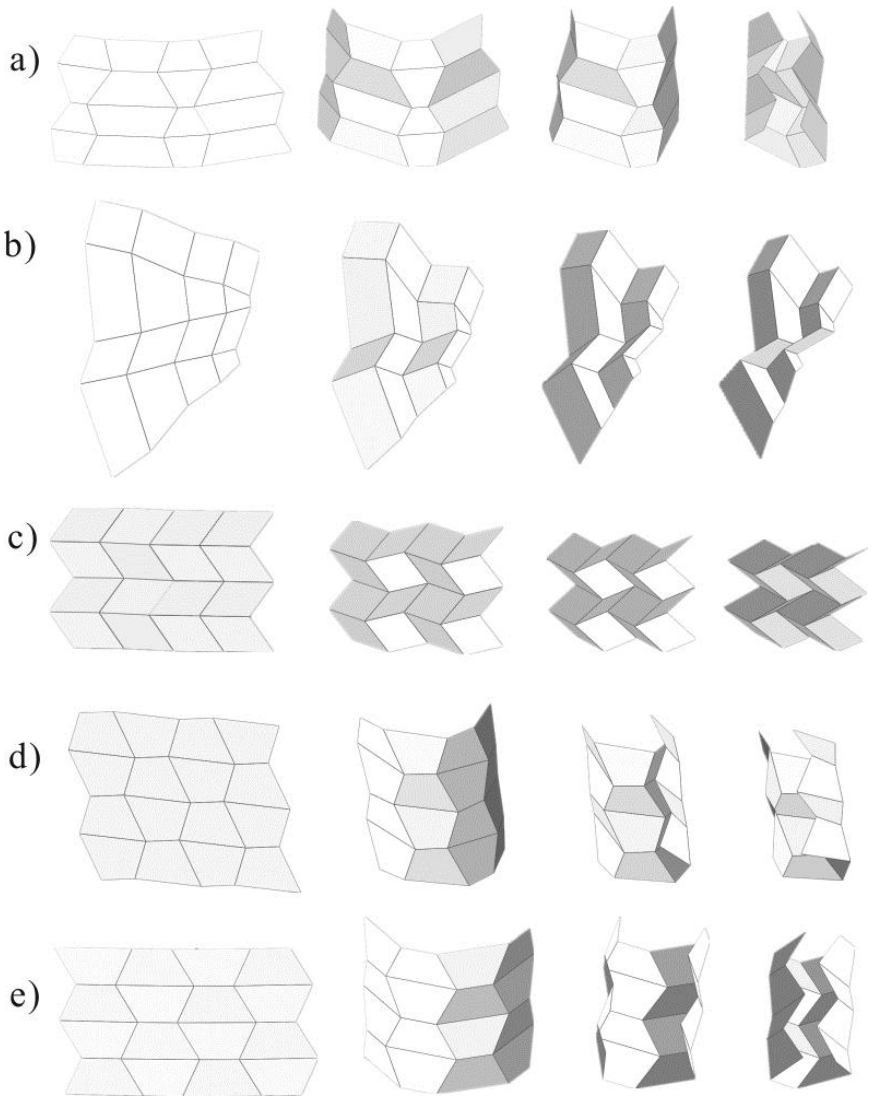

Fig. 3.27 The rigid origami patterns for flat surface: a) the planar-symmetric type; b) the supplementary type; c) the Miura-ori; d) the identical linkage type; e) the orthogonal type.

Chapter 4

Deployable Prismatic Structures with Rigid Origami Patterns

4.1 Introduction

The focus of this chapter is on the general conditions of a rigid origami pattern that can be used for deployable prismatic structures. A kinematic model is proposed based on the closed opposite assemblies of spherical 4*R* linkages. The compatibility conditions of these mobile assemblies are then derived. Two groups of even-sided deployable prismatic structures are obtained, which satisfy the general conditions. For the 4-sided case, one structure incorporates a kite-shaped intersection, whereas the other incorporates a parallelogram. Unit variations are discussed. Straight and curvy multi-layer prisms are obtained by changing the dihedral angles between the intersecting planes. A general method to design even-sided multi-layer deployable prismatic structures is proposed using the geometric conditions of the origami patterns. All the deployable structures constructed using this method can be deployed and folded along the central axis of the prisms with a single degree of freedom, which makes them attractive for a wide range of engineering applications.

The layout of the chapter is as follows. In section 4.2, the kinematics of the spherical 4*R* linkage is introduced. The geometric and kinematic compatibility conditions for the closed opposite assembly of spherical 4*R* linkages are derived. In section 4.3, rigid origami patterns for two groups of 2*n*-sided prismatic structures are obtained. In section 4.4, straight and curvy multi-layer structures are discussed; the general design method for multi-layer deployable prismatic structures is presented. Finally, summary in section 4.5 ends this chapter.

4.2 **Compatibility condition for the opposite assembly of spherical 4*R* linkages**

Without a loss of generality, two linkages are connected by aligning axes Z_1^j and Z_3^{j+1}, which is called the *opposite assembly*, as shown in Fig. 4.1. The planes $\mathrm{Z}_1^j \times \mathrm{Z}_2^j$ and $\mathrm{Z}_2^{j+1} \times \mathrm{Z}_3^{j+1}$ coincide as do planes $\mathrm{Z}_4^j \times \mathrm{Z}_1^j$ and $\mathrm{Z}_3^{j+1} \times \mathrm{Z}_4^{j+1}$, i.e., the normal vectors $\mathrm{X}_2^j // \mathrm{X}_3^{j+1}$ and $\mathrm{X}_1^j // \mathrm{X}_4^{j+1}$. Therefore, the rotation angles θ_1^j and θ_3^{j+1} are always equal during the movement of the assembly,

$$\theta_1^j = \theta_3^{j+1} \tag{4.1}$$

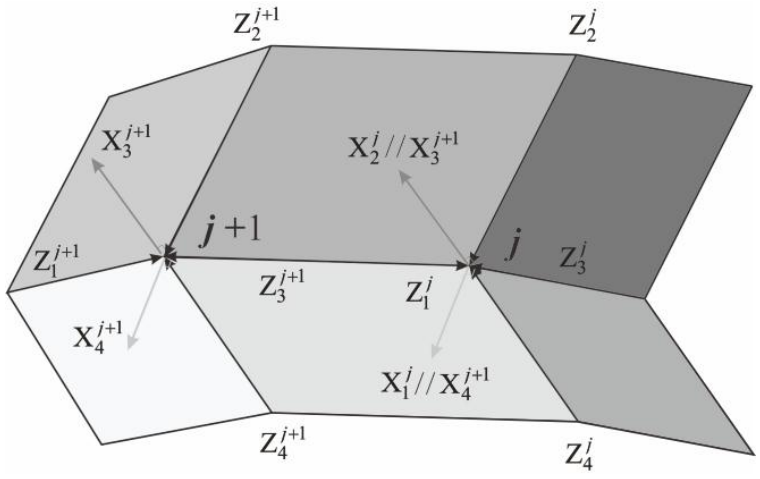

Fig. 4.1 Assembly of two spherical 4*R* linkages *j* and *j* + 1.

To form deployable prismatic structures, *N* spherical 4*R* linkages are assembled into a closed chain, as shown in Fig. 4.2. In each linkage, the rotation angle θ_1^j can be considered an input, whereas θ_3^j becomes the output, or vice versa. This assembly can be considered as an open chain closed by connecting linkage I and linkage *N*, which requires $\theta_1^N = \theta_3^{\mathrm{I}}$. Due to Eqns. (3.10) and (4.1), the kinematic compatibility condition,

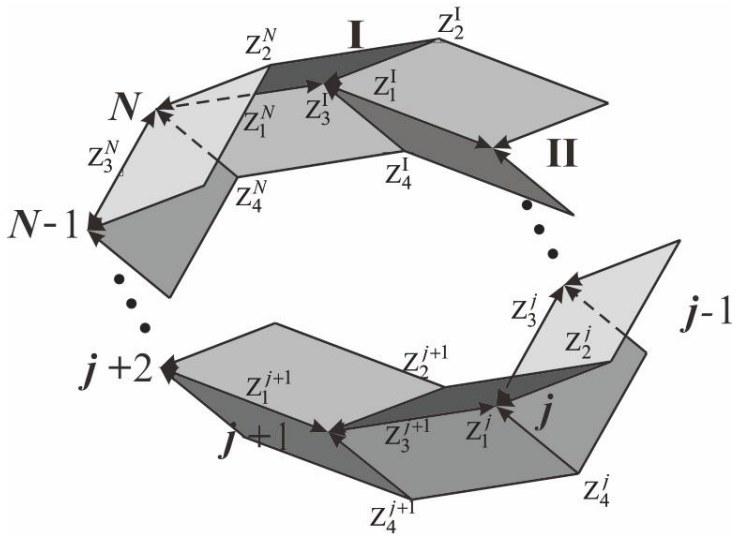

Fig. 4.2 Closed assembly of N spherical 4R linkages.

$$
\begin{aligned}
&\cos\theta_1^N = \cos\theta_3^{\mathrm{I}} = f^{\mathrm{I}}(\cos\theta_1^{\mathrm{I}}),\\
&\cos\theta_1^{\mathrm{I}} = \cos\theta_3^{\mathrm{II}} = f^{\mathrm{II}}(\cos\theta_1^{\mathrm{II}}),\\
&\vdots\\
&\cos\theta_1^{N\text{-}2} = \cos\theta_3^{N\text{-}1} = f^{N\text{-}1}(\cos\theta_1^{N\text{-}1}),\\
&\cos\theta_1^{N\text{-}1} = \cos\theta_3^{N} = f^{N}(\cos\theta_1^{N}),\\
&\Rightarrow\\
&\cos\theta_1^N = f^{\mathrm{I}}(f^{\mathrm{II}}(\cdots f^{N-1}(f^N(\cos\theta_1^N))\cdots)),
\end{aligned}
\tag{4.2}
$$

must be satisfied. Considering Eqn. (3.10), Eqn. (4.2) can be represented as

$$
\cos\theta_1^{\mathrm{I}} = A^{\mathrm{I}} + B^{\mathrm{I}}A^{\mathrm{II}} + \cdots + B^{\mathrm{I}}B^{\mathrm{II}}\cdots B^{N-1}A^N + B^{\mathrm{I}}B^{\mathrm{II}}\cdots B^N\cos\theta_1^{\mathrm{I}}, \tag{4.3}
$$

in which

$$
A^j = \frac{\mathrm{c}\alpha_{41}^j\,\mathrm{c}\alpha_{12}^j - \mathrm{c}\alpha_{34}^j\,\mathrm{c}\alpha_{23}^j}{\mathrm{s}\alpha_{41}^j\,\mathrm{s}\alpha_{12}^j},\quad B^j = \frac{\mathrm{s}\alpha_{34}^j\,\mathrm{s}\alpha_{23}^j}{\mathrm{s}\alpha_{41}^j\,\mathrm{s}\alpha_{12}^j}.
$$

Equation (4.3) is always true when $A^{\mathrm{I}} + B^{\mathrm{I}}A^{\mathrm{II}} + \cdots + B^{\mathrm{I}}B^{\mathrm{II}}\cdots B^{N-1}A^N = 0$ and $B^{\mathrm{I}}B^{\mathrm{II}}\cdots B^N = 1$, which leads to

$$\alpha_{12}^{j}+\alpha_{23}^{j+1}=\pi,\ \alpha_{41}^{j}+\alpha_{34}^{j+1}=\pi. \tag{4.4}$$

Thus, the axes in Fig. 4.2 must be

$$\mathrm{Z}_2^{j} \perp \mathrm{Z}_2^{j+1},\ \mathrm{Z}_4^{j} \perp \mathrm{Z}_4^{j+1}. \tag{4.5}$$

Therefore, all the Z_2^{j}s and planes between the adjacent axes form a prism as do the Z_4^{j}s. Also, the polygon that connects the vertices of all the linkages with axes Z_1^{j} and Z_3^{j} can be considered as the intersection of two prisms, which divides the closed assembly into upper and lower halves. Therefore, the polylines formed by axes Z_2^{j} and Z_4^{j} are called the *ridgelines* of the prismatic structures.

In both halves, two closed circles are established. Therefore, the following two geometric compatibility conditions should be satisfied:

$$\begin{aligned}
&\mathbf{T}_{\mathbf{U}}^{\mathrm{I}(N)}\cdots\mathbf{T}_{\mathbf{U}}^{(j+1)j}\cdots\mathbf{T}_{\mathbf{U}}^{(\mathrm{II})\mathrm{I}}=\mathbf{I},\\
&\mathbf{T}_{\mathbf{L}}^{\mathrm{I}(\mathrm{II})}\cdots\mathbf{T}_{\mathbf{L}}^{j(j+1)}\cdots\mathbf{T}_{\mathbf{L}}^{(N)\mathrm{I}}=\mathbf{I},
\end{aligned} \tag{4.6}$$

in which

$$\mathbf{T}_{\mathbf{U}}^{(j+1)j}=\mathbf{R}_{\mathrm{x}}(\alpha_{23}^{j+1})\mathbf{R}_{\mathrm{x}}(\pi)\mathbf{T}_{\mathrm{z}}(L_{j+1}^{j})\mathbf{R}_{\mathrm{x}}(\alpha_{12}^{j})\mathbf{R}_{\mathrm{z}}(\theta_2^{j}),$$

$$\mathbf{T}_{\mathbf{L}}^{j(j+1)}=\mathbf{R}_{\mathrm{z}}(\theta_4^{j})\mathbf{R}_{\mathrm{x}}(\alpha_{41}^{j})\mathbf{R}_{\mathrm{x}}(\pi)\mathbf{T}_{\mathrm{z}}(L_{j+1}^{j})\mathbf{R}_{\mathrm{x}}(\alpha_{34}^{j+1}).$$

As shown in Fig. 4.3, the matrix $\mathbf{T}_{\mathbf{U}}^{(j+1)j}$ represents the transformation from the coordinate frame X_3^{j+1}-Z_2^{j+1} to X_3^{j}-Z_2^{j} in the upper half of the assembly.

The matrix $\mathbf{T}_{\mathbf{L}}{}^{j(j+1)}$ represents the transformation from the coordinate frame X_4^j-Z_4^j to X_4^{j+1}-Z_4^{j+1} in the lower half of the assembly.

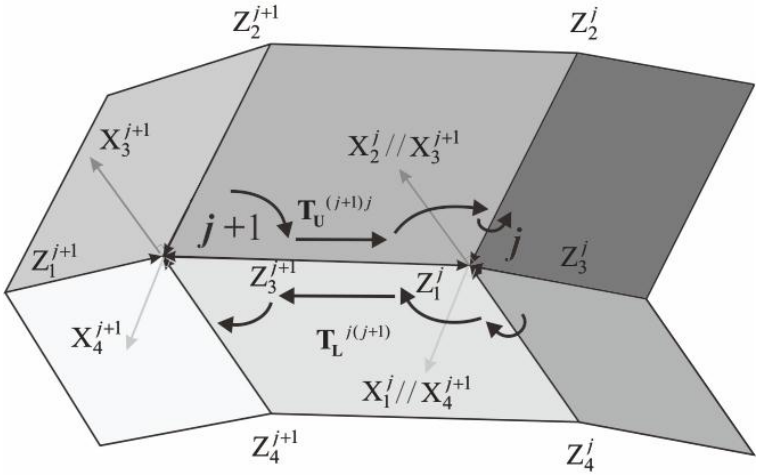

Fig. 4.3 Transformation matrices $\mathbf{T}_{\mathbf{U}}{}^{(j+1)j}$ and $\mathbf{T}_{\mathbf{L}}{}^{j(j+1)}$ in the upper and lower halves of the assembly.

The two equations in (4.6) can be rearranged as

$$\mathbf{T}_{\mathbf{U}}{}^{\mathrm{I}(N)}\mathbf{T}_{\mathbf{U}}{}^{N(N-1)}\cdots\mathbf{T}_{\mathbf{U}}{}^{(n+2)(n+1)} = [\mathbf{T}_{\mathbf{U}}{}^{(\mathrm{II})\mathrm{I}}]^{-1}[\mathbf{T}_{\mathbf{U}}{}^{(\mathrm{III})\mathrm{II}}]\cdots[\mathbf{T}_{\mathbf{U}}{}^{(n+1)n}]^{-1}, \tag{4.7}$$

$$\mathbf{T}_{\mathbf{L}}{}^{\mathrm{I}(\mathrm{II})}\mathbf{T}_{\mathbf{L}}{}^{\mathrm{II}(\mathrm{III})}\cdots\mathbf{T}_{\mathbf{L}}{}^{n(n+1)} = [\mathbf{T}_{\mathbf{L}}{}^{(N)\mathrm{I}}]^{-1}[\mathbf{T}_{\mathbf{L}}{}^{(N-1)N}]^{-1}\cdots[\mathbf{T}_{\mathbf{L}}{}^{(n+1)(n+2)}]^{-1}. \tag{4.8}$$

Eqns. (4.7) and (4.8) contains the compatibility condition of the close-chain assembly of N spherical 4R linkages. By solving the equations systematically, deployable prismatic structures with an origami pattern can be obtained. Substituting Eqn. (4.4) into Eqns. (4.7) and (4.8), and expanding the matrices, the following equations are obtained.

$$\cos\left(\sum_{j=1}^{n}\theta_4^j\right) = \cos\left(\sum_{j=n+1}^{N}\theta_4^j\right), \tag{4.9}$$

$$\cos\left(\sum_{j=1}^{n}\theta_2^j\right)=\cos\left(\sum_{j=n+1}^{N}\theta_2^j\right), \tag{4.10}$$

$$\sin\left(\sum_{j=1}^{n}\theta_4^j\right)=-\sin\left(\sum_{j=n+1}^{N}\theta_4^j\right), \tag{4.11}$$

$$\sin\left(\sum_{j=1}^{n}\theta_2^j\right)=-\sin\left(\sum_{j=n+1}^{N}\theta_2^j\right), \tag{4.12}$$

$$\sum_{k=1}^{n}\left[\sin\left(\sum_{j=1}^{k}\theta_4^j\right)\sin\left(\alpha_{41}^k\right)L_{k+1}^k\right]=\sum_{k=n+1}^{N\text{-}1}\left[\sin\left(\sum_{j=k+1}^{N}\theta_4^j\right)\sin\left(\alpha_{41}^k\right)L_{k+1}^k\right], \tag{4.13}$$

$$\sum_{k=1}^{n}\left[\sin\left(\sum_{j=\mathrm{I}}^{k}\theta_2^j\right)\sin\left(\alpha_{12}^k\right)L_{k+1}^k\right]=\sum_{k=n+1}^{N-1}\left[\sin\left(\sum_{j=k+1}^{N}\theta_2^j\right)\sin\left(\alpha_{12}^k\right)L_{k+1}^k\right], \tag{4.14}$$

$$\begin{aligned}&\sum_{k=1}^{n}\left[\cos\left(\sum_{j=1}^{k}\theta_4^j\right)\sin\left(\alpha_{41}^k\right)L_{k+1}^k\right]=\\&-\sum_{k=n+1}^{N\text{-}1}\left[\cos\left(\sum_{j=k+1}^{N}\theta_4^j\right)\sin\left(\alpha_{41}^k\right)L_{k+1}^k\right]-\sin\left(\alpha_{41}^N\right)L_1^N,\end{aligned} \tag{4.15}$$

$$\begin{aligned}&\sum_{k=1}^{n}\left[\cos\left(\sum_{j=\mathrm{I}}^{k}\theta_2^j\right)\sin\left(\alpha_{12}^k\right)L_{k+1}^k\right]=\\&-\sum_{k=n+1}^{N-1}\left[\cos\left(\sum_{j=k+1}^{N}\theta_2^j\right)\sin\left(\alpha_{12}^k\right)L_{k+1}^k\right]-\sin\left(\alpha_{12}^N\right)L_1^N,\end{aligned} \tag{4.16}$$

$$\sum_{j=1}^{n}\cos\left(\alpha_{41}^j\right)L_{j+1}^j=-\sum_{j=n+1}^{N}\cos\left(\alpha_{41}^j\right)L_{j+1}^j, \tag{4.17}$$

$$\sum_{j=1}^{n}\cos\left(\alpha_{12}^{j}\right)L_{j+1}^{j}=-\sum_{j=n+1}^{N}\cos\left(\alpha_{12}^{j}\right)L_{j+1}^{j}, \tag{4.18}$$

in which Eqns. (4.9), (4.11), (4.13), (4.15) and (4.17) are associated with the lower half, and the remaining equations are associated with the upper half.

In order to keep the intersection polygon between halves planar during the movement, adjacent planes $\mathrm{Z}_3^{j+1}\times\mathrm{Z}_1^{j+1}$ and $\mathrm{Z}_3^{j}\times\mathrm{Z}_1^{j}$ should always be coplanar. Thus, the follows should be satisfied,

$$1=\prod_{j=\mathrm{I}}^{N}\frac{C_{\mathrm{U}}^{j}-D_{\mathrm{U}}^{j}\cos\theta_2^{j}}{-D_{\mathrm{U}}^{j}+C_{\mathrm{U}}^{j}\cos\theta_2^{j}}. \tag{4.19}$$

$$1=\prod_{j=\mathrm{I}}^{N}\frac{C_{\mathrm{L}}^{j}-D_{\mathrm{L}}^{j}\cos\theta_4^{j}}{-D_{\mathrm{L}}^{j}+C_{\mathrm{L}}^{j}\cos\theta_4^{j}}, \tag{4.20}$$

in which,

$$C_{\mathrm{U}}^{j}=\sin\alpha_{12}^{j-1}\cos\alpha_{12}^{j},\ D_{\mathrm{U}}^{j}=\sin\alpha_{12}^{j}\cos\alpha_{12}^{j-1},$$

$$C_{\mathrm{L}}^{j}=\sin\alpha_{41}^{j-1}\cos\alpha_{41}^{j},\ D_{\mathrm{L}}^{j}=\sin\alpha_{41}^{j}\cos\alpha_{41}^{j-1}.$$

Eqns. (4.19) and (4.20) are obtained in Appendix C.1.

When the intersection is projected to the plane that perpendicular to the ridgelines Z_2^{j}, see Fig. 4.4, axes X_2^{j} and X_3^{j} are perpendicular to sides $j^{'}(j^{'}+1)$ and $(j^{'}-1)j^{'}$, respectively. According to the definition, the angle θ_2^{j} that rotates from X_2^{j} to X_3^{j} positively about Z_2^{j} should satisfied the following relationship

$$\theta_2^j = \pi + \angle(j^{'}-1)\,j^{'}(j^{'}+1) \tag{4.21}$$

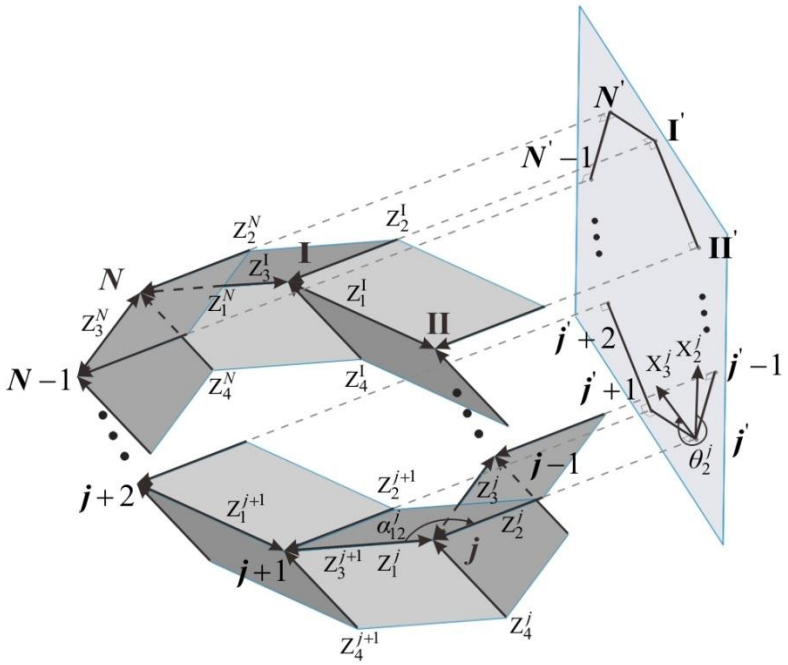

Fig. 4.4 The projection of the intersection to the plane perpendicular to ridgelines.

So the sum of the rotation angles around the ridgelines in each half is

$$\sum_{j=\mathrm{I}}^{N}\theta_2^j = \sum_{j=\mathrm{I}}^{N}\theta_4^j = N\pi + (N-2)\pi = 2(N-1)\pi, \tag{4.22}$$

for any mobile configuration because the prism remains closed. Equation (4.22) ensures Eqns. (4.9) ~ (4.12) are satisfied. Eqns. (4.13) ~ (4.16) represent the sums of corresponding lengths of the projection polygon in Fig. 4.4, which are always satisfied. Thus, the efforts should be focused on the solution of the remaining Eqns. (4.17) ~ (4.20). When $n=2$, the solution can be found through a geometric derivation (Tachi 2009b). However, for $n>2$, it is not possible to determine the solution directly. Therefore, an assumption, $N=2n$, is made with the symmetric properties to obtain several useful solutions.

4.3 Rigid origami patterns for deployable prismatic structures

4.3.1 2*n*-sided prism with a rotational symmetric intersection

By considering a rotational symmetric correspondence of the linkages in the closed chain (see Fig. 4.5), the following relationships can be obtained from (4.19) and (4.20).

$$\theta_2^j = \theta_2^{j+n}, \theta_4^j = \theta_4^{j+n}; \tag{4.23}$$

$$\alpha_{23}^j + \alpha_{23}^{j+n} = \pi, \alpha_{41}^j + \alpha_{41}^{j+n} = \pi. \tag{4.24}$$

Substituting Eqns. (4.24) into (4.17) and (4.18) derives

$$L_{j+1}^j = L_{j+n+1}^{j+n}. \tag{4.25}$$

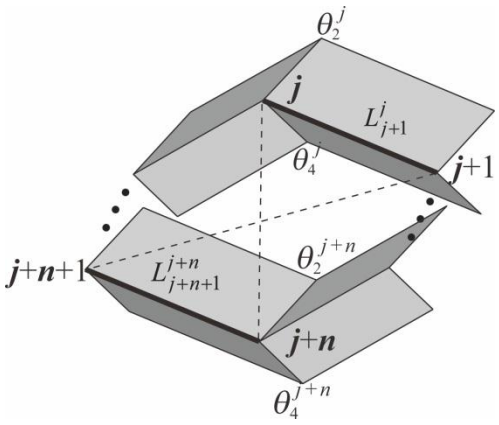

Fig. 4.5 Linkage j corresponds to $j + n$.

The relationships of the twist angles in Eqn. (4.24) constrain the intersections of the prismatic structures to planar 2*n*-sided polygons, i.e., a quadrilateral, a hexagon, an octagon, etc. Also, the corresponding angles on sides $j(j+1)$ and $(j + n)(j + n + 1)$ are supplementary. As shown in Fig. 4.6, the symmetric centers are the intersecting points of the diagonals that connect vertices j and $j + n$.

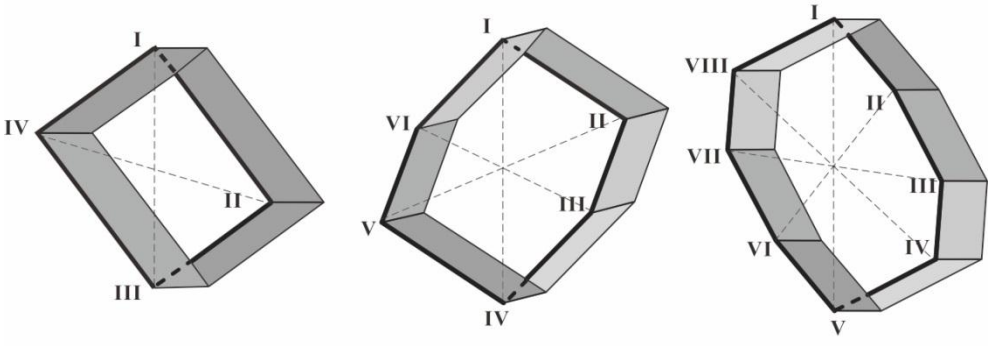

a) b) c)

Fig. 4.6 The upper-half views of the 2*n*-sided prisms with a rotational symmetric intersection: a) quadrilateral, b) hexagon, c) octagon.

It should be noted that the foldable tube proposed by Tachi (Tachi 2009b) is a special case of the structure with a rotational symmetric intersection, which requires that the tube be symmetric about the intersecting plane between the two halves to achieve a compact fold. According to Eqns. (4.23) and (4.24), in our solution, the upper and lower halves can have different θ's and α's. A 4-sided foldable tube with a parallelogram intersection is built by mating 8 rigid quadrilateral panels with revolute joints, as shown in Fig. 4.7. The folding process of this 4-sided prismatic structure is shown in Fig. 4.8.

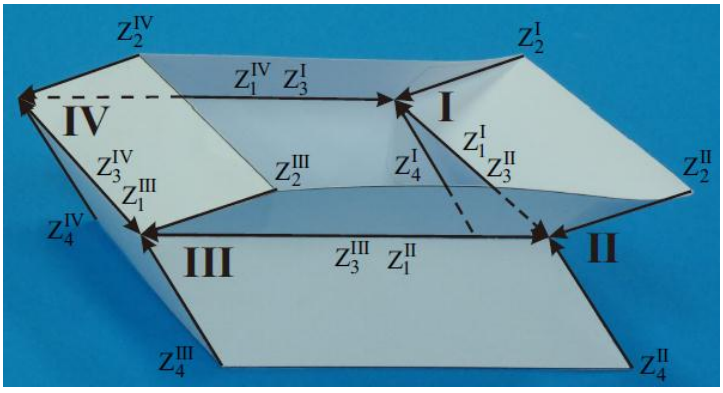

Fig. 4.7 A 4-sided deployable prismatic structure with a parallelogram intersection.

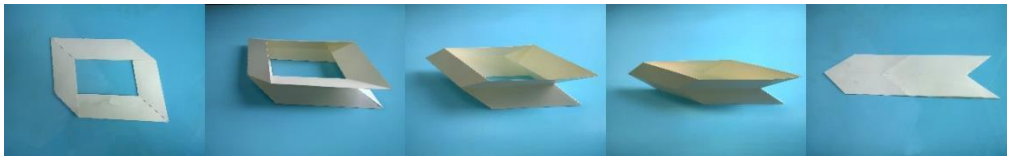

a) b) c) d) e)

Fig. 4.8 Deployment process of the deployable prismatic structures with a parallelogram intersection.

The deployment process includes two phases. Firstly, as shown in Fig. 4.8 a) and b), the structure deploys from a compact 2-D structure to a 3-D structure until it reaches its maximum height, as shown in Fig. 4.8 c). Then, the structure continues to fold into the second compact 2-D structure, as shown in Fig. 4.8 d) and e). The deployment processes are reversible at any point.

4.3.2 2*n*-sided prism with a plane symmetric intersection

Another set of parameter relationships are obtained by considering a plane symmetric correspondence relationship, as shown in Fig. 4.9 ,

$$\begin{gathered}\theta_2^j = \theta_2^{2n-j+2}, \theta_4^j = \theta_4^{2n-j+2};\\ \alpha_{23}^j = \alpha_{23}^{2n-j+3}, \alpha_{41}^j = \alpha_{41}^{2n-j+1};\\ L_{j+1}^j = L_{2n-j+2}^{2n-j+1};\\ \sum_{j=1}^{n}\cos\left(\alpha_{41}^j\right)L_{j+1}^j = 0, \sum_{j=1}^{n}\cos\left(\alpha_{23}^{j+1}\right)L_{j+1}^j = 0,\end{gathered} \tag{4.26}$$

which also meets the compatibility condition.

According to the relationships in Eqn. (4.26), the corresponding twist angles on sides $j(j+1)$ and $(2n-j+1)(2n-j+2)$ are equal, which also constrain the intersections into planar polygons. Judging from the relationships of the lengths, the 2*n*-sided polygons between the two halves are plane symmetric,

as shown in Fig. 4.10. The symmetric plane is perpendicular to the intersecting polygon and passes the diagonals connecting vertices I and n+1.

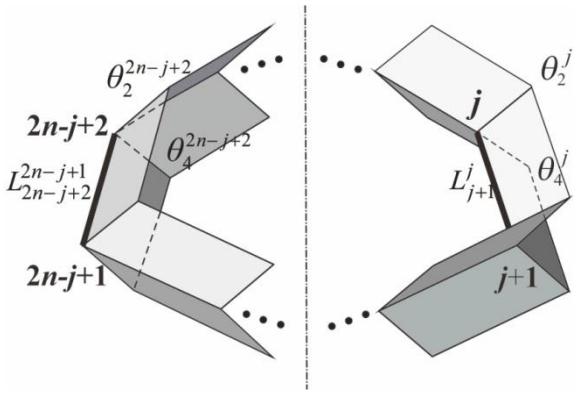

Fig. 4.9 Linkage j corresponds to $2n - j + 2$.

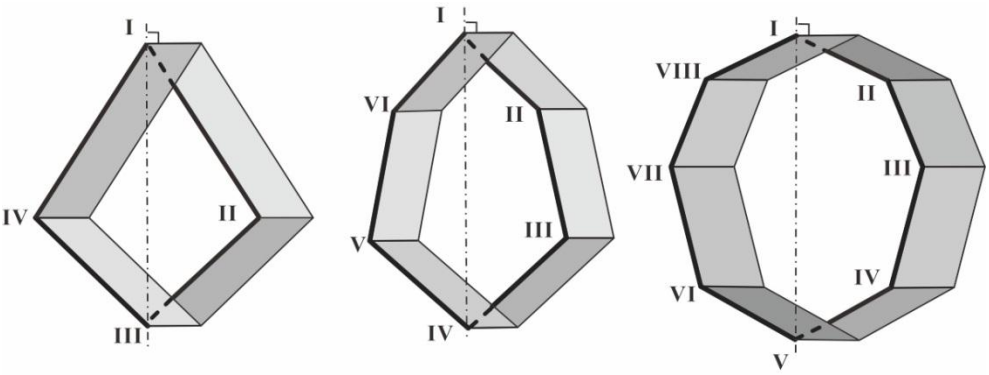

a) b) c)

Fig. 4.10 Upper-half views of $2n$-sided prisms with line symmetric intersections: a) quadrilateral, b) hexagon, c) octagon.

When $n = 2$, the $2n$-sided polygon is kite-shaped with twists and lengths that satisfy $\cos\alpha_{23}^{\mathrm{II}} L_{\mathrm{II}}^{\mathrm{I}} + \cos\alpha_{23}^{\mathrm{III}} L_{\mathrm{III}}^{\mathrm{II}} = 0$. An example is shown in Fig. 4.11, whose folding process is shown in Fig. 4.12. The folding unit in the metamaterial proposed by Schenk and Guest (Schenk and Guest 2013) belongs to a deployable structure with a plane symmetric, kite-shaped intersection.

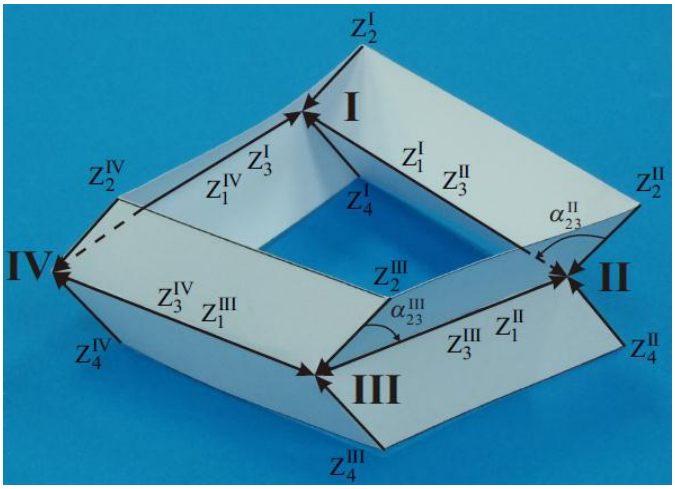

Fig. 4.11 A 4-sided deployable prismatic structure with a kite intersection.

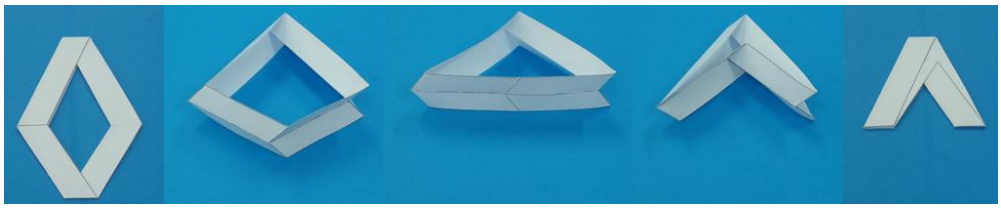

a) b) c) d) e)

Fig. 4.12 Deployment process of the deployable prismatic structure with a kite intersection.

Similar to the previous 4-sided deployable structure, the deployment process of the kite-intersection structure also has two reversible phases, as shown in Fig. 4.12, based on its maximum height, as shown in Fig. 4.12 c). The second 2-D structure is significantly more compact than the first 2-D structure. Such characteristics offer this structure great potential in applications, such as emergency shelters and outer space structures.

4.4 Construction of deployable prismatic structures

4.4.1 Unit variations

The deployable prismatic structures obtained from the previous section can be considered as units of a rigid origami pattern, whose geometric conditions have the following variations.

(1) Side lengths

For a unit with rotational symmetric intersections, the lengths L_{j+1}^{j} and L_{j+n+1}^{j+n} are equal. For a unit with plane symmetric intersections, lengths L_{j+1}^{j} and L_{2n-j+2}^{2n-j+1} are equal and associated with the twist angles described in Eqns. (4.26). For example, to design a 4-sided unit with a plane symmetric intersection, as in Fig. 4.13 b), the lengths of the sides should satisfy the following: $L_{\mathrm{II}}^{\mathrm{I}}=L_{\mathrm{I}}^{\mathrm{IV}}$, $L_{\mathrm{III}}^{\mathrm{II}}=L_{\mathrm{IV}}^{\mathrm{III}}$ and $\frac{L_{\mathrm{II}}^{\mathrm{I}}}{L_{\mathrm{III}}^{\mathrm{II}}}=-\frac{\cos\alpha_{23}^{\mathrm{III}}}{\cos\alpha_{23}^{\mathrm{II}}}=-\frac{\cos\alpha_{41}^{\mathrm{II}}}{\cos\alpha_{41}^{\mathrm{I}}}$.

(2) The value of the twist angles

When the rotation angles about the ridgelines reach π simultaneously, i.e., $\theta_2^j=\theta_4^j=\pi$, both of the halves of the unit fold compactly. According to Eqn. (3.28), the following relationship of the twist angles is obtained,

$$\sin\alpha_{23}^{j}\sin\alpha_{12}^{j}+\cos\alpha_{23}^{j}\cos\alpha_{12}^{j}=\sin\alpha_{34}^{j}\sin\alpha_{41}^{j}+\cos\alpha_{34}^{j}\cos\alpha_{41}^{j}, \qquad (4.27)$$

which is considered as the condition that allows the prismatic structure to be folded flat. According to the relationships of twist angles in Eqns. (4.4) and (4.24), in the unit with a rotational symmetric intersection, the four twist angles of linkage j are independent, though supplementary to the corresponding twist angles of linkage $j + n$. In a unit with plane symmetric intersections, the four twist angles of linkage j are equal to the corresponding twist angles in linkage $2n - j + 2$ and must satisfy the relationships in Eqn. (4.26), which are associated with the side lengths.

(3) Ridgeline lengths

The ridgeline lengths in a single layer, which are aligned with axes Z_2^j and Z_4^j, are independent from other layers. However, to construct deployable prismatic structures that consist of more than two layers, the ridgeline

lengths in each layer should always guarantee that the intersections of the tube are planar, as shown in Fig. 4.13 b) and c).

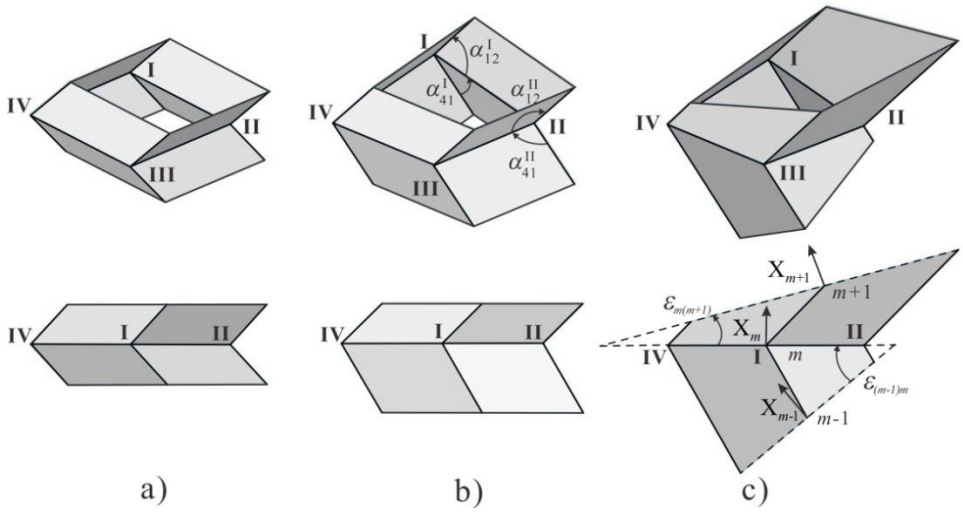

Fig. 4.13 Examples of unit variations: a) the side lengths are all equal, and two layers are symmetric to the intersecting plane; b) the ridgeline lengths in different layers are independent; c) the dihedral angles between two intersections are different.

(4) Dihedral angles

The dihedral angles between the intersections of each layer are independent from other layers. The dihedral angle $\varepsilon_{m(m+1)}$ represents the rotation from intersection plane m to $m + 1$, which is positive in the counterclockwise direction. As shown in Fig. 4.13 c), two dihedral angles $\varepsilon_{(m-1)m}, \varepsilon_{m(m+1)}$ can differ. In the case of parallel intersections, the dihedral angles $\varepsilon_{m(m+1)} = 0$.

4.4.2 Multi-layer deployable prismatic structures

Due to the rigid mobility and planar intersections of a unit, it is feasible to construct deployable prismatic structures with more than two layers. To maintain mobility, any two neighboring layers of the tube should follow the same set of relationships in terms of the geometric and kinematic parameters. If all the intersections in a multi-layer prismatic structure lie on parallel

planes, i.e., all the dihedral angles $\varepsilon_{m(m+1)} = 0$, the structure is defined as straight and otherwise, as curvy.

For a structure with a plane symmetric intersection, the planes of the intersections can only rotate about the axes that are parallel to the line passing vertices I and *n*+1, as shown in Fig. 4.14. The connecting ridgelines should fall on the plane that is perpendicular to the line passing vertices I and *n*+1 (as obtained in Appendix C.2). In contrast, for a structure with a rotational symmetric intersection, the planes of the intersections can rotate about any random axis. Six examples of the straight prismatic structure with rotational symmetric and plane symmetric intersections are shown in Fig. 4.15 a) and b), respectively.

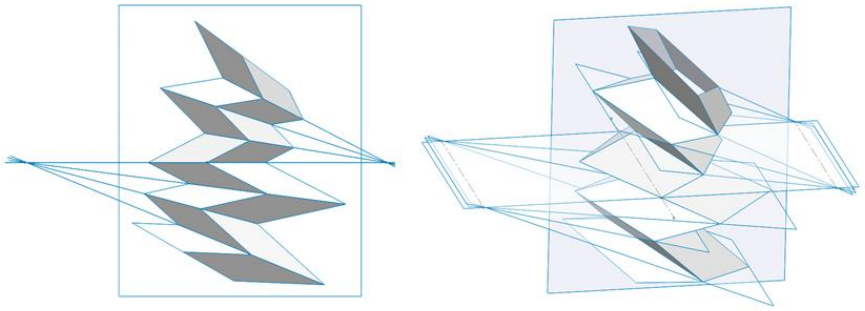

a)

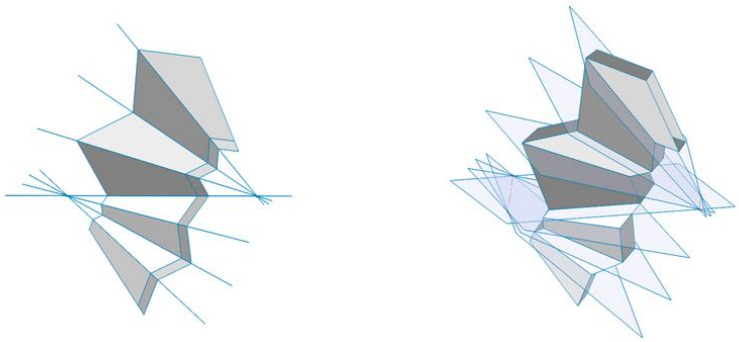

b)

Fig. 4.14 Constructing a curvy prismatic structure with a) a plane symmetric intersection and b) a rotational symmetric intersection.

Depending on the arrangements of the dihedral angles, the configuration of curvy prismatic structures can vary. If all the dihedral angles have the same

sign, positive (or negative), i.e., $\varepsilon_{m(m+1)} > 0$ (or $\varepsilon_{m(m+1)} < 0$), the intersections of the structure rotate in one direction, as shown in Fig. 4.16 a). If the dihedral angles change from being negative to positive, an S-shaped curvy structure can be generated, as shown in Fig. 4.16 b). The dihedral angles in one structure can also be arbitrary, which is shown in Fig. 4.16 c).

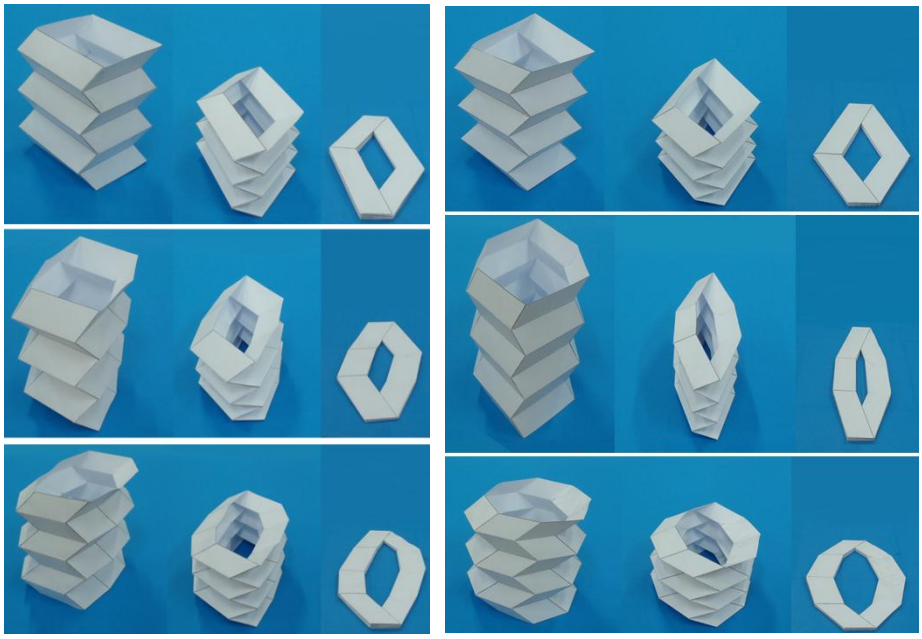

a) b)

Fig. 4.15 2*n*-sided straight, multi-layer prismatic structures with intersections, which are a) rotational symmetric and b) plane symmetric.

Therefore, to design a 2*n*-sided deployable prismatic structure with a rigid origami pattern, the following conditions must be satisfied.

1) The intersections can either be a rotationally symmetric or plane symmetric planar 2*n*-sided polygon. The intersections in a structure should be the projections of the same planar 2*n*-sided polygon on each intersecting plane, which means all the intersection polygons have the same relationship of the side lengths.

2) In every layer of both groups, the ridgelines are parallel.

3) For a deployable prismatic structure with plane symmetric intersections, every ridgeline through the entire structure should be in a direction that is plane perpendicular to the plane of symmetry.

4) To be flat foldable, condition (4.27) should be satisfied between every two layers.

5) The structure with plane symmetric intersections can only curve about the axes that are parallel to the line passing vertices I and n+1. The structure with a rotational symmetric intersection can curve about any random axis.

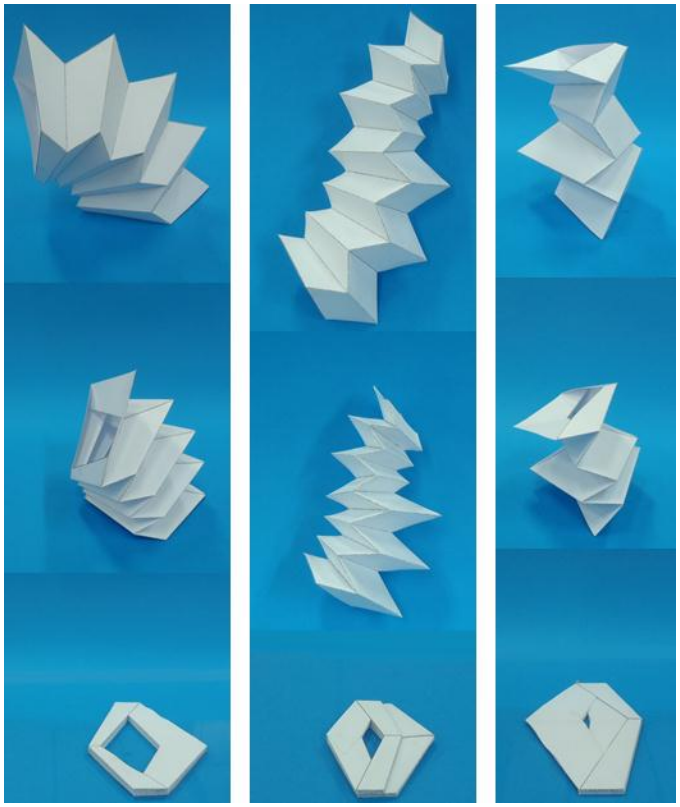

a) b) c)

Fig. 4.16 Three examples of curvy prismatic structures.

4.5 Summary

In this chapter, based on the kinematic property of a spherical 4*R* linkage, its mobile assembly was constructed to form a closed chain. The compatibility conditions of the one-DOF mobile assembly were derived and then solved.

There are two groups of $2n$-sided prismatic structures: one with a rotational symmetry and the other with a planar symmetry. The folding processes of both groups were presented. Based on manipulating the independent parameters, such as the side and ridgeline lengths and the values of the twist and dihedral angles, the unit variations were discussed and presented. Multi-layer deployable prismatic structures were constructed based on the unit variations. The straight and curvy multi-layer prisms were constructed depending on the configuration of the dihedral angles between the intersecting planes. The general design method for the $2n$-sided multi-layer deployable prismatic structures was discussed with the geometric condition of the origami patterns, which guarantees that all of the proposed deployable structures can be deployed and folded along the central axis of the prisms with a single degree of freedom.

The structures can be constructed via the origami technique. However, during the analysis of the spherical $4R$ linkage assembly, we never considered the condition that the sum of four twists around a single vertex is 2π, which is the general condition of an origami pattern that can be formed on a single piece of flat paper. Thus, more than one piece of paper and gluing are required to construct the deployable prismatic structures discussed in this paper.

The multi-layer structure can offer an extremely large deployable ratio when compact folding is achieved. Furthermore, the rigid origami pattern ensures that there is no deformation on the quadrilateral panels, which means repeated deployment and folding are easily realized. With all these characteristics, such deployable structures are expected to have a wide range of engineering applications.

Chapter 5

Deformation of the Miura-ori patterned sheet

5.1 Introduction

In this chapter, the study of the mechanical behavior of the Miura-ori patterned sheet is presented. The Miura-ori patterned sheet is made from a commercially available material, copolymer Elvaloy, through compression molding (Leong and Hamada 2010). The intrinsic mechanical properties of Elvaloy are obtained and subsequently used to define the material in the FE simulation. The quasi-static mechanical tests are carried out on the patterned sheet. The deformations are simulated in ABAQUS/Explicit, which are compared with the mechanical tests. To explore the mechanics of the patterned sheet, a theoretical analysis based on the deformations are presented.

The layout of the chapter is as follows. Firstly, the geometry and preparation of the Miura-ori patterned sheet will be introduced in section 5.2. The experiments setup and results will be introduced in section 5.3. Section 5.4 proposes the FE model in ABAQUS/Explicit and verifies its validity. Section 5.5 discusses the deformations of the patterned sheet and its energy absorption properties. The theoretical analysis is carried out in Section 5.6. Section 5.7 summarizes the chapter.

5.2 Geometries and preparation of the Miura-ori patterned sheet

5.2.1 The geometry of Miura-ori

The Miura-ori pattern can be constructed by the tessellation of multiple units. A unit consists of 4 identical parallelograms, see Fig. 5.1 a). The mountain and valley crease lines are marked as solid and dotted lines, respectively. Due to the Miura-ori's one-DOF mobility (Miura 1989b),

when the lengths a, b and twist angle α are given as constant, the motion of the unit only depending on the dihedral angle θ, see Fig. 5.1 b).

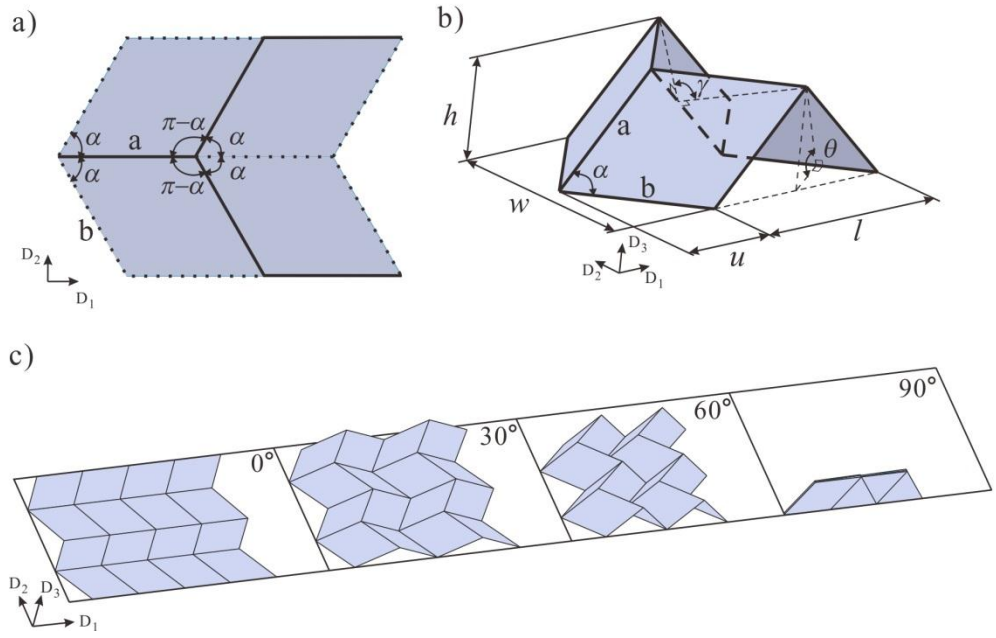

Fig. 5.1 a) A unit of the Miura-ori pattern in the original flat position; b) the definition of parameters; c) the same Miura-ori pattern with different values of dihedral angle θ.

According to Schenk's (Schenk, Allwood et al. 2011a) and Klett's (Klett 2010) work, the outer dimensions of the patterned sheet can be given by

$$h = a\sin\theta\sin\alpha, \tag{5.1}$$

$$w = 2b\frac{\cos\theta\tan\alpha}{\sqrt{1+\cos^2\theta\tan^2\alpha}}, \tag{5.2}$$

$$l = 2a\sqrt{1-\sin^2\theta\sin^2\alpha}, \tag{5.3}$$

and

$$u = \frac{2ab\cos\alpha}{l}. \tag{5.4}$$

To describe the rigid folding motion of the sheet, the additional relationships of the dihedral angles are

$$\sin\left(\frac{\gamma}{2}\right)=\frac{\cos\theta}{\cos\alpha\sqrt{1+\cos^2\theta\tan^2\alpha}}. \tag{5.5}$$

The mobility of Miura-ori pattern is shown in Fig. 5.1 c). Due to the anisotropy of the Miura-ori pattern, the mechanical behavior of the patterned sheet depends on the directions of the loads applied. Thus, two principal directions of the patterned sheet are defined, as direction D1 and D2. Direction D3 is the out-of-plane direction.

5.2.2 Fabrication of the Miura-Ori patterned sheet

The commercially available Elvaloy AC 1820 was selected, which is a copolymer of ethylene and methyl acrylate in pellet form (Dupont 2014). The manufacturing process is shown in Fig. 5.2. First, 25.9g Elvaloy pellets were melted at a temperature of 180 degrees Celsius and compressed into a flat sheet with dimensions of approximately 99 mm long, 99 mm wide and 2.7 mm thick after cooling, see Fig. 5.2 a) and b). The flat sheet was then compressed to form the patterned sheet between the male and female heated stainless steel moulds at 180 degrees Celsius, see Fig. 5.2 c) and d). The thickness of the patterned sheet facets, *T*, turned out to be 1.8 mm on average. Due to the adhesive nature of Elvaloy when melted, mould release agent was applied before each moulding. The Miura-ori pattern on the mould was designed based on the model shown in Fig. 5.1. The dimensions are

$$\alpha=60°,\quad a=b=10.5\,mm,\quad \theta_0=54°. \tag{5.6}$$

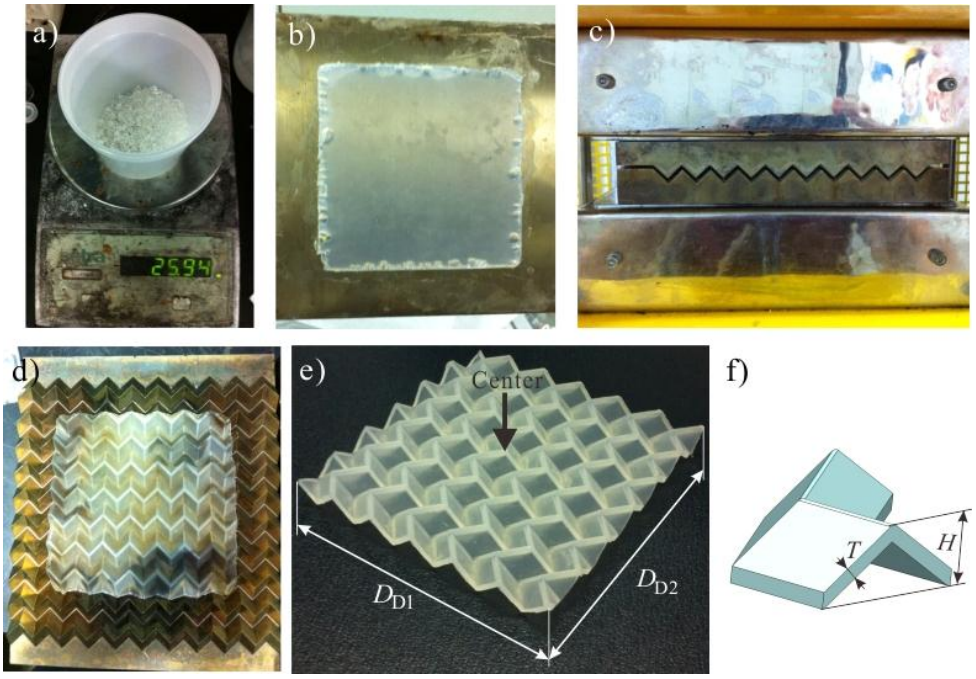

Fig. 5.2 The manufacturing process of Miura-ori patterned sheet is as follows: a) 25.9g Elvaloy pellets were melted and b) compressed into a flat sheet, then, c) the flat sheet was compressed into Miura-ori patterned sheet in d) the heated stainless mould. e) The peripheries were trimmed, and the center and lengths of in direction D1 and D2 are measured. f) The thickness of the panels and fillet on the ridgeling are measured.

Substituting the values in (5.6) to Eqns. (5.1) ~ (5.5) gives

$$h = 7.3\,\text{mm}, \quad w = 15\,\text{mm}, \quad l = 15\,\text{mm},$$
$$u = 7.5\,\text{mm}, \quad \gamma_0 = 110.9^{\circ}. \tag{5.7}$$

Fillets with 0.5 mm radius were added to the ridgelines for milling cutter to work. After the compressed moulding, the patterned sheet is on average 1.9 mm taller than *h*, ie. $H = 9.2\,\text{mm}$, see Fig. 5.2 f).

Finally, to eliminate the bubbles and inconsistent thickness, the Patterned sheets were trimmed into square shape with 6 units in direction D2 and 5 and half units in direction D1, see Fig. 5.2 e). After trimming, the average lengths of the patterned sheet in directions D1 and D2 are $D_{D1} = 88.3\,\text{mm}$, $D_{D2} = 88.4\,\text{mm}$.

5.3 Experiments

Two types of experiments were performed for the Elvaloy flat sheets: uniaxial tensile tests for stress-strain curves and four-point bending tests. For the patterned sheets, two types of experiments were conducted, i.e., compression tests in the global three directions of the patterned sheet and three-point bending tests.

5.3.1 Tests for properties of Elvaloy flat sheet

(1) Tensile test

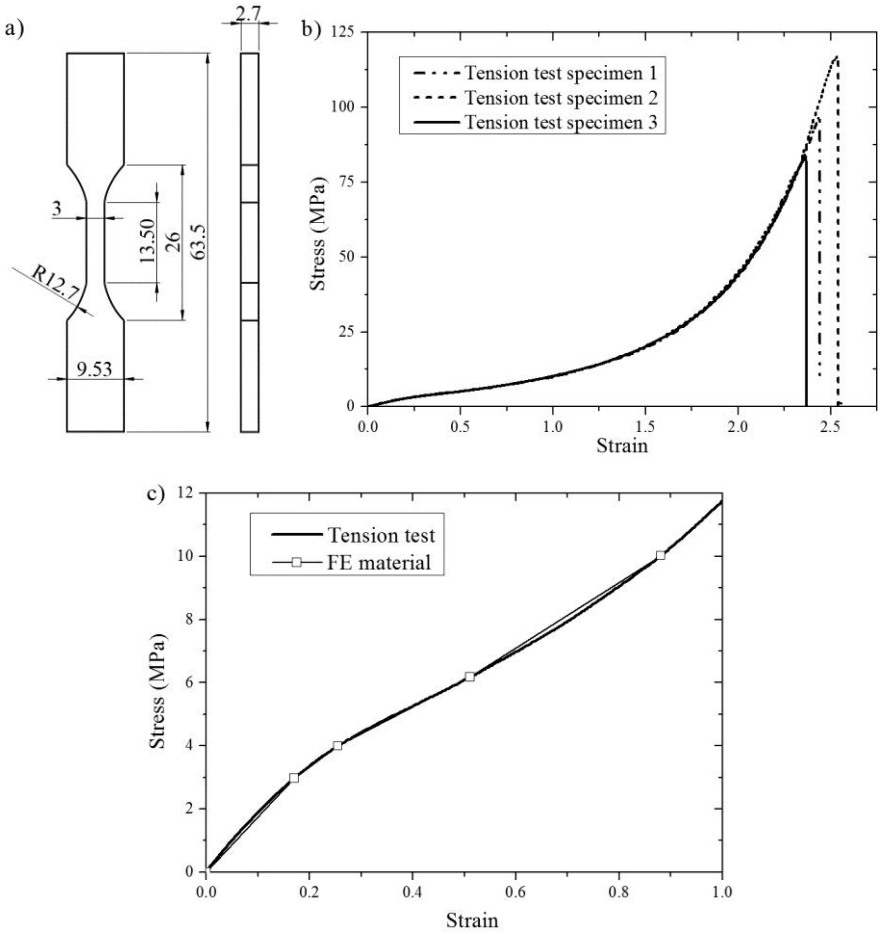

Fig. 5.3 a) the dumbbell specimen; data obtained in tension test: b) true stress strain, c) test result with fitted curve.

Tensile tests with Elvaloy dumbbell samples were performed according to ASTM D638, in order to characterise the mechanical property of Elvaloy. The diameter of the dumbbell is depicted in Fig. 5.3 a). The load-displacement data were obtained, which was then converted into the true

stress-strain curve. A typical stress-strain curve is shown in Fig. 5.3 b). The modulus of elasticity was obtained by fitting the initial linear portion of the curve, which is 18.6 MPa, see Fig. 5.3 c).

(2) Four-point bending test

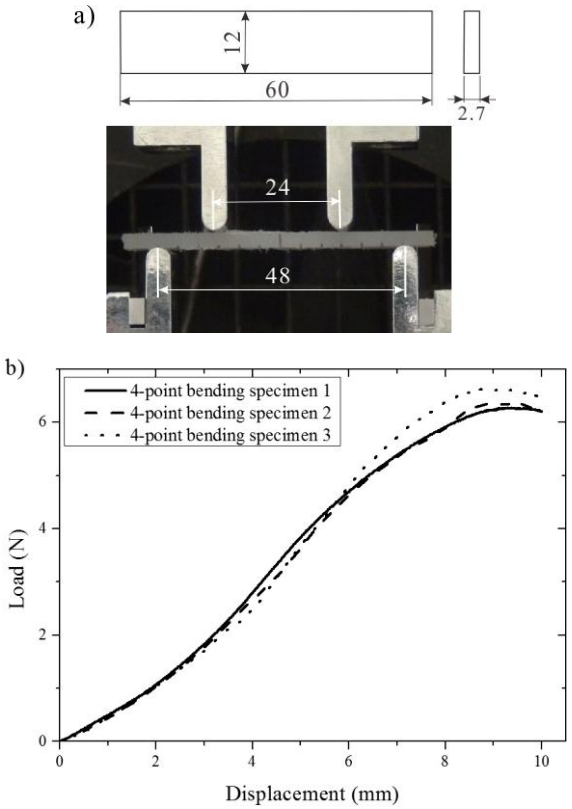

Fig. 5.4 a) The diameter of the specimen and test setup, b) load-displacement curve of the four-point bending test.

According to the standard test method for flexural properties ASTM D6272, the four-point bending test was performed. The diameters of the specimen and test setup are shown in Fig. 5.4 a). This was also to be used later in validating the material property in the finite element analysis. The load and displacement were measured, as shown in Fig. 5.4 b). Around the end of the test, the deformation was very large and there was some slippage observed between the specimen and the roller supports. Different from the approach in (Dai and Cannella 2007), which directly measure the folding force of a crease in a carton sheet, our experiment simply captures the behavior of the material under bending to estimate the bending in the facets or around the ridgelines of the patterned sheet.

5.3.2 Tests for patterned sheets

(1) Out-of-plane compression test

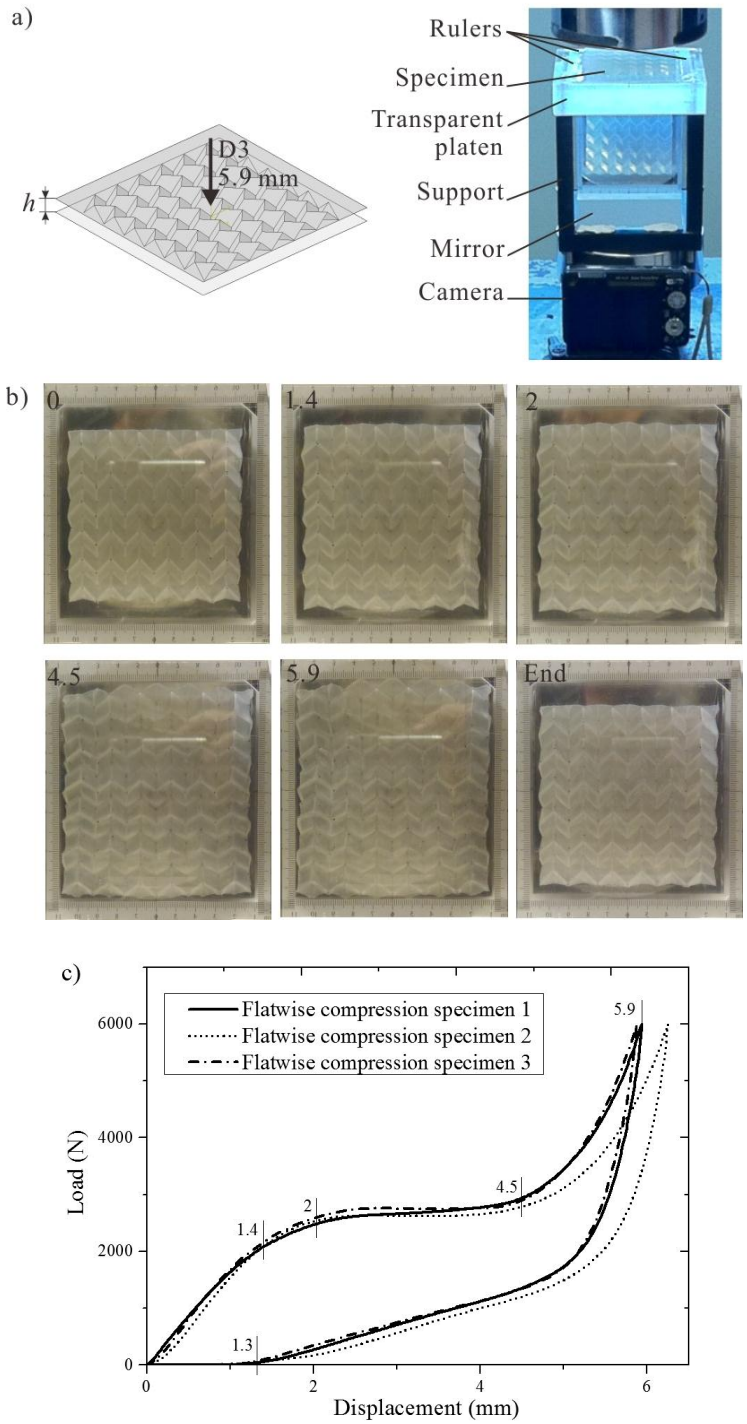

Fig. 5.5 Out-of-plane compression: a) the setup, b) deformation of the patterned sheet, c) the load-displacement curve.

To evaluate the characteristics of the patterned sheet in the out-of-plane direction, compression tests were performed, together with an unloading phase. Fig. 5.5 a) shows the setup. A mirror was fixed under the transparent bottom platen at 45 degrees to the vertical so that the camera pointing to the mirror can capture the successive in-plane deformation of the specimen. To track the in-plane displacement of the vertices, the vertices were marked and reference rulers were glued on the edge of transparent platen, see Fig. 5.5 b). The load-displacement curve is plotted in Fig. 5.5 c). The curve shows approximately five stages of the deformation. From the displacement at 0 to 1.4 mm, the deformation can be considered as linear elastic, where the load increases linearly with the displacement (Stage 1). The load increases gradually from the displacement at 1.4 to 2 mm, until a plateau has reached (Stage 2). At stage 3, the load remains constant and the patterned sheet structure collapses when the flat panels started buckling. During the displacement of 4.5 to 5.9 mm, the Miura-ori structure further collapsed with some facets touching the bottom platen. The load increases rapid with the displacement. This is followed by the unloading phase after the load reached 6 KN. The patterned sheet sprang back. After the complete unloading, the patterned sheet had a permanent displacement of 1.3 mm, and is slightly larger in area. The movement of the vertices is shown in Fig. 5.5 b), which demonstrates that the central vertex stayed still and each unit expanded evenly.

(2) In-plane compression tests

In-plane compression tests were carried out for the patterned sheet to investigate its deformation behavior. The sheet was sandwiched between two smooth and transparent rigid walls spaced at 11mm, to stop possible overall buckling, (Fig. 5.6 a). The thickness of the loading plate was 10mm. The loading plate pushed the patterned sheet at 10mm/min in direction D1 and D2, respectively. The deformations were recorded by camera during the tests. Deformation of the sheet exhibited a feature of overall negative Poisson's ratio (Schenk 2011c), see Fig. 5.6 b) and c).

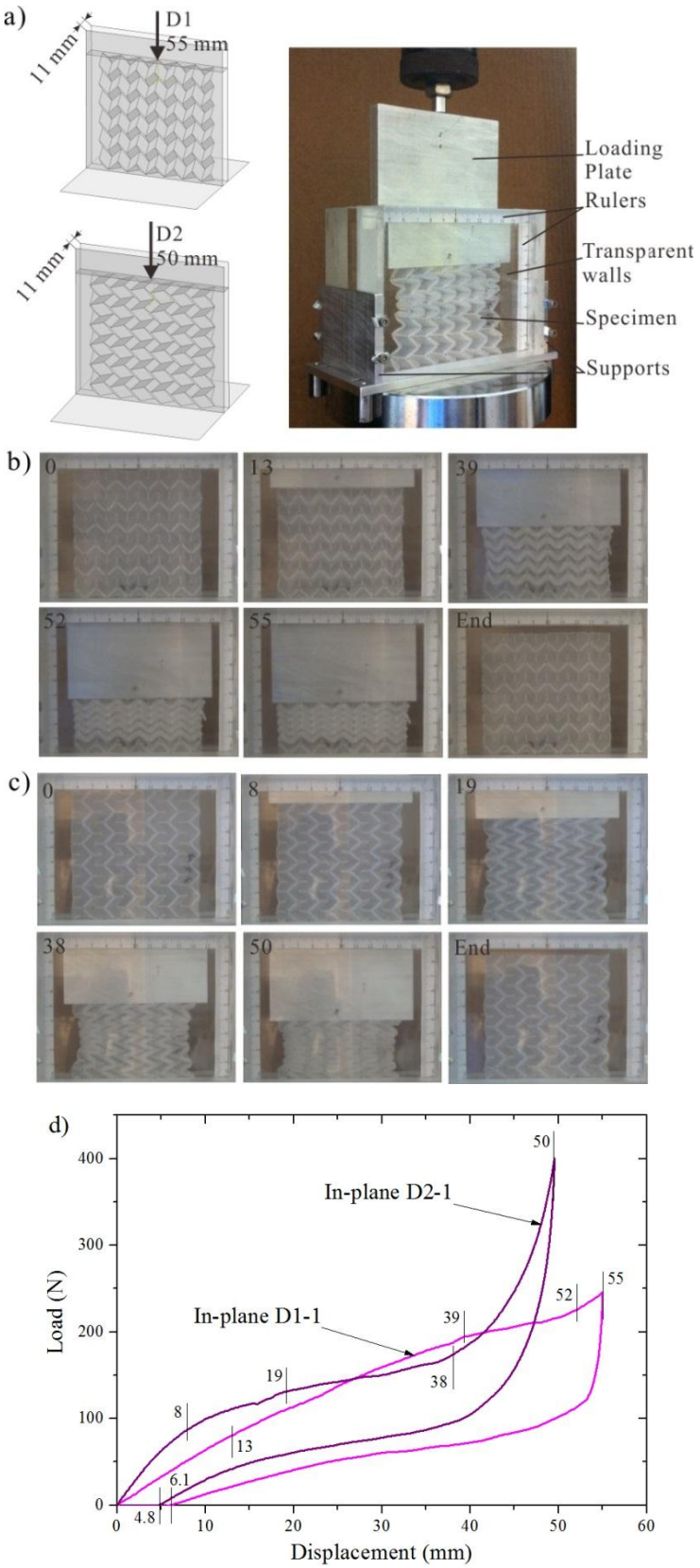

Fig. 5.6 The in-plane compression: a) the setup, b) test in direction D1, c) test in direction D2, d) the load-displacement curves.

The load-displacement curves are plotted in Fig. 5.6 d). Results for D2 showed good repeatability while for D1 direction they were less so, probably due to the friction between the patterned sheet and the transparent walls. Thus, only the curves of the in-plane D1-1 and D2-1 specimens are used. The patterned sheet starts densification at about 38mm in test D2 and 52mm in test D1, which shows the folding range in D1 is larger than that in D2. After complete unloading, there was a permanent displacement of 6.1mm and 4.6mm, in D1 and D2 directions, respectively.

(3) Three-point bending test

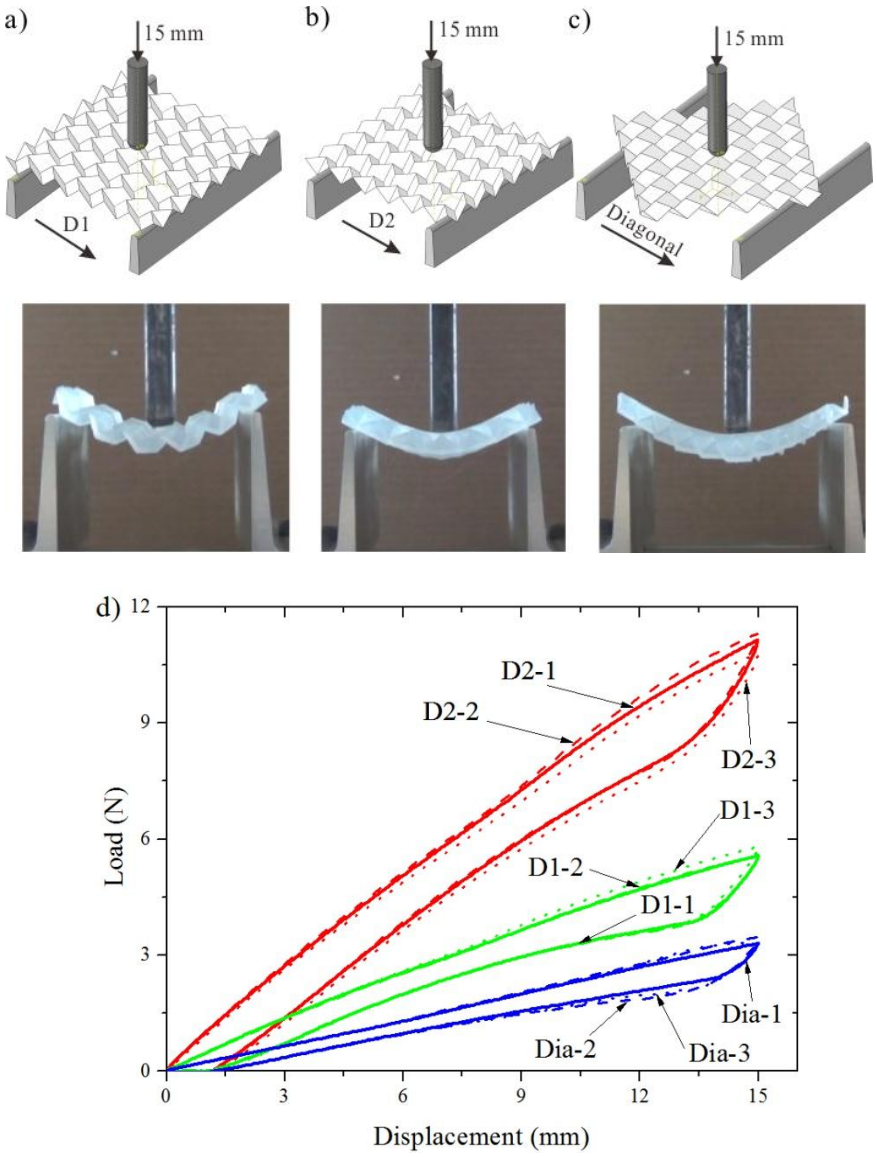

Fig. 5.7 The three-point bending test in directions, a) D1, b) D2 and c) Diagonal, and d) the load-displacement curves.

Schenk (Schenk 2011c) carried out three-point bending experiments on the paper model of the Miura-ori, which demonstrated the static configurations of the Miura-ori under three loading conditions. In this study of our specimens, similar to Schenk's, three-point bending tests for three arrangements of setup were conducted, with the deformations mainly along D1, D2 and Diagonal directions, respectively, (Fig. 5.7 a~c). A rigid stylus was used to apply a point load at the centre. Due to the friction between the specimen and loading stylus, the axis of the stylus always passed through the central vertices. As shown in Fig. 5.7 d), the load-displacement curves appear almost linear. At the same value of displacement, the corresponding load in test D2 is twice that in test D1 and about 3.7 times in test Diagonal. After the complete unloading, there was a permanent displacement of about 1.3 mm. The deformed patterned sheets were observed to have slowly sprung back to the original shape, after the tests.

5.4 Finite element analysis

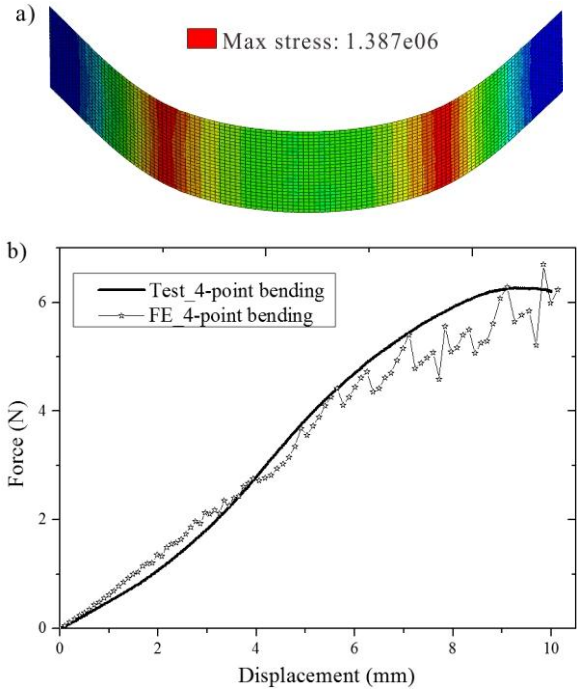

Fig. 5.8 Validation of material model performed on the four-point bending test: a) FE model after simulation, b) the comparation between test and FE result.

Commercial software ABAQUS/Explicit was employed to study the deformation of specimens under the same conditions as for the tests. Details of deformation from the finite element analysis are reported.

5.4.1 Validation of material constitutive model

A user defined isotropic elastic-plastic material is implemented in ABAQUS/Explicit for Elvaloy. The value of density was taken from the data sheet (Dupont 2014) and stress-strain curve from the tension test (Fig. 5.3 c) was used. The values are density $\rho = 942\ \mathrm{kg/m^3}$ and Young's modulus $E = 18.6\ \mathrm{MPa}$. The value of Poisson's ratio was assumed $\nu = 0.35$, based on this property of other similar polymers. This material model in ABAQUS/Explicit was validated by simulating the four-point bending test, see Fig. 5.8 a). The specimen was modelled with 4 node quadrilateral shell element S4R, whose size was 0.5 mm. The displacement was applied to the load span and the reaction force was calculated. Fig. 5.8 b) shows the force-displacement curves from the simulation and test. The simulation shows good agreement with the test up to a large value of displacement.

5.4.2 FE simulations of patterned sheet

The patterned sheet model was first built in SolidWorks by tiling identical Miura-ori units shown in Fig. 5.1. Such a patterned sheet was then meshed and modelled with shell elements of type S4R in ABAQUS/Explicit. The previously defined material constitutive relation was used. In order to further validate the FE model, compression test in the out-of-plane direction was simulated. The loading and supporting platens were both treated as rigid elements (see Fig. 5.5 a). The bottom platen was fully fixed while the top one was used to slowly apply displacements of up to 5.9 mm, which is the same as that in the test (Fig. 5.5 c). Self-contact was defined, which took into account hard contact and friction between the platens and the patterned sheet. Both the reaction and the displacement of the loading plate were noted. Several modelling parameters may affect the accuracy of the simulation and their sensitivity was studied.

(1) Element size

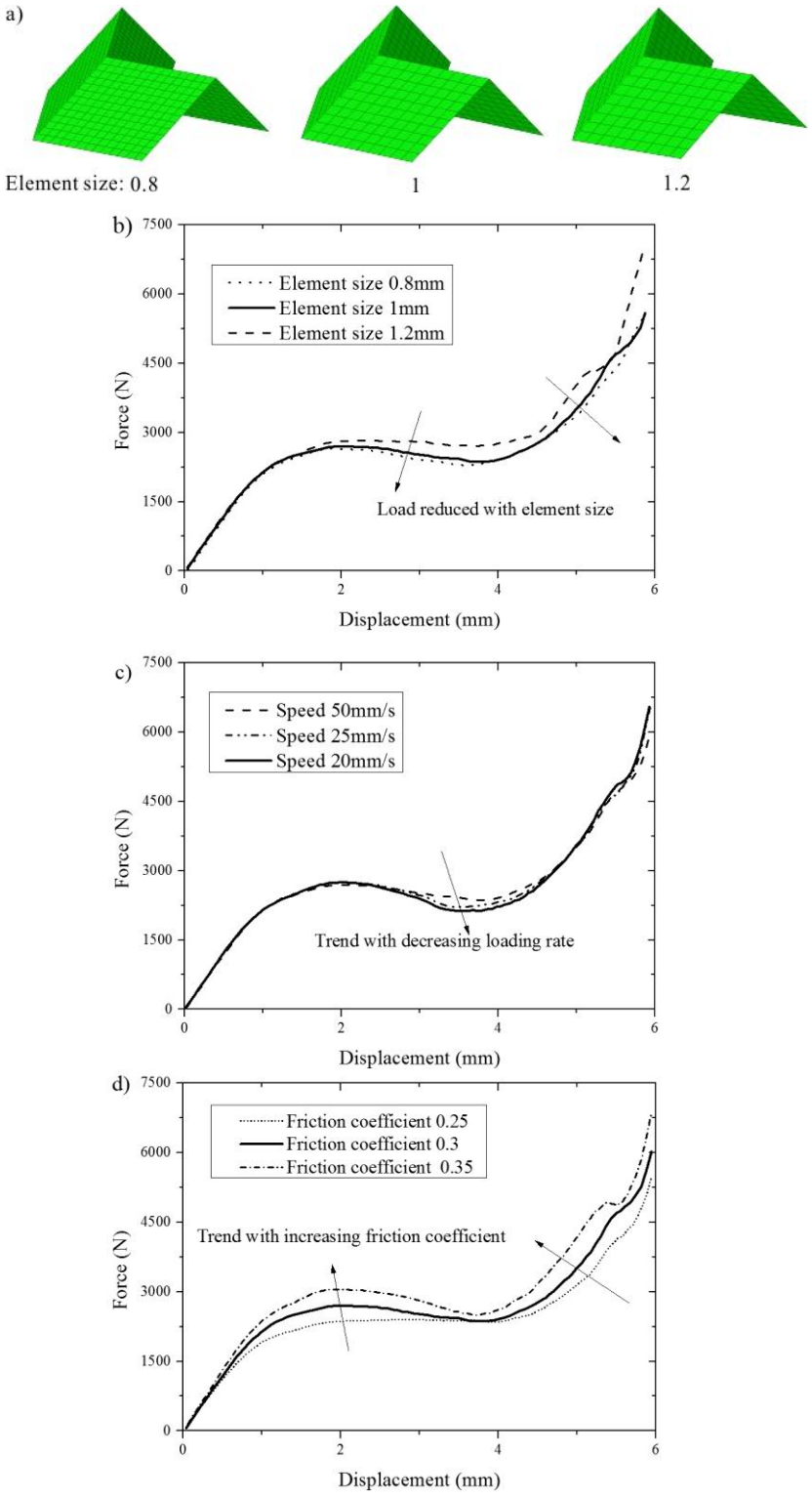

Fig. 5.9 The influence of model parameters in the simulation of out-of-plane compression: a) different sizes of the elements are investigated; the curves of different b) element sizes, c) loading rates and d) friction coefficients.

Different mesh sizes were used as shown in Fig. 5.9 a), and Fig. 5.9 b) plots the load-displacement curves obtained from FE. A smaller element size of 1.0 mm resulted in a reduced force compared that for 1.2mm size, but the CPU time increased significantly. Further refinement to 0.8mm did not seem to improve the accuracy significantly. Hence an element size of 1 mm was selected as the default element size for all the subsequent simulations.

(2) Loading rate

In order to simulate the quasi-static experiments in the FE analysis with an acceptable computing time, the loading rate in the simulation has to be considerably higher than that employed in the tests to reduce the CPU time, while the kinetic energy generated during the simulation should be lower than 5%. Therefore, a compression speed of 20, 25, 50 mm/s was applied, respectively, and their corresponding results are compared in Fig. 5.9 c). The force seems not sensitive to the loading rates for most values of displacement, though a speed of 20mm/s gave the lowest value of the force. Subsequently, 20mm/s was chosen as the compression speed of the top platen.

(3) Friction

In the out-of-plane compression test, the patterned sheet tends to expand in D1 and D2 directions when compressed by the loading platen in the D3 direction. The friction between sheet and the two platens resists this relative movement. Fig. 5.9 d) shows the FE load-displacement curves for three different value of coefficient of friction. As expected, the force increases with the value of friction coefficient. A friction coefficient of 0.3 gives reasonable agreements with the test (Fig. 5.10) and hence was used.

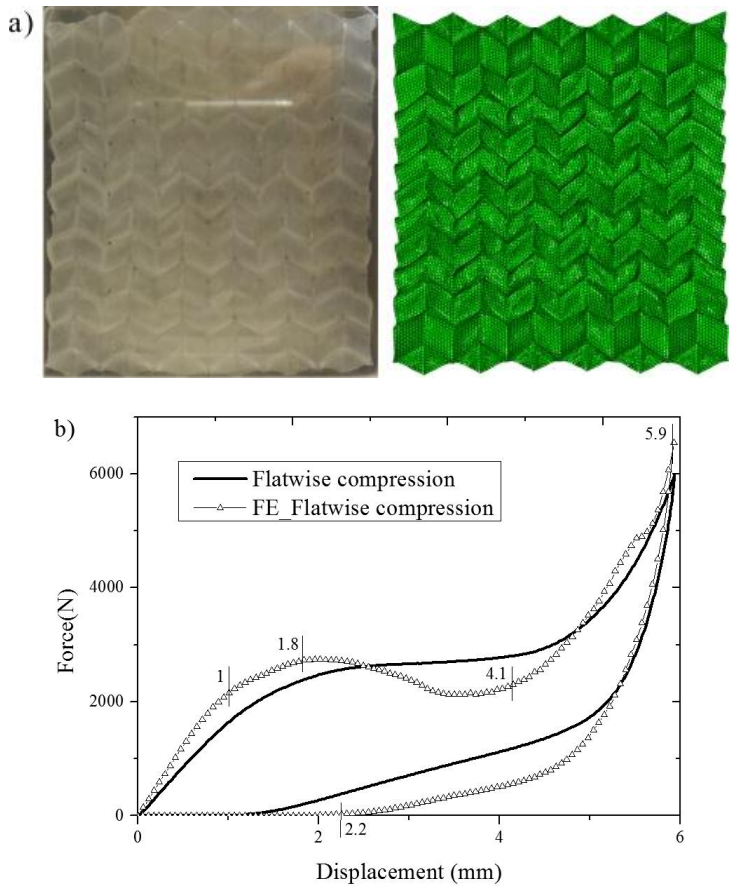

Fig. 5.10 The simulation results of out-of-plane compression compared with test: a) deformations b) the force-displacement curves.

5.4.3 FEA results

After validation of the FE model, FE simulations were performed for the in-plane compression and three-point bending tests. The FE models were set up as shown in Fig. 5.6 and Fig. 5.7. Except for the patterned sheet, all the parts in the simulations were defined as rigid. The supporting parts were completely fixed. Self-contact was defined, including hard contact and friction. The reaction forces and displacements at the reference points of the loading parts were obtained. In the in-plane compression simulations, the patterned sheet model was compressed in D1 and D2 directions at displacements 55 mm and 50 mm, respectively, matching the test data shown in Fig. 5.6 d). In the three-point bending simulations, the loading stylus, whose axis went pass the central vertex, was displaced 15 mm in D3 direction corresponding to the test data in Fig. 5.7 d).

The simulation results are shown in Fig. 5.11 and Fig. 5.12. The simulation result of the in-plane D1 compression fits closely to the test data in the overall energy absorption and elastic section, see Fig. 5.11 c). It shows a softer behavior in the plastic section and unloading which is ascribed to a less-accumulated structure compared to the test sample. The simulation for the in-plane compression D2 shows not only comparable trend in the force-displacement curve but also a smaller reaction force value compared with the test data, which can be ascribed to the lack of thickness in the shell elements. The adjacent facets of the patterned sheet in the tests initiated interactions at a small displacement, while being virtually untouched in the FE model.

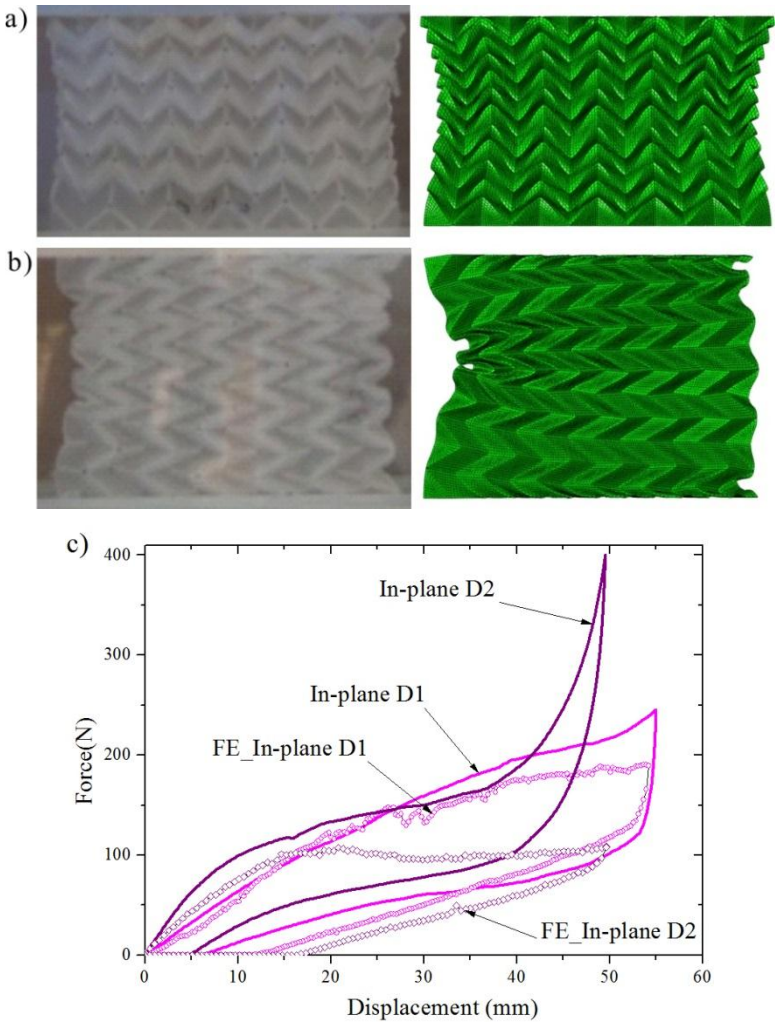

Fig. 5.11 The simulation results of the in-plane compression in directions a) D1 and b) D2; c) the force-displacement curves are compared with the tests.

In the three-point bending simulations, the simulation result shows acceptable consistency with the test data, see Fig. 5.12.

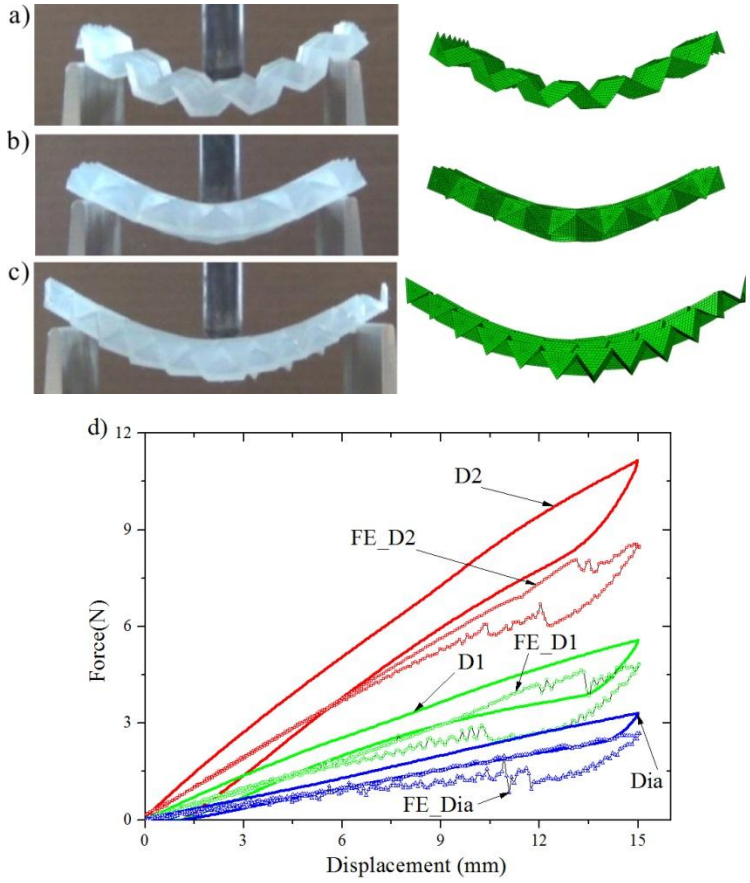

Fig. 5.12 The simulation results of three-point bending test in directions a) D1, b) D2 and c) Diagonal; d) the force-displacement curves are plotted.

5.5 Discussion

5.5.1 Deformations

Corresponding to the test curve, the curve obtained from the FE simulation of the out-of-plane compression shows five similar stages as shown in Fig. 5.10 b), which can be related to the deformation phenomena of the patterned sheet, see Fig. 5.13 a).

In the linear elastic stage from the displacement at 0 to 1 mm, the dihedral angle γ increases while θ decreases, as a result, the patterned sheet expands slightly. In stage 2, from the displacement at 1 to 1.8 mm, the facets started to deform. In stage 3, from the displacement at 1.8 to 4.1 mm,

the buckling of the facets turns the mountain and valley ridgelines of each unit into rotational symmetrical J shapes. During the displacement of 4.1 to 5.9 mm, after the facets touching the platens, the structure of the patterned sheet collapses and densification begins. In the unloading stage, the compactly compressed patterned sheet springs back together with the loading platen to a height which is 2.2 mm lower than the original. However, the changes of the shape after the test are less than that in the simulation.

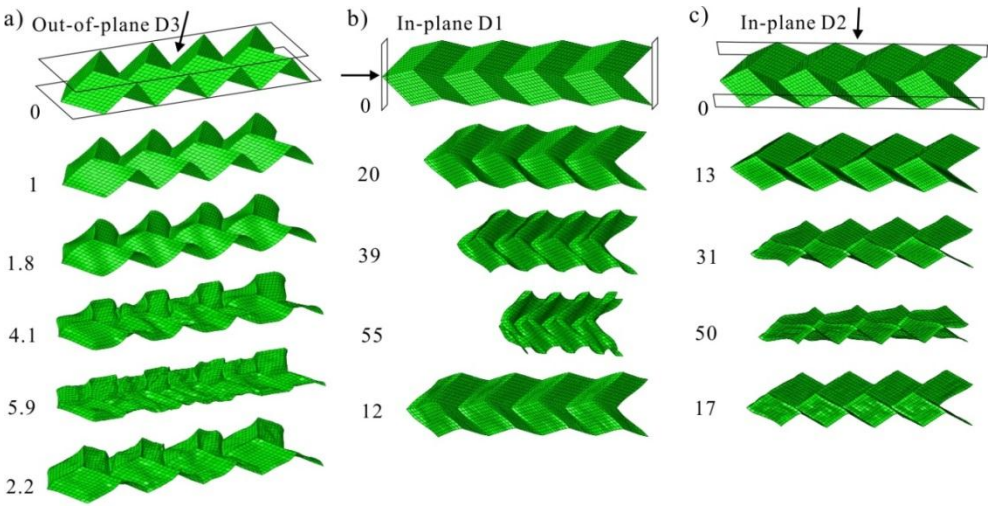

Fig. 5.13 The typical deformation in simulations: a) out-of-plane compression, in-plane compression b) D1, c) D2.

Compared with the deformation in the out-of-plane compression, the deformations in in-plane compression simulations display less bending on the facets. In the beginning of in-plane compression D1, see Fig. 5.13 b), the dihedral angle γ decreases at first while angle θ increases, which corresponds to the waist shape of the patterned sheet in the middle of the compression (Fig. 5.6 b). Then angle γ returns to its original value whilst angle θ reaches its maximum value and the structure is compactly compressed. In the simulation of the in-plane compression D2 (Fig. 5.13 c), the dihedral angle γ always decreases with θ's increase until compactly compressed.

By checking the PEEQ plot of the three-point bending simulations in ABAQUS, it shows that no plastic deformations took place on the patterned sheet. The deformations of the center units are shown in Fig. 5.14.

Compared with its original shape, the unit deforms most when the displacement is at 15mm. In the simulation for D2, the distance V2V5 decreases, while V1V4, V3V6, V1V3 and V4V6 increases, see Fig. 5.14 a) and c). In the simulation for D1, V1V3 and V4V6 extend almost the same as in simulation D2, but distances V1V4, V2V5 and V3V6 change less, see Fig. 5.14 b). In the simulation for Diagonal, the unit deforms the least, see Fig. 5.14 d).

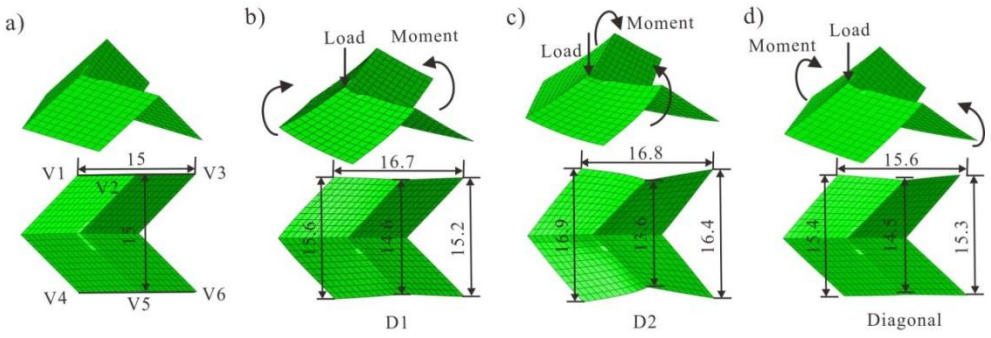

Fig. 5.14 a) The original shape of the center unit; the largest deformations of the center units in simulations of three-point bending b) D1, c) D2 and d) Diagonal.

The typical MISEs plots of the patterned sheets in all the simulations are shown to check the distributions of stress. It's apparent that in Fig. 5.15 a), the valley ridgelines in touch with the supporting platen contribute the most to the reaction force in the out-of-plane compression. In the in-plane compression D1, the mountain ridgelines parallel to D1 contribute the most to the reaction force, see Fig. 5.15 b). The reaction force in the in-plane compression D2 is mainly generated from the folding of all the ridgelines, see Fig. 5.15 c). In the three-point bending simulations, it appears that the stress concentrates on the center unit in D2 simulation, see Fig. 5.15 e). In simulations D1 and Diagonal, three rows of units in the middle deform the most, see Fig. 5.15 d) and f), respectively.

5.5.2 Energy absorption

Due to the nature of Elvaloy, the patterned sheet can be compactly compressed and springs back without destroying its structure. The absorbed energy results in the dimension changes and hardening of the patterned

sheet after recovery. Before densification, the patterned sheet absorbs the most energy under out-of-plane compression with a displacement about half of its height. The force-displacement curve in Fig. 5.5 c) shows a smooth and constant behaviour, especially when buckling is undergone.

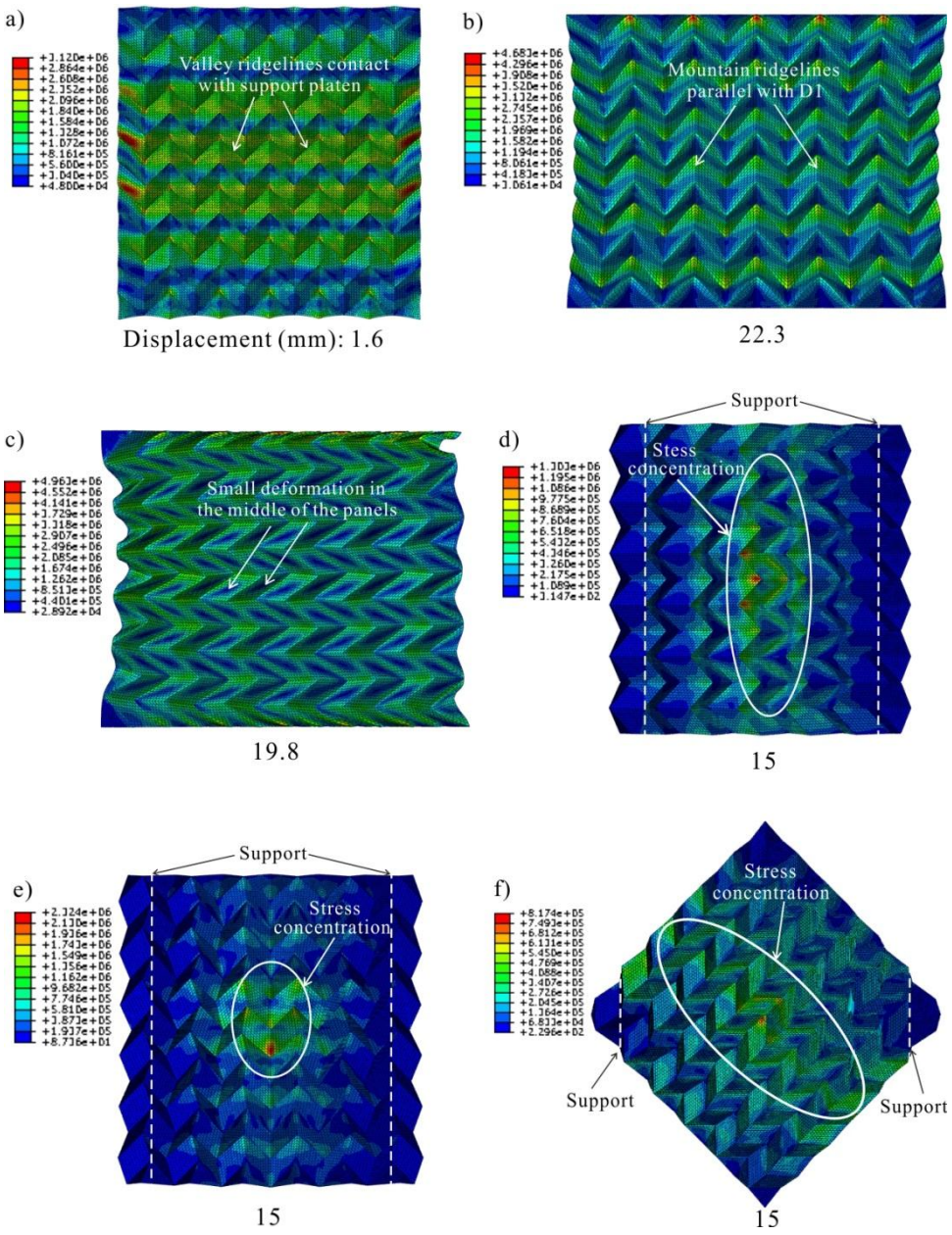

Fig. 5.15 MISEs plot of the patterned sheet in simulations: a) out-of-plane compression; b) in-plane compression D1 and c) D2; three-point bending d) D1, e) D2, f) Diagonal.

On the other hand, in the in-plane compression tests, the patterned sheet can be compressed about 60% and 40% of its length respectively in D1 and D2

directions before densification. The patterned sheet absorbs 50% more energy in the in-plane D1 direction than D2. According to the PEEQ plot of the patterned sheet in the simulations for three-point bending tests, the patterned sheet exhibits no plastic deformations, which limited the prediction of its energy absorption capacity in such loading situation.

5.5.3 Parallel parameter study

For potential applications, the mechanical behavior of the patterned sheet can be designed to meet a range of specific requirements. To provide design instruction, parallel parameter studies on the thickness of the facet *T* and angle α of the patterned sheet were carried out independently utilising the established FE model. The other parameters of the unit in the patterned sheet are still set as previously, as well as using the same tessellation of the units. The dimensions of the patterned sheet with different values of α are listed in Table 5.1.

Table 5.1 Dimensions of the patterned sheets

α (degree)	30°	50°	70°	80°
D_{D1} (mm)	115.2	98.9	80.6	72.8
D_{D2} (mm)	40.5	72.3	107.1	120.7
h (mm)	4.2	6.5	8.0	8.4

In the out-of-plane and in-plane compression simulations on patterned sheets with different *T*, it's obvious that the patterned sheets of larger thickness, among 1.5 mm, 2 mm and 2.5 mm, generate greater reaction force to resist compressions (see Fig. 5.16 a, b and c). For the patterned sheets with different α, the simulation results show that smaller α leads to a stronger structure in all three directions of compressions (see Fig. 5.16 d, e and f). The patterned sheets of larger α generate lower reaction forces in the out-of-plane and in-plane D1 compressions, whilst increase the stiffness in the in-plane D2 compressions.

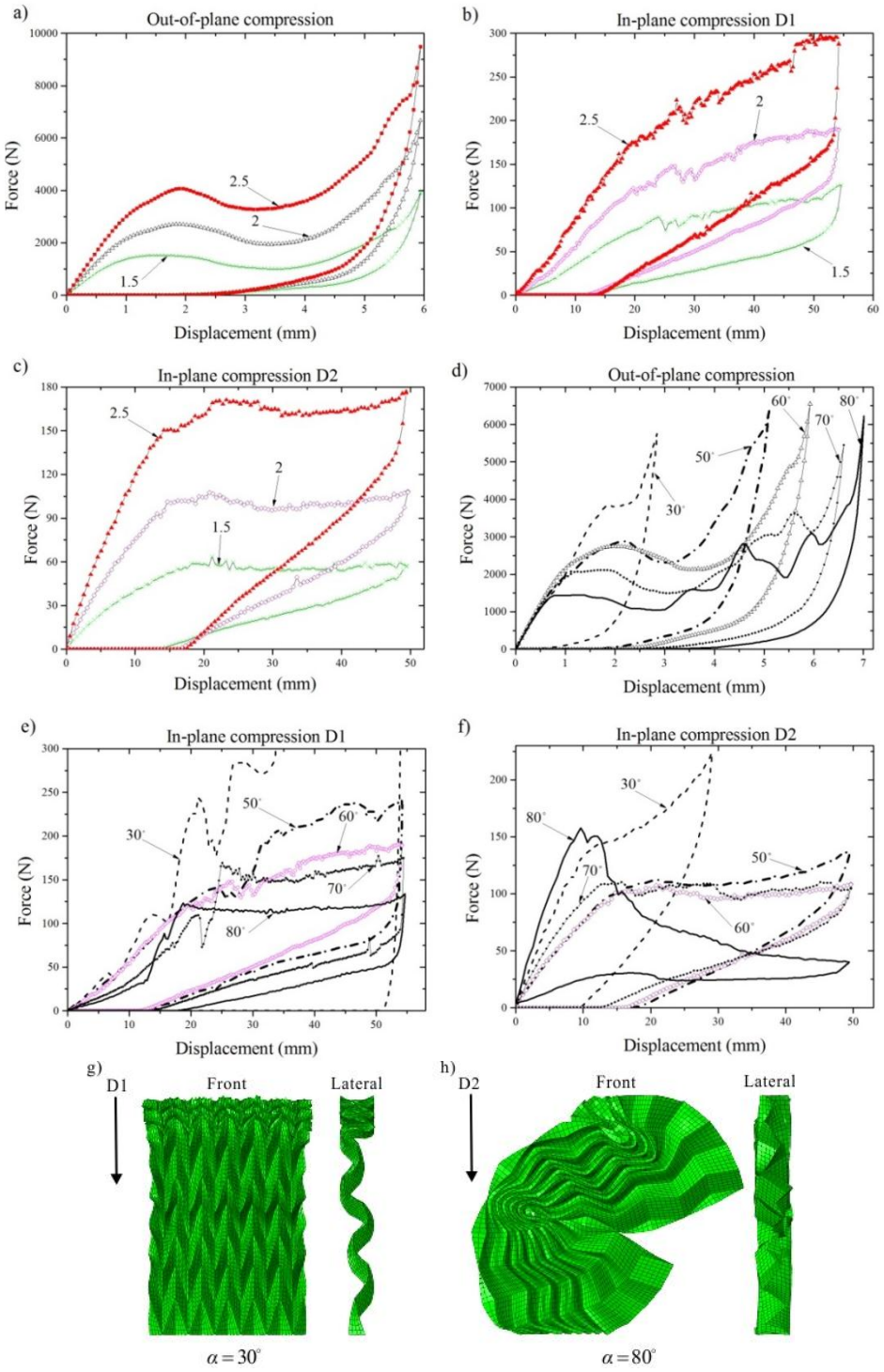

Fig. 5.16 Parallel parameter studies: thickness of facet *T*, a) out-of-plane compression, b) in-plane compression D1, and c) D2; angle α, d) out-of-plane compression, e) in-plane compression D1, and f) D2; the deformations of the sheet of g) $\alpha = 30^{\circ}$ in in-plane compression D1, h) $\alpha = 80^{\circ}$ in in-plane compression D2.

When angle α is too small or large, $\alpha = 30^\circ$ or $\alpha = 80^\circ$ as shown in Fig. 5.16 e) and f), the patterned sheets become unstable in the in-plane direction D1 or D2, respectively. Under in-plane D1 compression as shown in Fig. 5.16 g), the sheet of angle $\alpha = 30^\circ$ tends to buckle in the out-of-plane direction, which was stopped by the walls. It subsequently started local densification at the side closest to the loading plate. When subjected to in-plane D2 compress as shown in Fig. 5.16 h), the sheet of angle $\alpha = 80^\circ$ twists around two centers, which buckle first, instead of contracting in the D2 direction. Thus, in these extreme cases, new tessellation configurations are needed to make the sheet stable under in-plane compressions.

5.6 Theoretical analysis

5.6.1 Out-of-plane compression

According to the principle of virtual work, in the out-of-plane compression, the following relationship is obtained,

$$F_{\mathrm{D3}} \cdot dh = \sum \left(M_\theta \cdot d\theta \right) + \sum \left(M_\varphi \cdot d\varphi \right), \tag{5.8}$$

in which φ is half of the dihedral angle γ, i.e. $\varphi = \frac{\gamma}{2}$, representing the rotation of a single facet around the ridge; F_{D3} is the reaction force in direction D3, see Fig. 5.17 a) ; dh, $d\theta$ and $d\varphi$ are the changes in height h, angles θ and φ, respectively, h and θ decrease whilst φ increases during the compression; M is the corresponding moments (Yu and Zhang 1996) and

$$M = \frac{EI}{R}, \tag{5.9}$$

where I is the second moment of cross-section of the ridge, R is the radius of curvature after bending and

$$I_\theta = I_\varphi = \frac{bt^3}{12}, \quad R_\theta = \frac{nt}{\theta_0 - \theta_i}, \quad R_\varphi = \frac{nt}{\varphi_i - \varphi_0}. \tag{5.10}$$

Here, t is the thickness of the ridge lines, $t = 1.9\,\mathrm{mm}$, and nt is half of the width of a hinge. In a Miura-ori unit, there are eight of each rotational displacement, $d\theta$ and $d\varphi$, respectively.

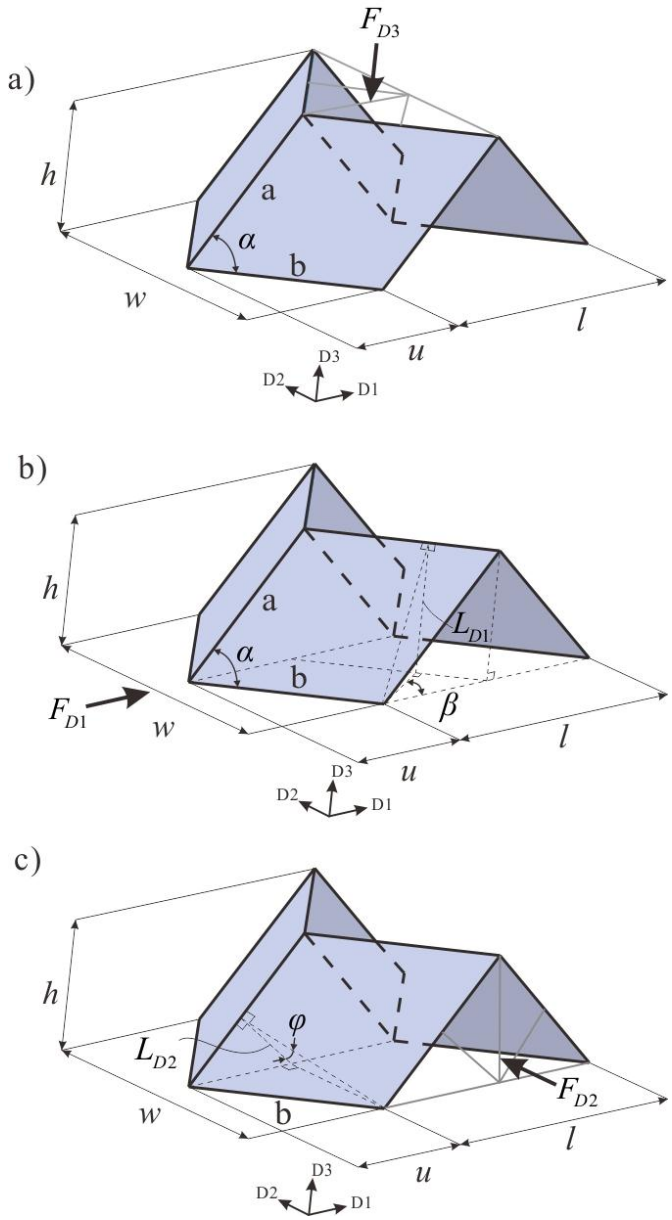

Fig. 5.17 Theoretical analysis: a) Out-of-plane compression, b) in-plane compression D1, c) in-plane compression D2.

Substituting (5.9) and (5.10) into (5.8) derives

$$F_{\mathrm{D3}} \cdot dh = \frac{2Ebt^2}{3n}\left[\left(\theta_0 - \theta_i\right)d\theta + \left(\varphi_i - \varphi_0\right)d\varphi\right]. \tag{5.11}$$

Due to the relationships in Eqns. (5.1) and (5.5), the relationship in (5.11) is a function of θ, i.e.

$$F_{\mathrm{D3}}\frac{\partial h}{\partial \theta}d\theta=\frac{2Ebt^2}{3n}\left[\left(\theta_0-\theta_i\right)d\theta+\left(\varphi_i-\varphi_0\right)\frac{\partial \varphi}{\partial \theta}d\theta\right]. \tag{5.12}$$

Thus, the reaction force of a unit in D3 is obtained as

$$F_{\mathrm{D3}}=\frac{2Ebt^2}{3n}\left[\theta_0-\theta_i+\left(\varphi_i-\varphi_0\right)\frac{\partial \varphi}{\partial \theta}\right]\Big/\frac{\partial h}{\partial \theta}. \tag{5.13}$$

Considering the tessellation of the patterned sheet, the reaction force in D3 of the sheet is 33 times that of F_{D3}. Fig. 5.18 a) plots the force and displacement curve from Eqn. (5.13). After the comparison with the experimental result of the out-of-plane compression, the width of the hinge at $n=0.5$ agrees with the experimental result reasonably and is subsequently used.

5.6.2 In-plane compressions

Similar to the out-of-plane compression, a unit under the in-plane compression D1 generates the reaction force as

$$F_{\mathrm{D1}}=\frac{2Ebt^2}{3n}\left[\theta_i-\theta_0+\left(\varphi_0-\varphi_i\right)\frac{\partial \varphi}{\partial \theta}\right]\Big/\frac{\partial l}{\partial \theta}. \tag{5.14}$$

also in the in-plane compression D2,

$$F_{\mathrm{D2}}=\frac{2Ebt^2}{3n}\left[\theta_i-\theta_0+\left(\varphi_0-\varphi_i\right)\frac{\partial \varphi}{\partial \theta}\right]\Big/\frac{\partial w}{\partial \theta}. \tag{5.15}$$

However, according to the deformation patterns shown in Fig. 5.13, the significant bending of the facets causes further contractions of the units in D1 direction under in-plane D1 compression, which is also the case in the D2 direction of the units under in-plane D2 compression. The displacements generated by bending of the facets can be represented by the concept of a

cantilever beam with an end load, thus the deflection d can be calculated using

$$d = \frac{FL^3}{3EI}, \tag{5.16}$$

so in the case of in-plane compressions, the cantilever beam deform under the loads equal to F_{D1} and F_{D2}, respectively. The additional displacements in a unit, l' in D1 and w' in D2, are calculated according to (5.16) as

$$l' = 2\left(\frac{F_{D1}}{2}\cos\beta\right)\frac{L_{D1}{}^3}{3EI}\cos\beta, \tag{5.17}$$

and

$$w' = 2\left(\frac{F_{D2}}{2}\right)\frac{L_{D2}^3}{3EI}, \tag{5.18}$$

in which L_{D1}, L_{D2} and β is defined in Fig. 5.17 b) and c). The following relationships,

$$L_{D1} = h, \quad \cos\beta = \frac{w}{2b}, \quad L_{D2} = b\sin\alpha\cos\varphi, \tag{5.19}$$

are substituted into (5.17) and (5.18), and the following relationships are derived,

$$l' = \frac{F_{D1}w^2h^3}{12b^2EI}, \tag{5.20}$$

and

$$w' = \frac{F_{D2}b^3\sin^3\gamma\cos^3\varphi}{3EI}. \tag{5.21}$$

Thus, the displacements of the patterned sheet under in-plane D1 and D2 compressions are calculated as

$$D_{D1} = 5.5\left(l_0 - l_i + l'\right), \quad D_{D2} = 6\left(w_0 - w_i + w'\right), \tag{5.22}$$

which ignores the change of length u in D1 direction.

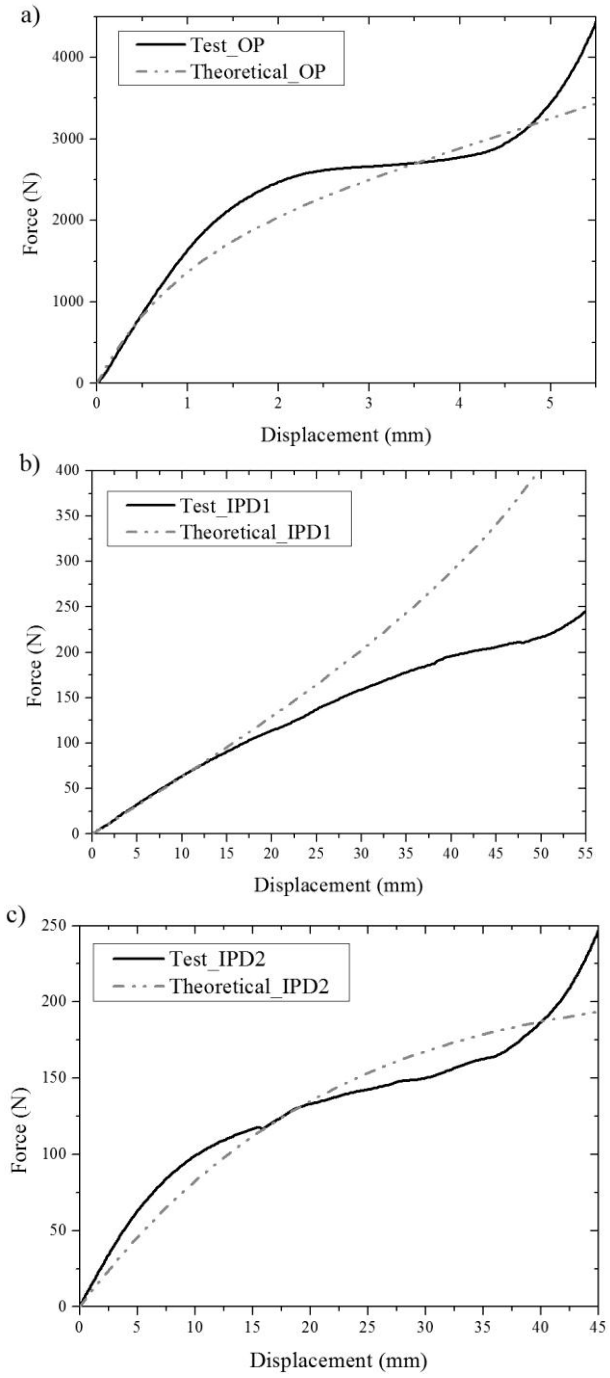

Fig. 5.18 Theoretical curves: a) Out-of-plane compression b) in-plane compression D1, and c) D2.

Due to the tessellation of the patterned sheet, the reaction forces of the sheet are 33 times those of F_{D1} and F_{D2} in respective cases. The curves of the force against displacement of the in-plane compressions are plotted in Fig. 5.18, which display good correlation with the experimental results in the in-plane D2 compression and comparable trend in the in-plane D1 compression.

5.7 Summary

The Miura-ori patterned sheet has been made from the commercialised material copolymer Elvaloy by compression moulding and its deformation behaviours have been investigated experimentally and using finite element analysis. The validation of the FE model has been completed in ABAQUS/Explicit. The simulations have been carried out on the Miura-ori patterned sheet under a series of loading situations corresponding to the tests. The simulation results have been compared with the mechanical tests, which show good consistency. Based on the simulation results, the deformations of the patterned sheet, the energy absorption and the parallel parameter studies have been investigated. A theoretical analysis has been carried out in the out-of-plane and in-plane compressions. The theoretical results correlate well with the experimental results in the out-of-plane and in-plane D2 cases, and show comparable trend in the in-plane D1 compression.

Chapter 6

Conclusions and Future Work

6.1 Contributions

In this thesis, we present our work on the kinematic modelling of the deployable structures, mechanical behaviour and mechanics of the patterned sheets. The main contributions are summarised here, followed by suggestions of future work.

6.1.1 Deployable surface

A kinematic model of the deployable surfaces has been proposed based on the adjacent assembly of four spherical 4*R* linkages. The model has managed to represent all the deployable surfaces with one degree of freedom and consisting of rigid planar quadrilaterals and degree-4 vertices.

To ensure the assemblies of spherical 4*R* linkages with one degree of freedom, the kinematic compatibility conditions of the model have been derived. The solutions thus cover the existing types of deployable surfaces, as well as twelve novel types. In total, eighteen types of mobile assemblies have been obtained with explicit geometric relationships. Based on the solutions, the discussions have been presented on the relationships between kinematic variables, hybrid assemblies, and networks of unlimited linkages. New rigid origami patterns for flat surfaces have been derived for their potential usage in the engineering applications.

6.1.2 Deployable prismatic structure

To investigate the deployable prismatic structure, which is one-DOF mobile and constituted by rigid planar quadrilaterals and degree-4 vertices, the

opposite assembly of the spherical 4*R* linkages has been constructed to form a closed chain. The kinematic compatibility conditions of the assembly have been derived and subsequently solved. There are two groups of 2*n*-sided prismatic structures: one with a rotational symmetry and the other with a planar symmetry. The folding processes of both groups have been presented. Based on manipulating the independent parameters, such as the side and ridgeline lengths and the values of the twist and dihedral angles, the unit variations have been discussed and presented. Multi-layer deployable prismatic structures have been constructed based on the unit variations. The straight and curvy multi-layer tubes have been constructed depending on the configuration of the dihedral angles between the intersecting planes. The general design method for the 2*n*-sided multi-layer deployable prismatic structures have been discussed with the geometric condition of the origami patterns, which guarantees that all of the proposed deployable structures can be deployed and folded along the central axis of the prismatic structures with a single degree of freedom.

The multi-layer structure can offer an extremely large deployable ratio when compact folding is achieved. Furthermore, the rigid origami pattern ensures that there is no deformation on the quadrilateral panels, which means repeated deployment and folding are easily realised. With all these characteristics, such deployable structures are expected to have a wide range of engineering applications.

6.1.3 Patterned sheet

The Miura-ori patterned sheet has been made from a commercialized material copolymer Elvaloy by compression moulding and its deformation behaviour has been investigated experimentally as well as with finite element analysis.

The intrinsic mechanical properties of Elvaloy have been obtained through tensile and four-point-bending tests, which are then used in the FE simulation. The newly introduced in-plane compression tests along with three-point bending tests have been performed. After each tests, the

patterned sheet specimen sprang back with trivial changes of its original dimensions. Thus, the repeated usage of the patterned sheet is possible. Its light weight, commercialized material, simple manufacture process and repeat-use capability endow the Elvaloy patterned sheet with application potential as wearable equipment, such as the cushion units in sports shoes and the safety gears for construction workers.

The validation of the FE model has been completed using ABAQUS/Explicit. The simulations have been carried out on the Miura-ori patterned sheet under a series of loading situations corresponding to the tests. The simulation results have been compared with the mechanical tests, which show good level of consistency. Based on the simulation results, the deformations of the patterned sheet under different load situation have been discussed. The energy absorption capacities of the patterned sheet have been investigated. To provide design instructions of the patterned sheet for a certain application, the parallel parameter studies on the thickness and the value of angle α have been carried out utilising the established FE model.

A theoretical analysis has been carried out in terms of the reaction force and displacement relationships in the out-of-plane and in-plane compressions, associated with the deformation patterns obtained in the FE simulations. The deformation in the out-of-plane compression has been modelled by the mechanism of rigid Miura-ori, and the force has been calculated by applying the principle of virtual work. In the in-plane compressions, the additional displacements generated by the significant bending of the facets have been simply modelled by the concept of a cantilever beam with an end load. The theoretical results correlate well with the experimental results in the out-of-plane and in-plane D2 cases, and show a comparable trend in the in-plane D1 compression.

6.2 Future work

A great deal of research can be engaged as a result of the work presented in this thesis, with the suggestions of possible avenues of future work listed as follows.

1. Despite of the complicity of the kinematic compatibility conditions of the assembly, more work can be done to discover the complete sets of the solutions for all possible mobile assemblies and the corresponding rigid origami patterns.

2. During the analysis of the spherical 4*R* linkage assembly for deployable prismatic structures, we never considered the condition that the sum of four twists around a single vertex is 2π, which is the general condition of an origami pattern that can be formed on a single piece of flat paper. Thus, more than one piece of paper and glue joining are required to construct deployable prismatic structures. New types of prismatic structures that can be fold from a single piece of flat paper could be developed in the future.

3. New types of deployable prismatic structures can be derived, such as odd-sided prismatic structures, which constitutes another field of further study within this topic.

4. Two different ways of assembling spherical 4*R* linkages have been used in this thesis to represent deployable surfaces and prismatic structures, which can be replaced by a generalised method that includes both.

5. Any future work could also focus on the manufacturing process of sandwich structures by adding upper and lower flat skins to the patterned sheet made of plastics, such as the Elvaloy, and then investigate its mechanical properties for repeat-use applications, such as the midsole of sports shoes.

6. The in-plane compressions in this thesis have only been carried out in directions D1 and D2 of the patterned sheet, but in order to further investigate the in-plane behaviour, the in-plane compressions in other directions, such as the direction 30 degree apart from D1 or the diagonal direction, can be performed.

7. To investigate the energy absorption of the patterned sheet under low/high speed impact loading, dynamic tests should be performed.

8. There have been numerous studies that have focused on the patterned sheet made of ridge materials. On the contrary, a wide range of soft or elastic materials have yet to be introduced to produce the patterned sheet. In addition, experimental and numerical analysis on other soft or elastic patterned sheets can also be studied as in any future work.

9. More work should be done on the theoretical analysis on the bending of the patterned sheet, associated with the existing numerical model that adds a fold in the short diagonal of each facet. To obtain the force-displacement curves in this thesis, we haven't considered the large deformations of the patterned sheet. The involvement of the large deformations, which will lead to a more accurate understanding of the mechanical behaviour, can serve as a challenging but rewarding avenue of future study.

10. We have only performed FE simulations to emulate the tests. Therefore, the FE simulations that focus on folding a flat sheet to the patterned sheet could be performed, which can be subsequently used to modify the flat pattern to be precisely fold into a desired shape.

Appendix A

A.1 Relationships between the inputs and outputs

In (3.16), functions f_{12}^{I}, f_{23}^{II}, $f_{34}^{-\mathrm{III}}$ and $f_{41}^{-\mathrm{IV}}$ are as follows.

$$\begin{aligned}&\cos\alpha_{23}^{\mathrm{I}}\sin\alpha_{41}^{\mathrm{I}}\sin\alpha_{12}^{\mathrm{I}}\cos\theta_{1}^{\mathrm{I}}+\cos\alpha_{41}^{\mathrm{I}}\sin\alpha_{12}^{\mathrm{I}}\sin\alpha_{23}^{\mathrm{I}}\cos\theta_{2}^{\mathrm{I}}\\&-\sin\alpha_{23}^{\mathrm{I}}\sin\alpha_{41}^{\mathrm{I}}\sin\theta_{1}^{\mathrm{I}}\sin\theta_{2}^{\mathrm{I}}+\cos\alpha_{12}^{\mathrm{I}}\sin\alpha_{23}^{\mathrm{I}}\sin\alpha_{41}^{\mathrm{I}}\cos\theta_{1}^{\mathrm{I}}\cos\theta_{2}^{\mathrm{I}}\\&+\cos\alpha_{34}^{\mathrm{I}}-\cos\alpha_{12}^{\mathrm{I}}\cos\alpha_{23}^{\mathrm{I}}\cos\alpha_{41}^{\mathrm{I}}=0,\end{aligned}\tag{A.1}$$

$$\begin{aligned}&\cos\alpha_{34}^{\mathrm{II}}\sin\alpha_{12}^{\mathrm{II}}\sin\alpha_{23}^{\mathrm{II}}\cos\theta_{2}^{\mathrm{II}}+\cos\alpha_{12}^{\mathrm{II}}\sin\alpha_{23}^{\mathrm{II}}\sin\alpha_{34}^{\mathrm{II}}\cos\theta_{3}^{\mathrm{II}}\\&-\sin\alpha_{12}^{\mathrm{II}}\sin\alpha_{34}^{\mathrm{II}}\sin\theta_{2}^{\mathrm{II}}\sin\theta_{3}^{\mathrm{II}}+\cos\alpha_{23}^{\mathrm{II}}\sin\alpha_{12}^{\mathrm{II}}\sin\alpha_{34}^{\mathrm{II}}\cos\theta_{2}^{\mathrm{II}}\cos\theta_{3}^{\mathrm{II}}\\&+\cos\alpha_{41}^{\mathrm{II}}-\cos\alpha_{12}^{\mathrm{II}}\cos\alpha_{23}^{\mathrm{II}}\cos\alpha_{34}^{\mathrm{II}}=0,\end{aligned}\tag{A.2}$$

$$\begin{aligned}&\cos\alpha_{41}^{\mathrm{III}}\sin\alpha_{23}^{\mathrm{III}}\sin\alpha_{34}^{\mathrm{III}}\cos\theta_{3}^{\mathrm{III}}+\cos\alpha_{23}^{\mathrm{III}}\sin\alpha_{34}^{\mathrm{III}}\sin\alpha_{41}^{\mathrm{III}}\cos\theta_{4}^{\mathrm{III}}\\&-\sin\alpha_{23}^{\mathrm{III}}\sin\alpha_{41}^{\mathrm{III}}\sin\theta_{3}^{\mathrm{III}}\sin\theta_{4}^{\mathrm{III}}+\cos\alpha_{34}^{\mathrm{III}}\sin\alpha_{23}^{\mathrm{III}}\sin\alpha_{41}^{\mathrm{III}}\cos\theta_{3}^{\mathrm{III}}\cos\theta_{4}^{\mathrm{III}}\\&+\cos\alpha_{12}^{\mathrm{III}}-\cos\alpha_{23}^{\mathrm{III}}\cos\alpha_{34}^{\mathrm{III}}\cos\alpha_{41}^{\mathrm{III}}=0,\end{aligned}\tag{A.3}$$

$$\begin{aligned}&\cos\alpha_{12}^{\mathrm{IV}}\sin\alpha_{34}^{\mathrm{IV}}\sin\alpha_{41}^{\mathrm{IV}}\cos\theta_{4}^{\mathrm{IV}}+\cos\alpha_{34}^{\mathrm{IV}}\sin\alpha_{41}^{\mathrm{IV}}\sin\alpha_{12}^{\mathrm{IV}}\cos\theta_{1}^{\mathrm{IV}}\\&-\sin\alpha_{12}^{\mathrm{IV}}\sin\alpha_{34}^{\mathrm{IV}}\sin\theta_{4}^{\mathrm{IV}}\sin\theta_{1}^{\mathrm{IV}}+\cos\alpha_{41}^{\mathrm{IV}}\sin\alpha_{12}^{\mathrm{IV}}\sin\alpha_{34}^{\mathrm{IV}}\cos\theta_{4}^{\mathrm{IV}}\cos\theta_{1}^{\mathrm{IV}}\\&+\cos\alpha_{23}^{\mathrm{IV}}-\cos\alpha_{12}^{\mathrm{IV}}\cos\alpha_{34}^{\mathrm{IV}}\cos\alpha_{41}^{\mathrm{IV}}=0.\end{aligned}\tag{A.4}$$

According to the trigonometry, the following relationships are obtained,

$$\sin\theta_{2}^{\mathrm{I}}=\frac{2\tan\dfrac{\theta_{2}^{\mathrm{I}}}{2}}{1+\tan^{2}\dfrac{\theta_{2}^{\mathrm{I}}}{2}}=\frac{2A}{1+A^{2}},\ \cos\theta_{2}^{\mathrm{I}}=\frac{1-\tan^{2}\dfrac{\theta_{2}^{\mathrm{I}}}{2}}{1+\tan^{2}\dfrac{\theta_{2}^{\mathrm{I}}}{2}}=\frac{1-A^{2}}{1+A^{2}},\tag{A.5}$$

and

$$\sin\theta_4^{\mathrm{III}} = \frac{2\tan\frac{\theta_4^{\mathrm{III}}}{2}}{1+\tan^2\frac{\theta_4^{\mathrm{III}}}{2}} = \frac{2A'}{1+A'^2},\ \cos\theta_4^{\mathrm{III}} = \frac{1-\tan^2\frac{\theta_4^{\mathrm{III}}}{2}}{1+\tan^2\frac{\theta_4^{\mathrm{III}}}{2}} = \frac{1-A'^2}{1+A'^2}, \tag{A.6}$$

in which $A = \tan\frac{\theta_2^{\mathrm{I}}}{2}$ and $A' = \tan\frac{\theta_4^{\mathrm{III}}}{2}$. Due to the relationships in (3.14), substituting Eqn. (A.5) into (A.1) and (A.2), and (A.6) into (A.3) and (A.4), the following equations are derived.

$$\begin{aligned} &A^2(\sin(\alpha_{12}^{\mathrm{I}}-\alpha_{23}^{\mathrm{I}})\sin\alpha_{41}^{\mathrm{I}}\cos\theta_1^{\mathrm{I}} - \cos(\alpha_{12}^{\mathrm{I}}-\alpha_{23}^{\mathrm{I}})\cos\alpha_{41}^{\mathrm{I}} + \cos\alpha_{34}^{\mathrm{I}}) \\ &-2A\sin\alpha_{23}^{\mathrm{I}}\sin\alpha_{41}^{\mathrm{I}}\sin\theta_1^{\mathrm{I}} \\ &+\sin(\alpha_{12}^{\mathrm{I}}+\alpha_{23}^{\mathrm{I}})\sin\alpha_{41}^{\mathrm{I}}\cos\theta_1^{\mathrm{I}} - \cos\alpha_{41}^{\mathrm{I}}\cos(\alpha_{12}^{\mathrm{I}}+\alpha_{23}^{\mathrm{I}}) + \cos\alpha_{34}^{\mathrm{I}} = 0, \end{aligned} \tag{A.7}$$

$$\begin{aligned} &A^2(\sin(\alpha_{23}^{\mathrm{II}}-\alpha_{12}^{\mathrm{II}})\sin\alpha_{34}^{\mathrm{II}}\cos\theta_3^{\mathrm{II}} - \cos\alpha_{34}^{\mathrm{II}}\cos(\alpha_{23}^{\mathrm{II}}-\alpha_{12}^{\mathrm{II}}) + \cos\alpha_{41}^{\mathrm{II}}) \\ &-2A\sin\alpha_{12}^{\mathrm{II}}\sin\alpha_{34}^{\mathrm{II}}\sin\theta_3^{\mathrm{II}} \\ &+\sin(\alpha_{23}^{\mathrm{II}}+\alpha_{12}^{\mathrm{II}})\sin\alpha_{34}^{\mathrm{II}}\cos\theta_3^{\mathrm{II}} - \cos(\alpha_{23}^{\mathrm{II}}+\alpha_{12}^{\mathrm{II}})\cos\alpha_{34}^{\mathrm{II}} + \cos\alpha_{41}^{\mathrm{II}} = 0, \end{aligned} \tag{A.8}$$

$$\begin{aligned} &A'^2(\sin(\alpha_{34}^{\mathrm{III}}-\alpha_{41}^{\mathrm{III}})\sin\alpha_{23}^{\mathrm{III}}\cos\theta_3^{\mathrm{III}} - \cos\alpha_{23}^{\mathrm{III}}\cos(\alpha_{34}^{\mathrm{III}}-\alpha_{41}^{\mathrm{III}}) + \cos\alpha_{12}^{\mathrm{III}}) \\ &-2A'\sin\alpha_{23}^{\mathrm{III}}\sin\alpha_{41}^{\mathrm{III}}\sin\theta_3^{\mathrm{III}} \\ &+\sin(\alpha_{34}^{\mathrm{III}}+\alpha_{41}^{\mathrm{III}})\sin\alpha_{23}^{\mathrm{III}}\cos\theta_3^{\mathrm{III}} - \cos\alpha_{23}^{\mathrm{III}}\cos(\alpha_{34}^{\mathrm{III}}+\alpha_{41}^{\mathrm{III}}) + \cos\alpha_{12}^{\mathrm{III}} = 0, \end{aligned} \tag{A.9}$$

$$\begin{aligned} &A'^2(\sin(\alpha_{41}^{\mathrm{IV}}-\alpha_{34}^{\mathrm{IV}})\sin\alpha_{12}^{\mathrm{IV}}\cos\theta_1^{\mathrm{IV}} - \cos\alpha_{12}^{\mathrm{IV}}\cos(\alpha_{41}^{\mathrm{IV}}-\alpha_{34}^{\mathrm{IV}}) + \cos\alpha_{23}^{\mathrm{IV}}) \\ &-2A'\sin\alpha_{12}^{\mathrm{IV}}\sin\alpha_{34}^{\mathrm{IV}}\sin\theta_1^{\mathrm{IV}} \\ &+\sin(\alpha_{41}^{\mathrm{IV}}+\alpha_{34}^{\mathrm{IV}})\sin\alpha_{12}^{\mathrm{IV}}\cos\theta_1^{\mathrm{IV}} - \cos\alpha_{12}^{\mathrm{IV}}\cos(\alpha_{41}^{\mathrm{IV}}+\alpha_{34}^{\mathrm{IV}}) + \cos\alpha_{23}^{\mathrm{IV}} = 0. \end{aligned} \tag{A.10}$$

By eliminating A^2 from (A.7) and (A.8), as well as A'^2 from (A.9) and (A.10), the following equations are derived.

$$
\begin{aligned}
&(\mathrm{s}(\alpha_{12}^{\mathrm{I}}+\alpha_{23}^{\mathrm{I}})\,\mathrm{s}\,\alpha_{41}^{\mathrm{I}}\,\mathrm{c}\,\theta_{1}^{\mathrm{I}}-\mathrm{c}(\alpha_{12}^{\mathrm{I}}+\alpha_{23}^{\mathrm{I}})\mathrm{c}\alpha_{41}^{\mathrm{I}}+\mathrm{c}\alpha_{34}^{\mathrm{I}})\\
&\cdot(\mathrm{s}(\alpha_{23}^{\mathrm{II}}-\alpha_{12}^{\mathrm{II}})\,\mathrm{s}\,\alpha_{34}^{\mathrm{II}}\,\mathrm{c}\,\theta_{3}^{\mathrm{II}}-\mathrm{c}(\alpha_{23}^{\mathrm{II}}-\alpha_{12}^{\mathrm{II}})\mathrm{c}\alpha_{34}^{\mathrm{II}}+\mathrm{c}\alpha_{41}^{\mathrm{II}})\\
&-(\mathrm{s}(\alpha_{23}^{\mathrm{II}}+\alpha_{12}^{\mathrm{II}})\,\mathrm{s}\,\alpha_{34}^{\mathrm{II}}\,\mathrm{c}\,\theta_{3}^{\mathrm{II}}-\mathrm{c}(\alpha_{23}^{\mathrm{II}}+\alpha_{12}^{\mathrm{II}})\,\mathrm{c}\,\alpha_{34}^{\mathrm{II}}+\mathrm{c}\alpha_{41}^{\mathrm{II}})\\
&\cdot(\mathrm{s}(\alpha_{12}^{\mathrm{I}}-\alpha_{23}^{\mathrm{I}})\,\mathrm{s}\,\alpha_{41}^{\mathrm{I}}\,\mathrm{c}\,\theta_{1}^{\mathrm{I}}-\mathrm{c}(\alpha_{12}^{\mathrm{I}}-\alpha_{23}^{\mathrm{I}})\,\mathrm{c}\,\alpha_{41}^{\mathrm{I}}+\mathrm{c}\alpha_{34}^{\mathrm{I}})\\
&=2A[\mathrm{s}\,\alpha_{23}^{\mathrm{I}}\,\mathrm{s}\,\alpha_{41}^{\mathrm{I}}\,\mathrm{s}\,\theta_{1}^{\mathrm{I}}(\mathrm{s}(\alpha_{23}^{\mathrm{II}}-\alpha_{12}^{\mathrm{II}})\,\mathrm{s}\,\alpha_{34}^{\mathrm{II}}\,\mathrm{c}\,\theta_{3}^{\mathrm{II}}-\mathrm{c}(\alpha_{23}^{\mathrm{II}}-\alpha_{12}^{\mathrm{II}})\mathrm{c}\alpha_{34}^{\mathrm{II}}+\mathrm{c}\alpha_{41}^{\mathrm{II}})\\
&-\mathrm{s}\,\alpha_{12}^{\mathrm{II}}\,\mathrm{s}\,\alpha_{34}^{\mathrm{II}}\,\mathrm{s}\,\theta_{3}^{\mathrm{II}}(\mathrm{s}(\alpha_{12}^{\mathrm{I}}-\alpha_{23}^{\mathrm{I}})\,\mathrm{s}\,\alpha_{41}^{\mathrm{I}}\,\mathrm{c}\,\theta_{1}^{\mathrm{I}}-\mathrm{c}(\alpha_{12}^{\mathrm{I}}-\alpha_{23}^{\mathrm{I}})\,\mathrm{c}\,\alpha_{41}^{\mathrm{I}}+\mathrm{c}\alpha_{34}^{\mathrm{I}})],
\end{aligned}
\tag{A.11}
$$

$$
\begin{aligned}
&(\mathrm{s}(\alpha_{34}^{\mathrm{III}}+\alpha_{41}^{\mathrm{III}})\,\mathrm{s}\,\alpha_{23}^{\mathrm{III}}\,\mathrm{c}\,\theta_{3}^{\mathrm{III}}-\mathrm{c}(\alpha_{34}^{\mathrm{III}}+\alpha_{41}^{\mathrm{III}})\mathrm{c}\alpha_{23}^{\mathrm{III}}+\mathrm{c}\alpha_{12}^{\mathrm{III}})\\
&\cdot(\mathrm{s}(\alpha_{41}^{\mathrm{IV}}-\alpha_{34}^{\mathrm{IV}})\,\mathrm{s}\,\alpha_{12}^{\mathrm{IV}}\,\mathrm{c}\,\theta_{1}^{\mathrm{IV}}-\mathrm{c}(\alpha_{41}^{\mathrm{IV}}-\alpha_{34}^{\mathrm{IV}})\mathrm{c}\alpha_{12}^{\mathrm{IV}}+\mathrm{c}\alpha_{23}^{\mathrm{IV}})\\
&-(\mathrm{s}(\alpha_{41}^{\mathrm{IV}}+\alpha_{34}^{\mathrm{IV}})\,\mathrm{s}\,\alpha_{12}^{\mathrm{IV}}\,\mathrm{c}\,\theta_{1}^{\mathrm{IV}}-\mathrm{c}(\alpha_{41}^{\mathrm{IV}}+\alpha_{34}^{\mathrm{IV}})\mathrm{c}\alpha_{12}^{\mathrm{IV}}+\mathrm{c}\alpha_{23}^{\mathrm{IV}})\\
&\cdot(\mathrm{s}(\alpha_{34}^{\mathrm{III}}-\alpha_{41}^{\mathrm{III}})\,\mathrm{s}\,\alpha_{23}^{\mathrm{III}}\,\mathrm{c}\,\theta_{3}^{\mathrm{III}}-\mathrm{c}(\alpha_{34}^{\mathrm{III}}-\alpha_{41}^{\mathrm{III}})\mathrm{c}\alpha_{23}^{\mathrm{III}}+\mathrm{c}\alpha_{12}^{\mathrm{III}})\\
&=2A'[\mathrm{s}\,\alpha_{23}^{\mathrm{III}}\,\mathrm{s}\,\alpha_{41}^{\mathrm{III}}\,\mathrm{s}\,\theta_{3}^{\mathrm{III}}(\mathrm{s}(\alpha_{41}^{\mathrm{IV}}-\alpha_{34}^{\mathrm{IV}})\,\mathrm{s}\,\alpha_{12}^{\mathrm{IV}}\,\mathrm{c}\,\theta_{1}^{\mathrm{IV}}-\mathrm{c}(\alpha_{41}^{\mathrm{IV}}-\alpha_{34}^{\mathrm{IV}})\mathrm{c}\alpha_{12}^{\mathrm{IV}}+\mathrm{c}\alpha_{23}^{\mathrm{IV}})\\
&-\mathrm{s}\,\alpha_{12}^{\mathrm{IV}}\,\mathrm{s}\,\alpha_{34}^{\mathrm{IV}}\,\mathrm{s}\,\theta_{1}^{\mathrm{IV}}(\mathrm{s}(\alpha_{34}^{\mathrm{III}}-\alpha_{41}^{\mathrm{III}})\,\mathrm{s}\,\alpha_{23}^{\mathrm{III}}\,\mathrm{c}\,\theta_{3}^{\mathrm{III}}-\mathrm{c}(\alpha_{34}^{\mathrm{III}}-\alpha_{41}^{\mathrm{III}})\mathrm{c}\alpha_{23}^{\mathrm{III}}+\mathrm{c}\alpha_{12}^{\mathrm{III}})].
\end{aligned}
\tag{A.12}
$$

From (A.11) and (A.12), A and A' can be obtained as

$$
A=\frac{A1A2-A3A4}{2(\mathrm{s}\,\alpha_{23}^{\mathrm{I}}\,\mathrm{s}\,\alpha_{41}^{\mathrm{I}}\,\mathrm{s}\,\theta_{1}^{\mathrm{I}}A2-\mathrm{s}\,\alpha_{12}^{\mathrm{II}}\,\mathrm{s}\,\alpha_{34}^{\mathrm{II}}\,\mathrm{s}\,\theta_{3}^{\mathrm{II}}A4)},
\tag{A.13}
$$

$$
A'=\frac{A'1A'2-A'3A'4}{2(\mathrm{s}\,\alpha_{23}^{\mathrm{III}}\,\mathrm{s}\,\alpha_{41}^{\mathrm{III}}\,\mathrm{s}\,\theta_{3}^{\mathrm{III}}A'2-\mathrm{s}\,\alpha_{12}^{\mathrm{IV}}\,\mathrm{s}\,\alpha_{34}^{\mathrm{IV}}\,\mathrm{s}\,\theta_{1}^{\mathrm{IV}}A'4)},
\tag{A.14}
$$

in which:

$$
\begin{aligned}
A1&=\mathrm{s}(\alpha_{12}^{\mathrm{I}}+\alpha_{23}^{\mathrm{I}})\,\mathrm{s}\,\alpha_{41}^{\mathrm{I}}\,\mathrm{c}\,\theta_{1}^{\mathrm{I}}-\mathrm{c}(\alpha_{12}^{\mathrm{I}}+\alpha_{23}^{\mathrm{I}})\mathrm{c}\alpha_{41}^{\mathrm{I}}+\mathrm{c}\alpha_{34}^{\mathrm{I}},\\
A2&=\mathrm{s}(\alpha_{23}^{\mathrm{II}}-\alpha_{12}^{\mathrm{II}})\,\mathrm{s}\,\alpha_{34}^{\mathrm{II}}\,\mathrm{c}\,\theta_{3}^{\mathrm{II}}-\mathrm{c}(\alpha_{23}^{\mathrm{II}}-\alpha_{12}^{\mathrm{II}})\mathrm{c}\alpha_{34}^{\mathrm{II}}+\mathrm{c}\alpha_{41}^{\mathrm{II}},\\
A3&=\mathrm{s}(\alpha_{23}^{\mathrm{II}}+\alpha_{12}^{\mathrm{II}})\,\mathrm{s}\,\alpha_{34}^{\mathrm{II}}\,\mathrm{c}\,\theta_{3}^{\mathrm{II}}-\mathrm{c}(\alpha_{23}^{\mathrm{II}}+\alpha_{12}^{\mathrm{II}})\,\mathrm{c}\,\alpha_{34}^{\mathrm{II}}+\mathrm{c}\alpha_{41}^{\mathrm{II}},\\
A4&=\mathrm{s}(\alpha_{12}^{\mathrm{I}}-\alpha_{23}^{\mathrm{I}})\,\mathrm{s}\,\alpha_{41}^{\mathrm{I}}\,\mathrm{c}\,\theta_{1}^{\mathrm{I}}-\mathrm{c}(\alpha_{12}^{\mathrm{I}}-\alpha_{23}^{\mathrm{I}})\,\mathrm{c}\,\alpha_{41}^{\mathrm{I}}+\mathrm{c}\alpha_{34}^{\mathrm{I}},\\
A'1&=\mathrm{s}(\alpha_{34}^{\mathrm{III}}+\alpha_{41}^{\mathrm{III}})\,\mathrm{s}\,\alpha_{23}^{\mathrm{III}}\,\mathrm{c}\,\theta_{3}^{\mathrm{III}}-\mathrm{c}(\alpha_{34}^{\mathrm{III}}+\alpha_{41}^{\mathrm{III}})\mathrm{c}\alpha_{23}^{\mathrm{III}}+\mathrm{c}\alpha_{12}^{\mathrm{III}},\\
A'2&=\mathrm{s}(\alpha_{41}^{\mathrm{IV}}-\alpha_{34}^{\mathrm{IV}})\,\mathrm{s}\,\alpha_{12}^{\mathrm{IV}}\,\mathrm{c}\,\theta_{1}^{\mathrm{IV}}-\mathrm{c}(\alpha_{41}^{\mathrm{IV}}-\alpha_{34}^{\mathrm{IV}})\mathrm{c}\alpha_{12}^{\mathrm{IV}}+\mathrm{c}\alpha_{23}^{\mathrm{IV}},\\
A'3&=\mathrm{s}(\alpha_{41}^{\mathrm{IV}}+\alpha_{34}^{\mathrm{IV}})\,\mathrm{s}\,\alpha_{12}^{\mathrm{IV}}\,\mathrm{c}\,\theta_{1}^{\mathrm{IV}}-\mathrm{c}(\alpha_{41}^{\mathrm{IV}}+\alpha_{34}^{\mathrm{IV}})\mathrm{c}\alpha_{12}^{\mathrm{IV}}+\mathrm{c}\alpha_{23}^{\mathrm{IV}},\\
A'4&=\mathrm{s}(\alpha_{34}^{\mathrm{III}}-\alpha_{41}^{\mathrm{III}})\,\mathrm{s}\,\alpha_{23}^{\mathrm{III}}\,\mathrm{c}\,\theta_{3}^{\mathrm{III}}-\mathrm{c}(\alpha_{34}^{\mathrm{III}}-\alpha_{41}^{\mathrm{III}})\mathrm{c}\alpha_{23}^{\mathrm{III}}+\mathrm{c}\alpha_{12}^{\mathrm{III}}.
\end{aligned}
$$

Substituting (A.13) into (A.7), and (A.14) into (A.10), gives the following equations.

$$(A1A2 - A3A4)^2$$
$$+4(\mathrm{s}\alpha_{23}^{\mathrm{I}}\,\mathrm{s}\alpha_{41}^{\mathrm{I}}\,\mathrm{s}\theta_1^{\mathrm{I}}A2 - \mathrm{s}\alpha_{12}^{\mathrm{II}}\,\mathrm{s}\alpha_{34}^{\mathrm{II}}\,\mathrm{s}\theta_3^{\mathrm{II}}A4)(\mathrm{s}\alpha_{23}^{\mathrm{I}}\,\mathrm{s}\alpha_{41}^{\mathrm{I}}\,\mathrm{s}\theta_1^{\mathrm{I}}A3 - \mathrm{s}\alpha_{12}^{\mathrm{II}}\,\mathrm{s}\alpha_{34}^{\mathrm{II}}\,\mathrm{s}\theta_3^{\mathrm{II}}A1) = 0, \quad \text{(A.15)}$$

$$(A'1A'2 - A'3A'4)^2$$
$$+4(\mathrm{s}\alpha_{23}^{\mathrm{III}}\,\mathrm{s}\alpha_{41}^{\mathrm{III}}\,\mathrm{s}\theta_3^{\mathrm{III}}A'2 - \mathrm{s}\alpha_{12}^{\mathrm{IV}}\,\mathrm{s}\alpha_{34}^{\mathrm{IV}}\,\mathrm{s}\theta_1^{\mathrm{IV}}A'4)(\mathrm{s}\alpha_{23}^{\mathrm{III}}\,\mathrm{s}\alpha_{41}^{\mathrm{III}}\,\mathrm{s}\theta_3^{\mathrm{III}}A'3 - \mathrm{s}\alpha_{12}^{\mathrm{IV}}\,\mathrm{s}\alpha_{34}^{\mathrm{IV}}\,\mathrm{s}\theta_1^{\mathrm{IV}}A'1) = 0. \quad \text{(A.16)}$$

Eqn. (A.15) represents the relationship between θ_1^{I} and θ_3^{II}, i.e. $\theta_3^{\mathrm{II}} = f_{23}^{\mathrm{II}}(f_{12}^{\mathrm{I}}(\theta_1^{\mathrm{I}}))$. Eqn. (A.16) represents the relationship between θ_1^{IV} and θ_3^{III}, i.e. $\theta_3^{\mathrm{III}} = f_{34}^{-\mathrm{III}}(f_{41}^{-\mathrm{IV}}(\theta_1^{\mathrm{IV}}))$.

Appendix B

Table B.1 All the solutions of the mobile assemblies

Group	Name	Assumptions	Shared features	Relationships of θ_1^{I} and θ_3^{II}	Shape of central facet	Explicit relationships	Features
One	Identical linkage (ID1)	$\theta_i^{\mathrm{I}} = \theta_i^{\mathrm{II}}$, $\theta_i^{\mathrm{III}} = \theta_i^{\mathrm{IV}}$.	Linkage I and II are identical; linkage III and IV are identical; $\alpha_{i(i+1)}^{\mathrm{I}} = \alpha_{i(i+1)}^{\mathrm{II}}$, $\alpha_{i(i+1)}^{\mathrm{III}} = \alpha_{i(i+1)}^{\mathrm{IV}}$.	$\mathrm{s}\alpha_{23}^{\mathrm{I}}\,\mathrm{s}\alpha_{34}^{\mathrm{I}}\,\mathrm{c}\theta_3^{\mathrm{II}} - \mathrm{c}\alpha_{23}^{\mathrm{I}}\,\mathrm{c}\alpha_{34}^{\mathrm{I}} = \mathrm{s}\alpha_{12}^{\mathrm{I}}\,\mathrm{s}\alpha_{41}^{\mathrm{I}}\,\mathrm{c}\theta_1^{\mathrm{I}} - \mathrm{c}\alpha_{12}^{\mathrm{I}}\mathrm{c}\alpha_{41}^{\mathrm{I}}$	Convex quadrilateral	$\alpha_{i(i+1)}^{\mathrm{I}} = \alpha_{i(i+1)}^{\mathrm{II}} = \alpha_{i(i+1)}^{\mathrm{III}} = \alpha_{i(i+1)}^{\mathrm{IV}}$.	All linkages are identical,
	ID2					$\alpha_{i(i+1)}^{\mathrm{I}} = \alpha_{i(i+1)}^{\mathrm{II}} = \pi - \alpha_{i(i+1)}^{\mathrm{III}} = \pi - \alpha_{i(i+1)}^{\mathrm{IV}}$.	Linkages I and II are supplementary of linkages III and IV, but different from the supplementary type.
	ID3			$\theta_1^{\mathrm{I}} = \theta_3^{\mathrm{II}}$	Convex quadrilateral with $\alpha_{12}^{\mathrm{I}} = \alpha_{23}^{\mathrm{II}}$	$\alpha_{12}^{\mathrm{I}} = \alpha_{23}^{\mathrm{I}} = \alpha_{12}^{\mathrm{II}} = \alpha_{23}^{\mathrm{II}}$; $\alpha_{34}^{\mathrm{I}} = \alpha_{41}^{\mathrm{I}} = \alpha_{34}^{\mathrm{II}} = \alpha_{41}^{\mathrm{II}}$; $\alpha_{12}^{\mathrm{III}} = \alpha_{34}^{\mathrm{III}} = \alpha_{12}^{\mathrm{IV}} = \alpha_{34}^{\mathrm{IV}}$; $\alpha_{23}^{\mathrm{III}} = \alpha_{41}^{\mathrm{III}} = \alpha_{23}^{\mathrm{IV}} = \alpha_{41}^{\mathrm{IV}}$.	In I and II, adjacent angles are equal, in III and IV, opposite angles are equal.
	ID4					$\alpha_{12}^{\mathrm{I}} = \alpha_{23}^{\mathrm{I}} = \alpha_{12}^{\mathrm{II}} = \alpha_{23}^{\mathrm{II}}$; $\alpha_{34}^{\mathrm{I}} = \alpha_{41}^{\mathrm{I}} = \alpha_{34}^{\mathrm{II}} = \alpha_{41}^{\mathrm{II}}$; $\alpha_{12}^{\mathrm{III}} = \pi - \alpha_{34}^{\mathrm{III}} = \alpha_{12}^{\mathrm{IV}} = \pi - \alpha_{34}^{\mathrm{IV}}$; $\alpha_{23}^{\mathrm{III}} = \pi - \alpha_{41}^{\mathrm{III}} = \alpha_{23}^{\mathrm{IV}} = \pi - \alpha_{41}^{\mathrm{IV}}$.	In I and II, adjacent angles are equal, in III and IV, opposite angles are supplementary.
	ID5				Convex quadrilateral	$\alpha_{12}^{\mathrm{I}} = \alpha_{34}^{\mathrm{I}} = \alpha_{12}^{\mathrm{II}} = \alpha_{34}^{\mathrm{II}}$, $\alpha_{23}^{\mathrm{I}} = \alpha_{41}^{\mathrm{I}} = \alpha_{23}^{\mathrm{II}} = \alpha_{41}^{\mathrm{II}}$, $\alpha_{12}^{\mathrm{III}} = \alpha_{34}^{\mathrm{III}} = \alpha_{12}^{\mathrm{IV}} = \alpha_{34}^{\mathrm{IV}}$, $\alpha_{23}^{\mathrm{III}} = \alpha_{41}^{\mathrm{III}} = \alpha_{23}^{\mathrm{IV}} = \alpha_{41}^{\mathrm{IV}}$.	The opposite angles in every linkage are equal.
	ID6					$\alpha_{12}^{\mathrm{I}} = \alpha_{34}^{\mathrm{I}} = \alpha_{12}^{\mathrm{II}} = \alpha_{34}^{\mathrm{II}}$, $\alpha_{23}^{\mathrm{I}} = \alpha_{41}^{\mathrm{I}} = \alpha_{23}^{\mathrm{II}} = \alpha_{41}^{\mathrm{II}}$,	In I and II, opposite angles equal. In III and IV, opposite angles are supplementary.

						$\alpha_{12}^{\mathrm{III}}=\pi-\alpha_{34}^{\mathrm{III}}=\alpha_{12}^{\mathrm{IV}}=\pi-\alpha_{34}^{\mathrm{IV}}$, $\alpha_{23}^{\mathrm{III}}=\pi-\alpha_{41}^{\mathrm{III}}=\alpha_{23}^{\mathrm{IV}}=\pi-\alpha_{41}^{\mathrm{IV}}$.	
	ID7			$\theta_1^{\mathrm{I}}+\theta_3^{\mathrm{II}}=2\pi$		$\alpha_{12}^{\mathrm{I}}=\pi-\alpha_{34}^{\mathrm{I}}=\alpha_{12}^{\mathrm{II}}=\pi-\alpha_{34}^{\mathrm{II}}$, $\alpha_{23}^{\mathrm{I}}=\pi-\alpha_{41}^{\mathrm{I}}=\alpha_{23}^{\mathrm{II}}=\pi-\alpha_{41}^{\mathrm{II}}$, $\alpha_{12}^{\mathrm{III}}=\pi-\alpha_{34}^{\mathrm{III}}=\alpha_{12}^{\mathrm{IV}}=\pi-\alpha_{34}^{\mathrm{IV}}$, $\alpha_{23}^{\mathrm{III}}=\pi-\alpha_{41}^{\mathrm{III}}=\alpha_{23}^{\mathrm{IV}}=\pi-\alpha_{41}^{\mathrm{IV}}$.	Opposite angles in every linkage are supplementary.
	ID8			$\theta_1^{\mathrm{I}}+\theta_3^{\mathrm{II}}=\pi$		$\alpha_{12}^{\mathrm{I}}=2\pi-\alpha_{34}^{\mathrm{I}}=\alpha_{12}^{\mathrm{II}}=2\pi-\alpha_{34}^{\mathrm{II}}$, $\alpha_{23}^{\mathrm{I}}=\alpha_{41}^{\mathrm{I}}=\alpha_{23}^{\mathrm{II}}=\alpha_{41}^{\mathrm{II}}$, $\alpha_{12}^{\mathrm{III}}=2\pi-\alpha_{34}^{\mathrm{III}}=\alpha_{12}^{\mathrm{IV}}=2\pi-\alpha_{34}^{\mathrm{IV}}$, $\alpha_{23}^{\mathrm{III}}=\alpha_{41}^{\mathrm{III}}=\alpha_{23}^{\mathrm{IV}}=\alpha_{41}^{\mathrm{IV}}$.	Four angles are larger than π.
Two	Orthogonal	$A1A2=A3A4$, $A'1A'2=A'3A'4$	Axes IV3, IV1, I1 and I3 coplanar, also III1, III3, II3 and II1 coplanar.		Equilateral trapezoid	$\alpha_{12}^{\mathrm{I}}+\alpha_{23}^{\mathrm{II}}=\pi$, $\alpha_{23}^{\mathrm{I}}+\alpha_{12}^{\mathrm{II}}=\pi$, $\alpha_{34}^{\mathrm{III}}+\alpha_{41}^{\mathrm{IV}}=\pi$, $\alpha_{41}^{\mathrm{III}}+\alpha_{34}^{\mathrm{IV}}=\pi$, $\cos\alpha_{12}^{j}\cos\alpha_{34}^{j}=\cos\alpha_{23}^{j}\cos\alpha_{41}^{j}$, $\alpha_{12}^{\mathrm{I}}=\alpha_{41}^{\mathrm{IV}}$, $\alpha_{41}^{\mathrm{I}}=\alpha_{12}^{\mathrm{IV}}$, $\alpha_{23}^{\mathrm{II}}=\alpha_{34}^{\mathrm{III}}$, $\alpha_{34}^{\mathrm{II}}=\alpha_{23}^{\mathrm{III}}$.	The network is assembled by equilateral trapezoids
	Miura-ori variation				Parallelogram	$\alpha_{12}^{\mathrm{I}}+\alpha_{23}^{\mathrm{II}}=\pi$, $\alpha_{23}^{\mathrm{I}}+\alpha_{12}^{\mathrm{II}}=\pi$, $\alpha_{34}^{\mathrm{III}}+\alpha_{41}^{\mathrm{IV}}=\pi$, $\alpha_{41}^{\mathrm{III}}+\alpha_{34}^{\mathrm{IV}}=\pi$, $\cos\alpha_{12}^{j}\cos\alpha_{34}^{j}=\cos\alpha_{23}^{j}\cos\alpha_{41}^{j}$, $\alpha_{12}^{\mathrm{I}}+\alpha_{41}^{\mathrm{IV}}=\pi$, $\alpha_{41}^{\mathrm{I}}+\alpha_{12}^{\mathrm{IV}}=\pi$, $\alpha_{23}^{\mathrm{II}}+\alpha_{34}^{\mathrm{III}}=\pi$, $\alpha_{34}^{\mathrm{II}}+\alpha_{23}^{\mathrm{III}}=\pi$.	The network is assembled by parallelograms
Three	Planar-symmetric	$A1=A3$, $A2=A4$, $A'1=A'3$, $A'2=A'4$.	Linkage I and II are related; linkages III and IV are related; center facet has parallel edges	$\theta_1^{\mathrm{I}}=\theta_3^{\mathrm{II}}$	Equilateral trapezoid	$\alpha_{12}^{\mathrm{I}}=\alpha_{23}^{\mathrm{II}}$, $\alpha_{12}^{\mathrm{III}}=\alpha_{23}^{\mathrm{IV}}$, $\alpha_{23}^{\mathrm{I}}=\alpha_{12}^{\mathrm{II}}$, $\alpha_{23}^{\mathrm{III}}=\alpha_{12}^{\mathrm{IV}}$, $\alpha_{34}^{\mathrm{I}}=\alpha_{41}^{\mathrm{II}}$, $\alpha_{34}^{\mathrm{III}}=\alpha_{41}^{\mathrm{IV}}$, $\alpha_{41}^{\mathrm{I}}=\alpha_{34}^{\mathrm{II}}$, $\alpha_{41}^{\mathrm{III}}=\alpha_{34}^{\mathrm{IV}}$.	Linkages I and II are symmetric, so as III and IV;

	Rotational symmetric		such as trapezoid or parallelogram			$\alpha_{12}^{\mathrm{I}}=\alpha_{23}^{\mathrm{II}}, \alpha_{12}^{\mathrm{III}}=\alpha_{23}^{\mathrm{IV}},$ $\alpha_{23}^{\mathrm{I}}=\alpha_{12}^{\mathrm{II}}+\pi, \alpha_{23}^{\mathrm{III}}=\alpha_{12}^{\mathrm{IV}}-\pi,$ $\alpha_{34}^{\mathrm{I}}=\alpha_{41}^{\mathrm{II}}, \alpha_{34}^{\mathrm{III}}=\alpha_{41}^{\mathrm{IV}},$ $\alpha_{41}^{\mathrm{I}}=\alpha_{34}^{\mathrm{II}}-\pi, \alpha_{41}^{\mathrm{III}}=\alpha_{34}^{\mathrm{IV}}+\pi.$	Four angles are larger than π. A variation of symmetric type,
	Translational			$\theta_1^{\mathrm{I}}+\theta_3^{\mathrm{II}}=\pi$	Trapezoid or parallelogram	$\alpha_{12}^{\mathrm{I}}+\alpha_{23}^{\mathrm{II}}=\pi, \alpha_{12}^{\mathrm{III}}=\alpha_{23}^{\mathrm{IV}},$ $\alpha_{23}^{\mathrm{I}}+\alpha_{12}^{\mathrm{II}}=\pi, \alpha_{23}^{\mathrm{III}}=\alpha_{12}^{\mathrm{IV}},$ $\alpha_{34}^{\mathrm{I}}=\alpha_{41}^{\mathrm{II}}, \alpha_{34}^{\mathrm{III}}+\alpha_{41}^{\mathrm{IV}}=\pi,$ $\alpha_{41}^{\mathrm{I}}=\alpha_{34}^{\mathrm{II}}, \alpha_{41}^{\mathrm{III}}+\alpha_{34}^{\mathrm{IV}}=\pi.$	Three panels of linkages I and II seems like being translated to the corresponding three panels of linkages III and IV
	Reverse supplementary			$\theta_1^{\mathrm{I}}+\theta_3^{\mathrm{II}}=2\pi$		$\alpha_{12}^{\mathrm{I}}+\alpha_{23}^{\mathrm{II}}=\pi, \alpha_{12}^{\mathrm{III}}=\alpha_{23}^{\mathrm{IV}},$ $\alpha_{23}^{\mathrm{I}}+\alpha_{12}^{\mathrm{II}}=2\pi, \alpha_{23}^{\mathrm{III}}+\alpha_{12}^{\mathrm{IV}}=\pi,$ $\alpha_{34}^{\mathrm{I}}=\alpha_{41}^{\mathrm{II}}, \alpha_{34}^{\mathrm{III}}+\alpha_{41}^{\mathrm{IV}}=\pi,$ $\alpha_{41}^{\mathrm{I}}+\alpha_{34}^{\mathrm{II}}=\pi, \alpha_{41}^{\mathrm{III}}+\alpha_{34}^{\mathrm{IV}}=2\pi.$	Two angles are larger than π. A variation of supplementary type
Four	Supplementary	$A1=-A3,$ $A2=-A4,$ $A'1=-A'3,$ $A'2=-A'4.$	Linkage I and II are related; linkages III and IV are related; center facet has parallel edges such as trapezoid or parallelogram	$\theta_1^{\mathrm{I}}+\theta_3^{\mathrm{II}}=2\pi$	Trapezoid or parallelogram	$\alpha_{12}^{\mathrm{I}}+\alpha_{23}^{\mathrm{II}}=\pi, \alpha_{12}^{\mathrm{III}}+\alpha_{23}^{\mathrm{IV}}=\pi,$ $\alpha_{23}^{\mathrm{I}}+\alpha_{12}^{\mathrm{II}}=\pi, \alpha_{23}^{\mathrm{III}}+\alpha_{12}^{\mathrm{IV}}=\pi,$ $\alpha_{34}^{\mathrm{I}}+\alpha_{41}^{\mathrm{II}}=\pi, \alpha_{34}^{\mathrm{III}}+\alpha_{41}^{\mathrm{IV}}=\pi,$ $\alpha_{41}^{\mathrm{I}}+\alpha_{34}^{\mathrm{II}}=\pi, \alpha_{41}^{\mathrm{III}}+\alpha_{34}^{\mathrm{IV}}=\pi.$	Angles in I are supplementary to the corresponding angles in II, so as in III and IV.
	Reverse translational			$\theta_1^{\mathrm{I}}+\theta_3^{\mathrm{II}}=\pi$		$\alpha_{12}^{\mathrm{I}}+\alpha_{23}^{\mathrm{II}}=\pi, \alpha_{12}^{\mathrm{III}}+\alpha_{23}^{\mathrm{IV}}=\pi,$ $\alpha_{23}^{\mathrm{I}}+\alpha_{12}^{\mathrm{II}}=\pi, \alpha_{23}^{\mathrm{III}}-\alpha_{12}^{\mathrm{IV}}=\pi,$ $\alpha_{34}^{\mathrm{I}}+\alpha_{41}^{\mathrm{II}}=\pi, \alpha_{34}^{\mathrm{III}}+\alpha_{41}^{\mathrm{IV}}=\pi,$ $\alpha_{41}^{\mathrm{I}}-\alpha_{34}^{\mathrm{II}}=-\pi, \alpha_{41}^{\mathrm{III}}+\alpha_{34}^{\mathrm{IV}}=\pi.$	Two angles are larger than π. A variation of translational type
	Reverse symmetric			$\theta_1^{\mathrm{I}}-\theta_3^{\mathrm{II}}=\pi$	Equilateral trapezoid	$\alpha_{12}^{\mathrm{I}}=\alpha_{23}^{\mathrm{II}}, \alpha_{12}^{\mathrm{III}}+\alpha_{23}^{\mathrm{IV}}=\pi,$ $\alpha_{23}^{\mathrm{I}}=\alpha_{12}^{\mathrm{II}}, \alpha_{23}^{\mathrm{III}}+\alpha_{12}^{\mathrm{IV}}=\pi,$ $\alpha_{34}^{\mathrm{I}}+\alpha_{41}^{\mathrm{II}}=\pi, \alpha_{34}^{\mathrm{III}}=\alpha_{41}^{\mathrm{IV}},$ $\alpha_{41}^{\mathrm{I}}+\alpha_{34}^{\mathrm{II}}=\pi, \alpha_{41}^{\mathrm{III}}=\alpha_{34}^{\mathrm{IV}}.$	A variation of symmetric type

Table B.2 Hybrid assemblies

Relationships of θ_1^{I} and θ_3^{II}	Hybrid assemblies	Explicit relationships	Central facet
$\theta_1^{\mathrm{I}} = \theta_3^{\mathrm{II}}$	Psym-RotSym	$\alpha_{12}^{\mathrm{I}} = \alpha_{23}^{\mathrm{II}}, \alpha_{12}^{\mathrm{III}} = \alpha_{23}^{\mathrm{IV}},$ $\alpha_{23}^{\mathrm{I}} = \alpha_{12}^{\mathrm{II}}, \alpha_{23}^{\mathrm{III}} = \alpha_{12}^{\mathrm{IV}} - \pi,$ $\alpha_{34}^{\mathrm{I}} = \alpha_{41}^{\mathrm{II}}, \alpha_{34}^{\mathrm{III}} = \alpha_{41}^{\mathrm{IV}},$ $\alpha_{41}^{\mathrm{I}} = \alpha_{34}^{\mathrm{II}}, \alpha_{41}^{\mathrm{III}} = \alpha_{34}^{\mathrm{IV}} + \pi.$	Equilateral trapezoid
	Psym-ID3	$\alpha_{12}^{\mathrm{I}} = \alpha_{23}^{\mathrm{II}}, \alpha_{23}^{\mathrm{I}} = \alpha_{12}^{\mathrm{II}},$ $\alpha_{34}^{\mathrm{I}} = \alpha_{41}^{\mathrm{II}}, \alpha_{41}^{\mathrm{I}} = \alpha_{34}^{\mathrm{II}},$ $\alpha_{12}^{\mathrm{III}} = \alpha_{34}^{\mathrm{III}} = \alpha_{12}^{\mathrm{IV}} = \alpha_{34}^{\mathrm{IV}},$ $\alpha_{23}^{\mathrm{III}} = \alpha_{41}^{\mathrm{III}} = \alpha_{23}^{\mathrm{IV}} = \alpha_{41}^{\mathrm{IV}}.$	Convex quadrilateral
	Psym-ID4	$\alpha_{12}^{\mathrm{I}} = \alpha_{23}^{\mathrm{II}}, \alpha_{23}^{\mathrm{I}} = \alpha_{12}^{\mathrm{II}},$ $\alpha_{34}^{\mathrm{I}} = \alpha_{41}^{\mathrm{II}}, \alpha_{41}^{\mathrm{I}} = \alpha_{34}^{\mathrm{II}},$ $\alpha_{12}^{\mathrm{III}} = \pi - \alpha_{34}^{\mathrm{III}} = \alpha_{12}^{\mathrm{IV}} = \pi - \alpha_{34}^{\mathrm{IV}},$ $\alpha_{23}^{\mathrm{III}} = \pi - \alpha_{41}^{\mathrm{III}} = \alpha_{23}^{\mathrm{IV}} = \pi - \alpha_{41}^{\mathrm{IV}}.$	Convex quadrilateral
	RotSym-ID3	$\alpha_{12}^{\mathrm{I}} = \alpha_{23}^{\mathrm{II}}, \alpha_{23}^{\mathrm{I}} = \alpha_{12}^{\mathrm{II}} + \pi,$ $\alpha_{34}^{\mathrm{I}} = \alpha_{41}^{\mathrm{II}}, \alpha_{41}^{\mathrm{I}} = \alpha_{34}^{\mathrm{II}} - \pi.$ $\alpha_{12}^{\mathrm{III}} = \alpha_{34}^{\mathrm{III}} = \alpha_{12}^{\mathrm{IV}} = \alpha_{34}^{\mathrm{IV}},$ $\alpha_{23}^{\mathrm{III}} = \alpha_{41}^{\mathrm{III}} = \alpha_{23}^{\mathrm{IV}} = \alpha_{41}^{\mathrm{IV}}.$	Convex quadrilateral
	RotSym-ID4	$\alpha_{12}^{\mathrm{I}} = \alpha_{23}^{\mathrm{II}}, \alpha_{23}^{\mathrm{I}} = \alpha_{12}^{\mathrm{II}} + \pi,$ $\alpha_{34}^{\mathrm{I}} = \alpha_{41}^{\mathrm{II}}, \alpha_{41}^{\mathrm{I}} = \alpha_{34}^{\mathrm{II}} - \pi.$ $\alpha_{12}^{\mathrm{III}} = \pi - \alpha_{34}^{\mathrm{III}} = \alpha_{12}^{\mathrm{IV}} = \pi - \alpha_{34}^{\mathrm{IV}},$ $\alpha_{23}^{\mathrm{III}} = \pi - \alpha_{41}^{\mathrm{III}} = \alpha_{23}^{\mathrm{IV}} = \pi - \alpha_{41}^{\mathrm{IV}}.$	Convex quadrilateral
$\theta_1^{\mathrm{I}} + \theta_3^{\mathrm{II}} = \pi$	Tran-RevTran	$\alpha_{12}^{\mathrm{I}} + \alpha_{23}^{\mathrm{II}} = \pi, \alpha_{12}^{\mathrm{III}} + \alpha_{23}^{\mathrm{IV}} = \pi,$ $\alpha_{23}^{\mathrm{I}} + \alpha_{12}^{\mathrm{II}} = \pi, \alpha_{23}^{\mathrm{III}} - \alpha_{12}^{\mathrm{IV}} = \pi,$ $\alpha_{34}^{\mathrm{I}} = \alpha_{41}^{\mathrm{II}}, \alpha_{34}^{\mathrm{III}} + \alpha_{41}^{\mathrm{IV}} = \pi,$ $\alpha_{41}^{\mathrm{I}} = \alpha_{34}^{\mathrm{II}}, \alpha_{41}^{\mathrm{III}} + \alpha_{34}^{\mathrm{IV}} = \pi.$	Trapezoid
	ID8-Tran	$\alpha_{12}^{\mathrm{I}} = 2\pi - \alpha_{34}^{\mathrm{I}} = \alpha_{12}^{\mathrm{II}} = 2\pi - \alpha_{34}^{\mathrm{II}},$ $\alpha_{23}^{\mathrm{I}} = \alpha_{41}^{\mathrm{I}} = \alpha_{23}^{\mathrm{II}} = \alpha_{41}^{\mathrm{II}},$ $\alpha_{12}^{\mathrm{III}} = \alpha_{23}^{\mathrm{IV}}, \alpha_{23}^{\mathrm{III}} = \alpha_{12}^{\mathrm{IV}},$ $\alpha_{34}^{\mathrm{III}} + \alpha_{41}^{\mathrm{IV}} = \pi, \alpha_{41}^{\mathrm{III}} + \alpha_{34}^{\mathrm{IV}} = \pi.$	Trapezoid
	ID8-RevTran	$\alpha_{12}^{\mathrm{I}} = 2\pi - \alpha_{34}^{\mathrm{I}} = \alpha_{12}^{\mathrm{II}} = 2\pi - \alpha_{34}^{\mathrm{II}},$ $\alpha_{23}^{\mathrm{I}} = \alpha_{41}^{\mathrm{I}} = \alpha_{23}^{\mathrm{II}} = \alpha_{41}^{\mathrm{II}},$ $\alpha_{12}^{\mathrm{III}} + \alpha_{23}^{\mathrm{IV}} = \pi, \alpha_{23}^{\mathrm{III}} - \alpha_{12}^{\mathrm{IV}} = \pi,$ $\alpha_{34}^{\mathrm{III}} + \alpha_{41}^{\mathrm{IV}} = \pi, \alpha_{41}^{\mathrm{III}} + \alpha_{34}^{\mathrm{IV}} = \pi$	Trapezoid

$\theta_1^{\mathrm{I}}+\theta_3^{\mathrm{II}}=2\pi$	Sup-RevSup	$\alpha_{12}^{\mathrm{I}}+\alpha_{23}^{\mathrm{II}}=\pi,\ \alpha_{12}^{\mathrm{III}}+\alpha_{23}^{\mathrm{IV}}=\pi,$ $\alpha_{23}^{\mathrm{I}}+\alpha_{12}^{\mathrm{II}}=2\pi,\ \alpha_{23}^{\mathrm{III}}+\alpha_{12}^{\mathrm{IV}}=\pi,$ $\alpha_{34}^{\mathrm{I}}=\alpha_{41}^{\mathrm{II}},\ \alpha_{34}^{\mathrm{III}}+\alpha_{41}^{\mathrm{IV}}=\pi,$ $\alpha_{41}^{\mathrm{I}}+\alpha_{34}^{\mathrm{II}}=\pi,\ \alpha_{41}^{\mathrm{III}}+\alpha_{34}^{\mathrm{IV}}=\pi.$	Trapezoid
	ID7-Sup	$\alpha_{12}^{\mathrm{I}}=\pi-\alpha_{34}^{\mathrm{I}}=\alpha_{12}^{\mathrm{II}}=\pi-\alpha_{34}^{\mathrm{II}},$ $\alpha_{23}^{\mathrm{I}}=\pi-\alpha_{41}^{\mathrm{I}}=\alpha_{23}^{\mathrm{II}}=\pi-\alpha_{41}^{\mathrm{II}},$ $\alpha_{12}^{\mathrm{III}}+\alpha_{23}^{\mathrm{IV}}=\pi,\alpha_{23}^{\mathrm{III}}+\alpha_{12}^{\mathrm{IV}}=\pi,$ $\alpha_{34}^{\mathrm{III}}+\alpha_{41}^{\mathrm{IV}}=\pi,\alpha_{41}^{\mathrm{III}}+\alpha_{34}^{\mathrm{IV}}=\pi.$	Trapezoid
	ID7-RevSup	$\alpha_{12}^{\mathrm{I}}=\pi-\alpha_{34}^{\mathrm{I}}=\alpha_{12}^{\mathrm{II}}=\pi-\alpha_{34}^{\mathrm{II}},$ $\alpha_{23}^{\mathrm{I}}=\pi-\alpha_{41}^{\mathrm{I}}=\alpha_{23}^{\mathrm{II}}=\pi-\alpha_{41}^{\mathrm{II}},$ $\alpha_{12}^{\mathrm{III}}=\alpha_{23}^{\mathrm{IV}},\alpha_{23}^{\mathrm{III}}+\alpha_{12}^{\mathrm{IV}}=\pi,$ $\alpha_{34}^{\mathrm{III}}+\alpha_{41}^{\mathrm{IV}}=\pi,\alpha_{41}^{\mathrm{III}}+\alpha_{34}^{\mathrm{IV}}=2\pi.$	Trapezoid

Table B.3 The properties of the mobile assemblies of spherical 4*R* linkage

Mobile assemblies	Novel	Networks	Rigid origami pattern
Identical linkage	_	Yes	Yes
ID2	Yes	Yes	Yes
ID3	Yes	Yes	Yes
ID4	Yes	Yes	Yes
ID5	Yes	Yes	Yes
ID6	Yes	Yes	Yes
ID7	Yes	Yes	Yes
ID8	Yes	_	_

Orthogonal	_	Yes	Yes
Miura-Ori's variation	_	Yes	Yes
Planar symmetric	_	Yes	Yes
Rotational symmetric	Yes	_	_
Translational	_	Yes	_
Reverse supplementary	Yes	_	_
Supplementary	Yes	Yes	Yes
Reverse translational	Yes	_	_
Reverse symmetric	Yes	Yes	_
Psym-RotSym	Yes	_	_
Psym-ID3	Yes	Yes	Yes
Psym-ID4	Yes	Yes	Yes
RotSym-ID3	Yes	_	_
RotSym-ID4	Yes	_	_
Tran-RevTran	Yes	_	_
ID8-Tran	Yes	_	_
ID8-RevTran	Yes	_	_
Sup-RevSup	Yes	_	_

ID7-Sup	Yes	Yes	Yes
ID7-RevSup	Yes	_	_

Appendix C

C.1 The geometric condition

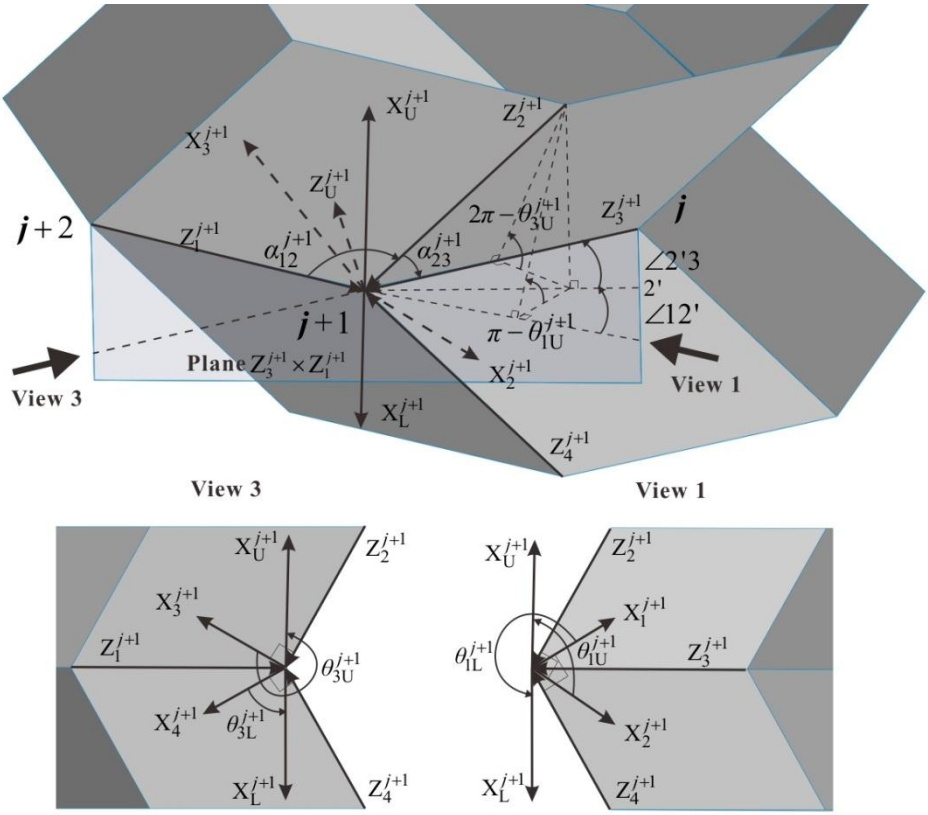

Fig. C.1 The transformations between coordinate frames in linkage $j+1$.

In Fig. C.1, the axes are defined as $X_U^{j+1}=Z_3^{j+1}\times Z_1^{j+1}$, $Z_U^{j+1}=Z_2^{j+1}\times X_U^{j+1}$, $X_L^{j+1}=Z_1^{j+1}\times Z_3^{j+1}$ and $Z_L^{j+1}=X_L^{j+1}\times Z_4^{j+1}$. The rotation angle θ_{3U}^{j+1} rotates from X_3^{j+1} to X_U^{j+1} positively about Z_3^{j+1}, θ_{3L}^{j+1} rotates from X_4^{j+1} to X_L^{j+1}, positively about Z_3^{j+1}, θ_{1U}^{j+1} rotates from X_2^{j+1} to X_U^{j+1}, positively about Z_1^{j+1}, θ_{1L}^{j+1} from X_1^{j+1} to X_L^{j+1}, positively about Z_1^{j+1}. Line 2' is the projection of axis Z_2^{j+1} on the intersection. In order to keep the movements of the halves compatible and the intersection polygon planer during the movement, adjacent planes $Z_3^{j+1}\times Z_1^{j+1}$ and $Z_3^{j}\times Z_1^{j}$ should be coplanar, and the rotation angles

$$\theta_{3U}^{j+1} + \theta_{1U}^{j} = 2\pi, \theta_{3L}^{j+1} + \theta_{1L}^{j} = 2\pi. \tag{C.1}$$

The transformations from coordinate frames X_3^{j+1} - Z_2^{j+1} and X_2^{j+1} - Z_2^{j+1} to X_U^{j+1} - Z_U^{j+1} respectively are,

$$\mathbf{F}_{U}^{j+1} = \mathbf{R}_{x}\left(\alpha_{23}^{j+1}\right)\mathbf{R}_{z}\left(\theta_{3U}^{j+1}\right)\mathbf{R}_{x}\left(\frac{3\pi}{2} - \angle 2'3\right)\mathbf{F}_{32}^{j+1}, \tag{C.2a}$$

$$\mathbf{F}_{U}^{j+1} = \mathbf{R}_{x}\left(-\alpha_{12}^{j+1}\right)\mathbf{R}_{z}\left(\theta_{1U}^{j+1}\right)\mathbf{R}_{x}\left(\frac{\pi}{2} + \angle 12'\right)\mathbf{F}_{22}^{j+1}. \tag{C.2b}$$

The homogeneous transformations from frames X_3^{j+1} - Z_2^{j+1} to X_3^{j-1} - Z_2^{j-1} and X_2^{j+1} - Z_2^{j+1} to X_2^{j-1} - Z_2^{j-1} respectively are

$$\mathbf{F}_{32}^{j-1} = \mathbf{T}_{32}^{(j+1)j}\mathbf{T}_{32}^{j(j-1)}\mathbf{F}_{32}^{j+1}, \tag{C.3a}$$

$$\mathbf{F}_{22}^{j-1} = \mathbf{T}_{22}^{(j+1)j}\mathbf{T}_{22}^{j(j-1)}\mathbf{F}_{22}^{j+1}, \tag{C.3b}$$

in which

$$\mathbf{T}_{32}^{(j+1)j} = \mathbf{R}_{x}\left(\alpha_{23}^{j+1}\right)\mathbf{R}_{x}\left(\pi\right)\mathbf{T}_{z}\left(L_{j+1}^{j}\right)\mathbf{R}_{x}\left(\alpha_{12}^{j}\right)\mathbf{R}_{z}\left(\theta_{2}^{j}\right),$$

$$\mathbf{T}_{22}^{(j+1)j} = \mathbf{R}_{z}\left(\theta_{2}^{j+1}\right)\mathbf{R}_{x}\left(\alpha_{23}^{j+1}\right)\mathbf{R}_{x}\left(\pi\right)\mathbf{T}_{z}\left(L_{j+1}^{j}\right)\mathbf{R}_{x}\left(\alpha_{12}^{j}\right).$$

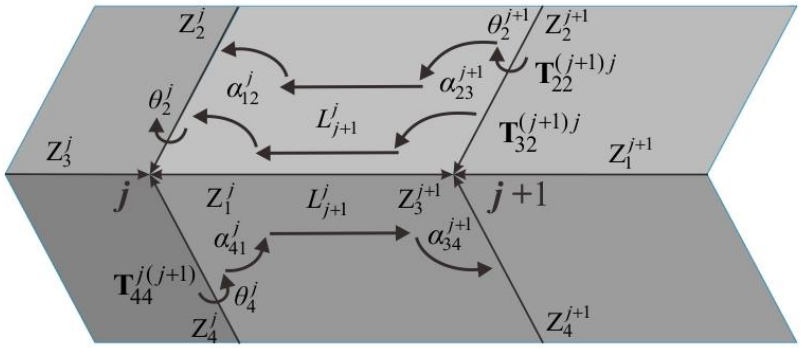

Fig. C.2 The transformations of coordinate frames between linkages j and $j+1$in upper and lower halves.

As shown in Fig.C.2, the matrix $\mathbf{T}_{32}^{(j+1)j}$ represents the transformation from the coordinate frame X_3^{j+1} - Z_2^{j+1} to X_3^{j} - Z_2^{j}. The matrix $\mathbf{T}_{22}^{(j+1)j}$ represents the transformation from the coordinate frame X_2^{j+1} - Z_2^{j+1} to X_2^{j} - Z_2^{j}. So the coordinates of vertex $j-1$ in frame X_3^{j+1} - Z_2^{j+1} and X_2^{j+1} - Z_2^{j+1} can be obtained from (C.3a) and (C.3b) as

$$\begin{aligned} x_{32} &= -\sin\theta_2^j \sin\alpha_{12}^{j-1} L_j^{j-1}, \\ y_{32} &= \cos\theta_2^j \sin\alpha_{12}^{j-1} L_j^{j-1} + \sin\alpha_{12}^{j} L_{j+1}^{j}, \\ z_{32} &= \cos\alpha_{12}^{j-1} L_j^{j-1} + \cos\alpha_{12}^{j} L_{j+1}^{j}, \end{aligned} \tag{C.4a}$$

$$\begin{aligned} x_{22} &= -\sin(\theta_2^{j+1} + \theta_2^j)\sin\alpha_{23}^{j} L_j^{j-1} - \sin\theta_2^{j+1} \sin\alpha_{23}^{j+1} L_{j+1}^{j}, \\ y_{22} &= \cos(\theta_2^{j+1} + \theta_2^j)\sin\alpha_{23}^{j} L_j^{j-1} + \cos\theta_2^{j+1} \sin\alpha_{23}^{j+1} L_{j+1}^{j}, \\ z_{22} &= -\cos\alpha_{23}^{j} L_j^{j-1} - \cos\alpha_{23}^{j+1} L_{j+1}^{j}. \end{aligned} \tag{C.4b}$$

After the coordinates (C.4a) and (C.4b) are transformed to the frame of $\mathrm{X}_{\mathrm{U}}^{j+1}$ - $\mathrm{Z}_{\mathrm{U}}^{j+1}$ using the transformation in (C.2a) and (C.2b), vertex $j-1$ should always be on the plane of intersection $\mathrm{Z}_3^{j+1} \times \mathrm{Z}_1^{j+1}$, i.e. the distances along axis $\mathrm{X}_{\mathrm{U}}^{j+1}$ are 0. Substituting (4.4) and (C.4a) into (C.2a) derives

$$\cot\theta_{3\mathrm{U}}^{j+1} = \frac{\cos\alpha_{12}^{j-1}\sin\alpha_{12}^{j} - \sin\alpha_{12}^{j-1}\cos\alpha_{12}^{j}\cos\theta_2^j}{\sin\alpha_{12}^{j-1}\sin\theta_2^j} = -\cot\theta_{1\mathrm{U}}^{j}. \tag{C.5a}$$

Substituting (4.4), (C.4b) and (C.5a) into (C.2b) derives

$$\cot\theta_{1\mathrm{U}}^{j} = \frac{\cos\alpha_{12}^{j+1}\sin\alpha_{12}^{j} - \sin\alpha_{12}^{j+1}\cos\alpha_{12}^{j}\cos\theta_2^{j+1}}{\sin\alpha_{12}^{j+1}\sin\theta_2^{j+1}} = -\cot\theta_{3\mathrm{U}}^{j+1}. \tag{C.5b}$$

According to the dashed triangles in Fig. C.1,

$$-\sin\alpha_{23}^{j+1}\sin\theta_{3\mathrm{U}}^{j+1}=\sin\alpha_{12}^{j+1}\sin\theta_{1\mathrm{U}}^{j+1}. \tag{C.6}$$

Substituting (4.4), (C.5a) and (C.5b) into (C.6) derives

$$\cos\theta_{3\mathrm{U}}^{j+1}=\frac{\sin\alpha_{12}^{j}\cos\alpha_{12}^{j+1}-\sin\alpha_{12}^{j+1}\cos\alpha_{12}^{j}\cos\theta_{2}^{j+1}}{-\sin\alpha_{12}^{j+1}\cos\alpha_{12}^{j}+\sin\alpha_{12}^{j}\cos\alpha_{12}^{j+1}\cos\theta_{2}^{j+1}}\cos\theta_{1\mathrm{U}}^{j+1}. \tag{C.7}$$

The relationships between $\cos\theta_{3\mathrm{L}}^{j}$ and $\cos\theta_{1\mathrm{L}}^{j}$ can also be obtained in the lower half using such method. Thus,

$$\cos\theta_{1\mathrm{U}}^{j-1}=\cos\theta_{3\mathrm{U}}^{j}=\frac{C_{\mathrm{U}}^{j}-D_{\mathrm{U}}^{j}\cos\theta_{2}^{j}}{-D_{\mathrm{U}}^{j}+C_{\mathrm{U}}^{j}\cos\theta_{2}^{j}}\cos\theta_{1\mathrm{U}}^{j}, \tag{C.8a}$$

$$\cos\theta_{1\mathrm{L}}^{j-1}=\cos\theta_{3\mathrm{L}}^{j}=\frac{C_{\mathrm{L}}^{j}-D_{\mathrm{L}}^{j}\cos\theta_{4}^{j}}{-D_{\mathrm{L}}^{j}+C_{\mathrm{L}}^{j}\cos\theta_{4}^{j}}\cos\theta_{1\mathrm{L}}^{j}, \tag{C.8b}$$

And

$$C_{\mathrm{U}}^{j}=\sin\alpha_{12}^{j-1}\cos\alpha_{12}^{j},\ D_{\mathrm{U}}^{j}=\sin\alpha_{12}^{j}\cos\alpha_{12}^{j-1},$$

$$C_{\mathrm{L}}^{j}=\sin\alpha_{41}^{j-1}\cos\alpha_{41}^{j},\ D_{\mathrm{L}}^{j}=\sin\alpha_{41}^{j}\cos\alpha_{41}^{j-1}.$$

Equation (C.8a) will be represented as $\cos\theta_{3\mathrm{U}}^{j}=f_{\mathrm{U}}^{j}(\cos\theta_{1\mathrm{U}}^{j})$ for short in the following analysis. From linkage I to *j*, in the upper half,

$$\begin{aligned}
&\cos\theta_{1\mathrm{U}}^{\mathrm{I}-1}=\cos\theta_{3\mathrm{U}}^{\mathrm{I}}=f_{\mathrm{U}}^{\mathrm{I}}(\cos\theta_{1\mathrm{U}}^{\mathrm{I}}),\\
&\cos\theta_{1\mathrm{U}}^{\mathrm{I}}=\cos\theta_{3\mathrm{U}}^{\mathrm{II}}=f_{\mathrm{U}}^{\mathrm{II}}(\cos\theta_{1\mathrm{U}}^{\mathrm{II}}),\\
&\vdots\\
&\cos\theta_{1\mathrm{U}}^{j-2}=\cos\theta_{3\mathrm{U}}^{j-1}=f_{\mathrm{U}}^{j-1}(\cos\theta_{1\mathrm{U}}^{j-1}),\\
&\cos\theta_{1\mathrm{U}}^{j-1}=\cos\theta_{3\mathrm{U}}^{j}=f_{\mathrm{U}}^{j}(\cos\theta_{1\mathrm{U}}^{j}),\\
&\Rightarrow
\end{aligned}$$

$$\cos\theta_{1\mathrm{U}}^{\mathrm{I}-1}=f_{\mathrm{U}}^{\mathrm{I}}(f_{\mathrm{U}}^{\mathrm{II}}(\cdots f_{\mathrm{U}}^{j-1}(f_{\mathrm{U}}^{j}(\cos\theta_{1\mathrm{U}}^{j}))\cdots)). \tag{C.9}$$

Therefore, for a closed assembly of *N* linkages, $\cos\theta_{1\mathrm{U}}^{N}=\cos\theta_{3\mathrm{U}}^{\mathrm{I}}$, the following is obtained,

$$1=\prod_{j=\mathrm{I}}^{N}\frac{C_{\mathrm{U}}^{j}-D_{\mathrm{U}}^{j}\cos\theta_{2}^{j}}{-D_{\mathrm{U}}^{j}+C_{\mathrm{U}}^{j}\cos\theta_{2}^{j}}. \tag{C.10a}$$

Also, in the lower half,

$$1=\prod_{j=\mathrm{I}}^{N}\frac{C_{\mathrm{L}}^{j}-D_{\mathrm{L}}^{j}\cos\theta_{4}^{j}}{-D_{\mathrm{L}}^{j}+C_{\mathrm{L}}^{j}\cos\theta_{4}^{j}}. \tag{C.10b}$$

C.2 The geometric property of the prism with plane symmetric intersection

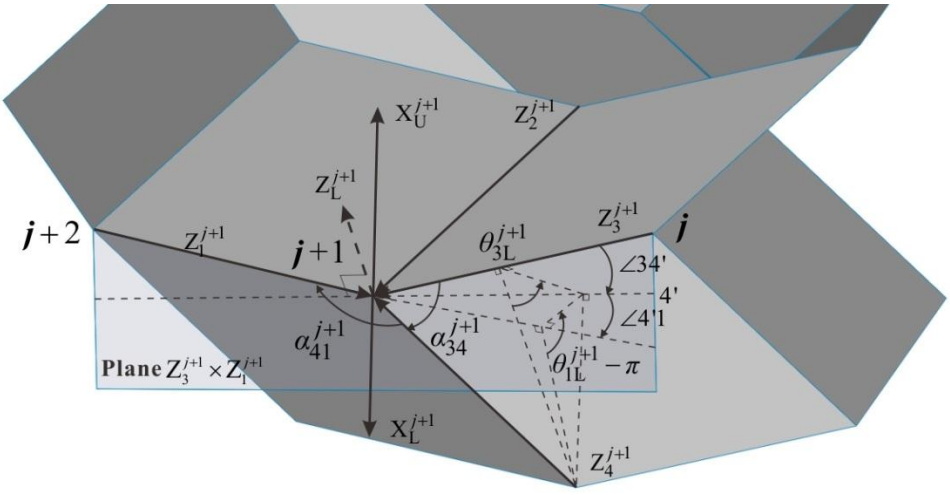

Fig. C.3 The relationships of angles in linkage $n+1$.

In linkage $n+1$ of the prism with line symmetric intersection, the following relationships of angles can be obtained from the dashed triangles, see Fig. C.1 and C.3,

$$\begin{aligned}&\tan\angle 2'3=\tan\alpha_{23}^{j+1}\cos\theta_{3\mathrm{U}}^{j+1},\quad \tan\angle 12'=\tan\alpha_{12}^{j+1}\cos\theta_{1\mathrm{U}}^{j+1},\\&\tan\angle 4'3=\tan\alpha_{34}^{j+1}\cos\theta_{3\mathrm{L}}^{j+1},\quad \tan\angle 14'=\tan\alpha_{41}^{j+1}\cos\theta_{1\mathrm{L}}^{j+1}.\end{aligned} \tag{C.11}$$

Eqns. (C.5a), (C.5b) and the relationships of twist angles in (4.26) are substituted into (C.11), which derives

$$\angle 2'3=\angle 12',\quad \angle 4'3=\angle 14'. \tag{C.12}$$

Thus, axes X_U^{n+1} and X_L^{n+1} are in the same direction and collinear with the bisector of angle $\angle n(n+1)(n+2)$. Axes Z_2^{n+1} and Z_4^{n+1} are in the plane that perpendicular to the plane of intersection and the axis of symmetry line $I(n+1)$. Due to the ridgelines in each half are parallel, Z_2^js and Z_4^js are in the parallel planes of Z_2^{n+1} and Z_4^{n+1}.

References

Allen, D. M. (1986), *The Principles and Practice of Photochemical Machining and Photoetching*, Adam Hilger.

Antkowiak, A., Audoly, B., Josserand, C., Neukirch, S. and Rivetti, M. (2011), Instant fabrication and selection of folded structures using drop impact, *Proceedings of the National Academy of Sciences*, 108(26): 10400-10404.

Ario, I., Nakazawa, M., Tanaka, Y., Tanikura, I. and Ono, S. (2013), Development of a prototype deployable bridge based on origami skill, *Automation in Construction*, 32: 104-111.

Baranger, E., Cluzel, C. and Guidault, P. A. (2011), Modelling of the Behaviour of Aramid Folded Cores Up to Global Crushing, *Strain*, 47: 170-178.

Basily, B. B. and Elsayed, E. A. (2004), Dynamic axial crushing of multilayer core structures of folded Chevron patterns, *Int. J. of Materials and Product Technology*, 21(1/2/3): 169 - 185.

Basily, B. B. and Elsayed, E. A. (2005), Design and development of lightweight sandwich structures with innovative sheet folded cores, *Working papers, Department of Industrial and Systems Engineering, Rutgers University*.

Belcastro, s.-m. and Hull, T. C. (2002), Modelling the folding of paper into three dimensions using affine transformations, *Linear Algebra and its Applications*, 348(1–3): 273-282.

Benbernou, N., Demaine, E. D., Demaine, M. L. and Ovadya, A. (2009), A Universal Crease Pattern for Folding Orthogonal Shapes, *CoRR*, abs/0909.5388.

Bennett, G. T. (1903), A new mechanism, *Engineering*, 76: 777-778.

Bern, M. and Hayes, B. (1996), The complexity of flat origami, *Proceedings of the seventh annual ACM-SIAM symposium on Discrete algorithms*,

Atlanta, Georgia, United States, Society for Industrial and Applied Mathematics.

Bobenko, A. and Pinkall, U. (1996), Discrete surfaces with constant negative Gaussian curvature and the Hirota equation, *Journal of Differential Geometry*, 43: 527-611.

Bobenko, A. I. and Suris, Y. B. (2008), *Discrete differential geometry : integrable structure*, Providence, R.I., American Mathematical Society.

Bodle, J. G. and Lungerhausen, C. C. (1987), US Patent 4653951, US Patent 4653951.

Botke, M., Murphy, D., Murphey, T. and Sorensen, P. (2002), Zero Deadband, Multiple Strut Synchronized Hinge for Deployable Structures, *36th Aerospace Mechanisms Symposium*, Cleveland, USA.

Buri, H. and Weinand, Y. (2008), Origami-Folded Plate Structures, Architecture, *10th World Conference on Timber Engineering*, Miyazaki, Japan.

Byoungkwon, A. and Rus, D. (2012), Programming and controlling self-folding robots, *2012 IEEE International Conference on Robotics and Automation (ICRA)*.

Cecchi, A. and Sab, K. (2007), A homogenized Reissner–Mindlin model for orthotropic periodic plates: Application to brickwork panels, *International Journal of Solids and Structures*, 44(18–19): 6055-6079.

Cervantes-Sánchez, J. J. and Medellín-Castillo, H. I. (2002), A robust classification scheme for spherical 4R linkages, *Mechanism and Machine Theory*, 37(10): 1145-1163.

Chalapat, K., Chekurov, N., Jiang, H., Li, J., Parviz, B. and Paraoanu, G. S. (2013), Self-Organized Origami Structures via Ion-Induced Plastic Strain, *Advanced Materials*, 25(1): 91-95.

Chen, Y. (2003), *Design of structural mechanisms*, PhD Thesis, University of Oxford.

Chiang, C. H. (1984), On the classification of spherical four-bar linkages, *Mechanism and Machine Theory*, 19(3): 283-287.

Chiang, C. H. (1988), *Kinematics of spherical mechanisms*, Cambridge, New York, New Rochelle, Melbourne, Sydney.

Chudoba, R., van der Woerd, J., Schmerl, M. and Hegger, J. (2013), ORICRETE: Modeling support for design and manufacturing of folded concrete structures, *Advances in Engineering Software*.

Dai, J. S. and Cannella, F. (2007), Stiffness Characteristics of Carton Folds for Packaging, *Journal of Mechanical Design*, 130(2): 022305-022305.

Dai, J. S. and Jones, J. R. (1999), Mobility in Metamorphic Mechanisms of Foldable/Erectable Kinds, *Journal of Mechanical Design*, 121(3): 375-382.

Dai, J. S. and Jones, J. R. (2002), Kinematics and mobility analysis of carton folds in packing manipulation based on the mechanism equivalent, *Proceedings of the Institution of Mechanical Engineers, Part C: Journal of Mechanical Engineering Science*, 216(10): 959-970.

Demaine, E. D. and Demaine, M. L. (2001), Recent results in computational origami, *Proceedings of the 3rd International Meeting of Origami Science, Math, and Education*, A.K.Peters, Monterey, CA.

Denavit, J. and Hartenberg, R. S. (1955), A kinematic notation for lower-pair mechanisms based on matrices, *Trans ASME J. Appl. Mech*, 23: 215-221.

Dupont (2014), Elvaloy AC resins Product Data Sheet, http://www2.dupont.com/Elvaloy/en_US/assets/downloads/elvaloy_ac_1820.pdf.

Elsayed, E. A. and Basily, B. B. (2004), A continuous folding process for sheet materials, *Int. J. of Materials and Product Technology*, 21(1/2/3): 217-238.

Felton, S., Tolley, M., Demaine, E., Rus, D. and Wood, R. (2014), A method for building self-folding machines, *Science*, 345(6197): 644-646.

Fischer, S., Drechsler, K., Kilchert, S. and Johnson, A. (2009a), Mechanical tests for foldcore base material properties, *Composites Part A: Applied Science and Manufacturing*, 40(12): 1941-1952.

Fischer, S., Heimbs, S., Kilchert, S., Klaus, M. and Cluzel, C. (2009b), Sandwich structures with folded core: manufacturing and mechanical behavior, *SAMPE Europe international conference*, Paris.

Focatiis, D. S. A. D. and Guest, S. D. (2002), Deployable membranes designed from folding tree leaves, *Phil. Trans. R. Soc. Lond. A*, 360: 227-238.

Gattas, J. M., Wu, W. and You, Z. (2013a), Miura-Base Rigid Origami: Parameterizations of First-Level Derivative and Piecewise Geometries, *Journal of Mechanical Design*, 135(11): 111011-111011.

Gattas, J. M. and You, Z. (2013b), Quasi-Static Impact Response of Alternative Origami-Core Sandwich Panels, *ASME 2013 International Design Engineering Technical Conferences and Computers and Information in Engineering Conference*, Portland, Oregon, USA,.

Gattas, J. M. and You, Z. (2014a), Miura-base rigid origami: parametrisations of curved-crease geometries, *Journal of Mechanical Design*.

Gattas, J. M. and You, Z. (2014b), Quasi-static impact of indented foldcores, *International Journal of Impact Engineering*, 73: 15-29.

Gattas, J. M. and You, Z. (2014c), The Behaviour of Curved-Crease Foldcores under Quasi-Static Impact Loads, *International Journal of Solids and Structures*.

Gruber, P., Häuplik, S., Imhof, B., Özdemir, K., Waclavicek, R. and Perino, M. A. (2007), Deployable structures for a human lunar base, *Acta Astronautica*, 61(1–6): 484-495.

Guest, S. D. and Pellegrino, S. (1994), The folding of Triangulated Cylinders,Part I: Geometric Considerations, *ASME Journal of Applied Mechanics*, 61: 773-777.

Guo, X., Li, H., Yeop Ahn, B., Duoss, E. B., Hsia, K. J., Lewis, J. A. and Nuzzo, R. G. (2009), Two- and three-dimensional folding of thin film single-crystalline silicon for photovoltaic power applications, *Proceedings of the National Academy of Sciences*, 106(48): 20149-20154.

Hawkes, E., An, B., Benbernou, N. M., Tanaka, H., Kim, S., Demaine, E. D., Rus, D. and Wood, R. J. (2010), Programmable matter by folding, *Proceedings of the National Academy of Sciences*.

Heimbs, S. (2009), Virtual testing of sandwich core structures using dynamic finite element simulations, *Computational Materials Science*, 45(2): 205-216.

Heimbs, S. (2013), Foldcore Sandwich Structures and Their Impact Behaviour: An Overview, *Dynamic Failure of Composite and Sandwich Structures*, S. Abrate, B. Castanié and Y. D. S. Rajapakse, Springer Netherlands. 192**:** 491-544.

Heimbs, S., Cichosz, J., Kilchert, S. and Klaus, M. (2009), Sandwich panels with cellular cores made of folded composite material: mechanical behaviour and impact performance, *17th international conference on composite materials (ICCM-17)*, Edinburgh.

Heimbs, S., Cichosz, J., Klaus, M., Kilchert, S. and Johnson, A. F. (2010), Sandwich structures with textile-reinforced composite foldcores under impact loads, *Composite Structures*, 92(6): 1485-1497.

Heimbs, S., Mehrens, T., Middendorf, P., Maier, M. and Schumacher, A. (2007), Numerical determination of the nonlinear effective mechanical properties of folded core structures for aircraft sandwich panels, *6th European LS-Dyna users conference*, Gothenburg.

Heimbs, S., Middendorf, P., Kilchert, S., Johnson, A. F. and Maier, M. (2007), Experimental and Numerical Analysis of Composite Folded Sandwich Core Structures Under Compression, *Applied Composite Materials*, 14(5-6): 363-377.

Hoberman, C. (1993), Curved pleated sheet structures. United States, Patent No. 5,234,727.

Howell, L. L. (2001), *Compliant mechanisms*, John Wiley & Sons.

Huffman, D. A. (1976), Curvature and Creases: A Primer on Paper, *Computers, IEEE Transactions on*, C-25(10): 1010-1019.

Ionov, L. (2013), Bioinspired Microorigami by Self-Folding Polymer Films, *Macromolecular Chemistry and Physics*, 214(11): 1178-1183.

Ishida, S., Nojima, T. and Hagiwara, I. (2014), Mathematical Approach to Model Foldable Conical Structures Using Conformal Mapping, *Journal of Mechanical Design*, 136(9): 091007-091007.

Izmestiev, I. (2009), Projective background of the infinitesimal rigidity of frameworks, *Geometriae Dedicata*, 140(1): 183-203.

Kanemitsu, T. (1998), Self-deployable antenna using centrifugal force, *IUTAM-IASS Symposium On Deployable Structures: Theory and Applications*, Cambridge, UK.

Karpenkov, O. (2010), On the flexibility of Kokotsakis meshes, *Geometriae Dedicata*, 147(1): 15-28.

Kazemahvazi, S., Kiele, J., Russel, B., Deshpande, V. and Zenkert, D. (2010), IMPACT PROPERTIES OF CORRUGATED COMPOSITE SANDWICH CORES *9th International Conference on Sandwich Structures*.

Kelsey, S., Gellatly, R. A. and Clark, B. W. (1958), The Shear Modulus of Foil Honeycomb Cores, *Aircraft Engineering and Aerospace Technology*, 30(10): 294-302.

Kiper, G. and Soylemez, E. (2009), Deployable space structures, *Recent Advances in Space Technologies, 2009. RAST '09. 4th International Conference on*.

Klaus, M. and Reimerdes, H. G. (2009), Residual strength simulations of sandwich panels after impact, *17th international conference on composite materials (ICCM-17)*, Edinburgh.

Klett, Y., Drechsler, K. (2010), Designing technical tessellations, *In Proceedings of The 5th International Conference on Origami in Science, Mathematics, and Education (5OSME)*, Singapore.

Kokotsakis, A. (1933), Über bewegliche Polyeder, *Mathematische Annalen*, 107(1): 627-647.

Kuribayashi, K., Tsuchiya, K., You, Z., Tomus, D., Umemoto, M., Ito, T. and Sasaki, M. (2006), Self-deployable origami stent grafts as a biomedical application of Ni-rich TiNi shape memory alloy foil, *Materials Science and Engineering: A*, 419(1–2): 131-137.

Lebée, A. and Sab, K. (2010a), Reissner–Mindlin Shear Moduli of a Sandwich Panel with Periodic Core Material, *Mechanics of Generalized Continua*, G. A. Maugin and A. V. Metrikine, Springer New York. 21**:** 169-177.

Lebée, A. and Sab, K. (2010b), Transverse shear stiffness of a chevron folded core used in sandwich construction, *International Journal of Solids and Structures*, 47(18–19): 2620-2629.

Lebée, A. and Sab, K. (2011), A Bending-Gradient model for thick plates, Part II: Closed-form solutions for cylindrical bending of laminates, *International Journal of Solids and Structures*, 48(20): 2889-2901.

Lebée, A. and Sab, K. (2012), Homogenization of thick periodic plates: Application of the Bending-Gradient plate theory to a folded core sandwich panel, *International Journal of Solids and Structures*, 49(19–20): 2778-2792.

Leong, Y. W. and Hamada, H. (2010), *Introduction to Film Insert Injection Molding: A Practical & Theoretical Approach*, Lambert Academic Publishing.

Liu, S., Chen, Y. and Lu, G. (2013), The Rigid Origami Patterns for Flat Surface, *Proceedings of the ASME 2013 International Design Engineering Technical Conferences & Computers and Information in Engineering Conference*.

Lu, G. and Yu, T. (2003), *Energy Absorption of Structures and Materials*, Cambridge, UK, Woodhead Publishing.

Ma, J., Le, Y. and You, Z. (2010), Axial Crushing Tests of Steel Thin-Walled Square Tubes with Pyramid Pattern, *51st AIAA/ASME/ASCE/AHS/ASC Structures, Structural Dynamics, and Materials Conference*, American Institute of Aeronautics and Astronautics.

Ma, J. and You, Z. (2013a), Energy Absorption of Thin-Walled Square Tubes With a Prefolded Origami Pattern—Part I: Geometry and Numerical Simulation, *Journal of Applied Mechanics*, 81(1): 011003-011003.

Ma, J. and You, Z. (2013b), Energy absorption of thin-walled beams with a pre-folded origami pattern, *Thin-Walled Structures*, 73: 198-206.

Malone, P. K., Crawford, L. and Williams, G. T. (1993), Developing an inflatable solar array, *7th AIAA/Utah State University Annual Conference on Small Satellites*, Logan, USA.

McCarthy, J. M. and Bodduluri, R. M. (2000), Avoiding singular configurations in finite position synthesis of spherical 4R linkages, *Mechanism and Machine Theory*, 35(3): 451-462.

McCarthy, J. M. and Soh, G. S. (2011), *Geometric Design of Linkages*, Springer New York.

Medellín-Castillo, H. I. and Cervantes-Sánchez, J. J. (2005), An improved mobility analysis for spherical 4R linkages, *Mechanism and Machine Theory*, 40(8): 931-947.

Mills, A. (2007), Robert Hooke's 'universal joint' and its application to sundials and the sundial-clock, *Notes and Records of the Royal Society*, 61(2): 219-236.

Miura, K. (1972), Zeta-Core Sandwich-Its Concept and Realization, *ISAS report*, 37(6): 137-164.

Miura, K. (1989a), A Note on Intrinsic Geometry of Origami, *Research of Pattern Formation*, R. Takaki, Tokyo, KTK Scientific Publishers**:** 91–102.

Miura, K. (1989b), Map Fold a La Miura Style, Its Physical Characteristics and Application to the Space Science, *Research of Pattern Formation*, R. Takaki, Tokyo, KTK Scientific Publishers**:** 77–90.

Miura, K. (2002), PCCP Shells, *New Approaches to Structural Mechanics, Shells and Biological Structures*, H. R. Drew and S. Pellegrino, Springer Netherlands. 104**:** 329-339.

Nguyen, M. Q., Jacombs, S. S., Thomson, R. S., Hachenberg, D. and Scott, M. L. (2005), Simulation of impact on sandwich structures, *Composite Structures*, 67(2): 217-227.

Nojima, T. (2002), Modelling of Folding Patterns in Flat Membranes and Cylinder by Origami., *JSME International Journal Series C*, 45(1): 364-370.

Nojima, T. (2007), Origami modeling of functional structures based on organic patterns, Presentation Manuscript at VIPSI Tokyo http://impact.kuaero.kyoto-u.ac.jp/pdf/Origami.pdf.

Nojima, T. and Saito, K. (2006), Development of Newly Designed Ultra-Light Core Structures, *JSME International Journal Series A Solid Mechanics and Material Engineering*, 49(1): 38-42.

Onal, C. D., Wood, R. J. and Rus, D. (2011), Towards printable robotics: Origami-inspired planar fabrication of three-dimensional mechanisms, *Robotics and Automation (ICRA), 2011 IEEE International Conference on*.

Onal, C. D., Wood, R. J. and Rus, D. (2013), An Origami-Inspired Approach to Worm Robots, *Mechatronics, IEEE/ASME Transactions on*, 18(2): 430-438.

Onoda, J. (1988), Two-dimensional deployable truss structures for space applications, *Journal of Spacecraft Rockets*, 25: 109-116.

Perez, A. and McCarthy, J. M. (2002), Bennett's linkage and the cylindroid, *Mechanism and Machine Theory*, 37(11): 1245-1260.

Rapp, E. G. (1960), Sandwich-type structural element, US Patent 2963128.

Rauschenbach., H. S. (1980), *Solar Cell Array Design Handbook*, California, NASA Jet Propulsion Laboratory, California Inst. Tech. 1**:** Ch. 6, Sec. 2, p. 6.

Reynaerts, D., Peirs, J. and Van Brussel, H. (1995), Design of a SMA-actuated gastrointestinal intervention system, *Micro Machine and Human Science, 1995. MHS '95., Proceedings of the Sixth International Symposium on*.

Ruth, D. A. and McCarthy, J. M. (1999), The design of spherical 4R linkages for four specified orientations, *Mechanism and Machine Theory*, 34(5): 677-692.

Ryhänen, J. (1999), *Biocompatibility evaluation of nickel–titanium shape memory metal alloy*, PhD Thesis, University Hospital of Oulu.

Sauer, R. and Graf, H. (1931), Über Flächenverbiegung in Analogie zur Verknickung offener Facettenflache, *Mathematische Annalen*, 105(1): 499-535.

Schenk, M. (2011c), *Folded shell sructures*, PhD Thesis, University of Cambridge.

Schenk, M., Allwood, J. and Guest, S. D. (2011a), Cold gas-pressure folding of Miura-ori sheets, *Steel Research International, Special Issue Proceedings of the International Conference on Technology of Plasticity (ICTP).*

Schenk, M. and Guest, S. D. (2011b), Origami folding: A structural engineering approach, *Origami 5: Fifth International Meeting of Origami Science, Mathematics, and Education (5OSME).*

Schenk, M. and Guest, S. D. (2013), Geometry of Miura-folded metamaterials, *Proceedings of the National Academy of Sciences*, 110(9): 3276-3281.

Schief, W. K., Bobenko, A. I. and Hoffmann, T. (2008), On the Integrability of Infinitesimal and Finite Deformations of Polyhedral Surfaces, *Discrete Differential Geometry*, A. I. Bobenko, J. M. Sullivan, P. Schröder and G. M. Ziegler, Birkhäuser Basel. 38**:** 67-93.

Shen, J., Lu, G., Zhao, L. and Zhang, Q. (2013), Short sandwich tubes subjected to internal explosive loading, *Engineering Structures*, 55: 56-65.

Silverberg, J. L., Evans, A. A., McLeod, L., Hayward, R. C., Hull, T., Santangelo, C. D. and Cohen, I. (2014), Using origami design principles to fold reprogrammable mechanical metamaterials, *Science*, 345(6197): 647-650.

Sogame, A. and Furuya, H. (2000), Conceptual study on cylindrical deployable space structures, *IUTAM-IASS Symposium on Deployable Structures: Theory and Applications*.

Song, C. Y. (2013), *Kinematic study of overconstrained linkages and design of reconfigurable mechanisms*, PhD Thesis, Nanyang Technological University.

Song, J., Chen, Y. and Lu, G. (2012), Axial crushing of thin-walled structures with origami patterns, *Thin-Walled Structures*, 54: 65-71.

Song, J., Chen, Y. and Lu, G. (2013), Light-weight thin-walled structures with patterned windows under axial crushing, *International Journal of Mechanical Sciences*, 66: 239-248.

Sreetharan, P. S., Whitney, J. P., Strauss, M. D. and Wood, R. J. (2012), Monolithic fabrication of millimeter-scale machines, *Journal of Micromechanics and Microengineering*, 22(5): 055027.

Stachel, H. (2009), Remarks on Miura-ori, a Japanese folding method, *ACTA TECHNICA NAPOCENSIS - Series: APPLIED MATHEMATICS, MECHANICS, and ENGINEERING*, 52: 245-248.

Stachel, H. (2010), A kinematic approach to Kokotsakis meshes, *Computer Aided Geometric Design*, 27(6): 428-437.

Tachi, T. (2009a), Generalization of Rigid Foldable Quadrilateral Mesh Origami, *Proceedings of the International Association for Shell and Spatial Structures Symposium*, Madrid.

Tachi, T. (2009b), One-DOF Cylindrical Deployable Structures with Rigid Quadrilateral Panels, *The International Association for Shell and Spatial Structures Symposium*, Madrid.

Tibert, A. G. and Pellegrino, S. (2003), Deployable tensegrity masts, *44th AIAA/ASME/ASCE/AHS/ASC Structures, Structural Dynamics, and Materials Conference*, Norfolk, USA.

Tolman, S. S., Delimont, I. L., Howell, L. L. and Fullwood, D. T. (2014), Material selection for elastic energy absorption in origami-inspired compliant corrugations, *Smart Materials and Structures*, 23(9): 094010.

Trautz, M. and Künstler, A. (2009), Deployable folded plate structures - folding patterns based on 4-fold-mechanism using stiff plates, *Symposium of the International Association for Shell and Spatial Structures*, Valencia.

Wang, K. F. and Chen, Y. (2010), Rigid Origami to Fold a Flat Paper into a Patterned Cylinder, *The 5th international conference on origami in science*, Singapore.

Wang, Z. J. and Xu, Q. H. (2006), Experimental research on soundproof characteristics for the sandwich plates with folded core, *J Vib Eng*, 19: 65-69.

Watanabe, N. and Kawaguchi, K.-i. (2009), The Method for Judging Rigid Foldability, *Origami 4*, A K Peters/CRC Press**:** 165-174.

Wei, G. and Dai, J. S. (2009), Geometry and kinematic analysis of an origami-evolved mechanism based on artmimetics, *ASME/IFToMM International Conference on Reconfigurable Mechanisms and Robots*.

Wei, G. and Dai, J. S. (2014), Origami-Inspired Integrated Planar-Spherical Overconstrained Mechanisms, *Journal of Mechanical Design*, 136(5): 051003-051003.

Wei, Z. Y., Guo, Z. V., Dudte, L., Liang, H. Y. and Mahadevan, L. (2013), Geometric Mechanics of Periodic Pleated Origami, *Physical review letters*, 110(21): 215501.

Wu, W. and You, Z. (2011), A solution for folding rigid tall shopping bags, *Proceedings of the Royal Society A: Mathematical, Physical and Engineering Science*.

Wu, Z., Hagiwara, I. and Tao, X. (2007), Optimisation of crush characteristics of the cylindrical origami structure, *International Journal of Vehicle Design*, 43(1/2/3/4): 66-81.

Yasuda, H., Yein, T., Tachi, T., Miura, K. and Taya, M. (2013), Folding behaviour of Tachi–Miura polyhedron bellows, *Proceedings of the Royal Society A: Mathematical, Physical and Engineering Science*, 469(2159).

Yu, T. and Zhang, L. C. (1996), *Plastic Bending: Theory and Applications*, World Scientific.

Yves, K. and Klaus, D. (2011), Designing Technical Tessellations, *Origami 5*, A K Peters/CRC Press**:** 305-322.

Zakirov, I. M. and Alekseev, K. A. (2010), Design of a wedge-shaped folded structure, *Journal of Machinery Manufacture and Reliability*, 39(5): 412-417.

Zhao, X., Hu, Y. and Hagiwara, I. (2011), Shape Optimization to Improve Energy Absorption Ability of Cylindrical Thin-Walled Origami Structure, *Journal of Computational Science and Technology*, 5(3): 148-162.

Zhou, X., Wang, H. and You, Z. (2014), Mechanical properties of Miura-based folded cores under quasi-static loads, *Thin-Walled Structures*, 82: 296-310.